Analytical and Numerical Methods Applied to Nonlinear Vessel Dynamics and Code Verification for Chaotic Systems

Wan Wu

Dissertation submitted to the Faculty of the
Virginia Polytechnic Institute and State University
in partial fulfillment of the requirements for the degree of

Doctor of Philosophy
in
Aerospace Engineering

Leigh S. McCue, Chair
Alan J. Brown
Kostas J. Spyrou
Craig A. Woolsey

December 1, 2009
Blacksburg, Virginia

Keywords: Ship stability, Melnikov's method, Capsize, Surf-riding, Broaching-to, non-Hamiltonian, Method of Manufactured Solution, Chaotic control

Analytical and Numerical Methods Applied to Nonlinear Vessel Dynamics and Code Verification for Chaotic Systems

Wan Wu

(ABSTRACT)

In this dissertation, the extended Melnikov's method has been applied to several nonlinear ship dynamics models, which are related to the new generation of stability criteria in the International Maritime Organization (IMO). The advantage of this extended Melnikov's method is it overcomes the limitation of small damping that is intrinsic to the implementation of the standard Melnikov's method.

The extended Melnikv's method is first applied to two published roll motion models. One is a simple roll model with nonlinear damping and cubic restoring moment. The other is a model with a biased restoring moment. Numerical simulations are investigated for both models. The effectiveness and accuracy of the extended Melnikov's method is demonstrated.

Then this method is used to predict more accurately the threshold of global surf-riding for a ship operating in steep following seas. A reference ITTC ship is used here by way of example and the result is compared to that obtained from previously published standard analysis as well as numerical simulations. Because the primary drawback of the extended Melnikov's method is the inability to arrive at a closed form equation, a 'best fit' approximation is given for the extended Melnikov numerically predicted result.

The extended Melnikov's method for slowly varying system is applied to a roll-heave-sway coupled ship model. The Melnikov's functions are calculated based on a fishing boat model. And the results are compared with those from standard Melnikov's method. This work is a preliminary research on the application of Melnikov's method to multi-degree-of-freedom ship dynamics.

In the last part of the dissertation, the method of manufactured solution is applied to systems with chaotic behavior. The purpose is to identify points with potential numerical discrepancies, and to improve computational efficiency. The numerical discrepancies may be due to the selection of error tolerances, precisions, *etc.* Two classical chaotic models and two ship capsize models are examined. The current approach overlaps entrainment in chaotic control theory. Here entrainment means two dynamical systems have the same period, phase and amplitude. The convergent region from control theory is used to give a rough guideline on identifying numerical discrepancies for the classical chaotic models. The effectiveness of this method in improving computational efficiency is demonstrated for the ship capsize models.

This work has been supported by Dr. Patrick Purtell under Office of Naval Research (ONR) Grant N00014-06-1-0551 and by Dr. Eduardo Misawa under National Science Foundation (NSF) Grant CMMI 0747973.

Dedication

To my dearest dad, mom and husband

who love me and support me unconditionally

Acknowledgments

I owe my deepest gratitude to my advisor, Dr. Leigh McCue-Weil. She provided me support, encouragement and guidance during my PhD study. Her vision and insightful thoughts have always thrown me light when I went into dark end. She is more than an excellent advisor, but a mentor and role model. Dr. McCue, I am honored to be your first PhD student!

My special thanks goes to Dr. Kostas Spyrou. He gave me tremendous help during my stay at NTUA. He helped me to set up the problem in Chapter 4 and provided me guidance and suggestions. Without him, the work in Chapter 4 could not be possible. I would also like to show my great appreciation to Dr. Chris Roy. Thanks for his patience to help me understand the MMS and provided insightful suggestions for the work in Chapter 6.

I want to express my appreciation to Dr. Craig Woolsey and Dr. Alan Brown. Thank you for serving as my committee and for your kind help through my graduate study. I want to thank Dr. Shane Ross for the useful discussion about chaotic control. Thank you for your patience and help. My gratitude goes to my colleagues and officemates: Qing Yang, Zhiliang Xing, and William Story. It has always been a pleasure to work with you.

Besides the people who work with me, I want to thank my best friend Yanpeng Hou and my lovely roommates: Xiaojun Chang and Shijing Cheng, who cheered me up when I was sad and took care of me when I was sick. You made my life in Blacksburg colorful!

Contents

1 Introduction **1**

1.1 Background and motivation 1

1.2 Literature review 3

1.3 Equations of motion of ship dynamics 8

1.4 Nonlinear vessel dynamics 11

1.5 Background on method of manufactured solution 12

1.6 Summary of coming chapters 13

2 Melnikov's Method **16**

2.1 Melnikov's method for single-DOF dynamical systems 16

2.2 Melnikov's function for system with large damping terms 19

2.3 Melnikov's method for multi-degree-of-freedom system 23

2.4 Melnikov's method for multi-DOF system with large damping 26

2.5 Summary 28

3 Melnikov's Method for the 1DOF Rolling Problem without Damping Constraint 30

3.1 Introduction 30

3.2 Simple roll motion 31

3.2.1 Calculation of Melnikov's integral for simple roll motion 33

3.2.2 Numerical simulation for simple roll motion 35

3.3 Biased roll motion 39

3.3.1 Calculation of the Melnikov's integral for biased roll model 40

3.3.2 Numerical simulation for biased roll model 41

3.4 Conclusions 43

4 Melnikov's Method and the 1DOF Surf-riding Problem 44

4.1 Mathematical model 45

4.2 Formulation of Melnikov's function 48

4.2.1 Treating linear damping as large term 49

4.2.2 Treating linear damping and nonlinear damping as large terms 51

4.3 Numerical results 53

4.3.1 Simulation of transition from periodic surfing to surf-riding 53

4.3.2 Treating the linear damping as large 55

4.3.3 Treating both the linear and nonlinear damping terms as large 56

4.4 Concluding remarks 61

5 Melnikov's Method and a Multi-DOF Ship Model **62**

5.1 Introduction 62

5.2 Mathematical model 63

5.3 Melnikov's function 67

5.4 Numerical results 70

5.4.1 Case 1: the equilibrium position $\bar{x}_1 = \pm 0.5647$ 71

5.4.2 Case 2: the equilibrium position $\bar{x}_1 = 0$ 71

5.5 Some remarks 74

6 The Method of Manufactured Solutions Applied to Chaotic Systems **75**

6.1 Introduction 75

6.2 Classic chaotic models 76

6.3 Ship capsizing models 87

6.4 Conclusion 94

7 Practical Impact of This Research **96**

8 Conclusions and Future Work **98**

8.1 Summary 98

8.2 Future work 99

Bibliography **101**

Appendix **109**

List of Figures

1.1 Typical GZ diagram. 4

1.2 GZ diagram with negative GM. 5

2.1 Phase planes of the unperturbed sub-system for different σ. 21

3.1 Critical forcing for different Ω at different δ_1 as well as the remaining of safe basin. '.': Critical forcing from extended Melnikov method. '-M': Critical forcing from Falzarano's results. 36

3.2 Safe basin for different forcing at $\Omega = 1.0$ with $\delta_1 = 0.37$. 38

3.3 Safe basin for different forcing at $\Omega = 0.65$ with $\delta_1 = 0.37$. 39

3.4 Critical forcing for different ω at $\beta = 0.1$. '-': Critical forcing from Spyrou's results. '–': Critical forcing from extended Melnikov method. '-.': Forcing at which 90% of safe basin left. 42

3.5 Critical forcing for different ω at $\beta = 0.05$. '-': Critical forcing from Spyrou's results. '.': Critical forcing from extended Melnikov method. '-.': Forcing at which 90% of safe basin left. 43

4.1 Time series of surging velocity at different propeller rates. 53

4.2 Phase plane of the surge motion. Dash-dotted line: periodic motion. Dashed line: asymmetric surging. Solid line: surf-riding. 54

4.3 The numerical values of σ_c for different values of p_1 compared with empirical formula. 56

4.4 Numerical values of σ_c for different values of p_1 and p_2 when treating both linear and quadratic damping terms large. 57

4.5 Numerical values of σ_c compared with empirical formula. 58

4.6 Numerical values of σ_c compared with empirical formula. 59

4.7 Critical Froude's number and wave height. Solid lines: results from numerical simulations. Dashed line: results from standard Melnikov's method. Solid-dotted line: results from extended Melnikov's method treating linear and quadratic damping large. 60

5.1 Homoclinic orbit for the unperturbed sub-system. 69

5.2 The Melnikov's function for different values of wave amplitude. 72

5.3 The maximum values of Melnikov's function for different values of wave amplitude. 73

5.4 The maximum values of Melnikov's function for different values of wave amplitude. 73

6.1 Direct comparison between manufactured solution and numerical simulation results using DLSODA. Figure 6.1(a) is given with relative and absolute error tolerances of 1.0e-12 and 1.0e-16 respectively. Figure 6.1(b) is simulated using relative error tolerance 1.0e-6 and absolute error tolerance 1.0e-8. Figure 6.1(c) compares Figures 6.1(a) and 6.1(b) for MMS agreement. 80

6.2 Comparison between manufactured solution and numerical simulation results using DLSODA for different agreement definitions. Figures 6.2(a), 6.2(e) and 6.2(c) are all generated with relative and absolute error tolerances of 1.0e-12 and 1.0e-16 respectively. Figure 6.2(a) is generated using L_∞ criterion. Figure 6.2(b) compares Figures 6.1(a) and 6.2(a) for MMS agreement. Figure 6.2(c) is generated using L_2. Figure 6.2(d) compares Figures 6.1(a) and 6.2(c) for MMS agreement. Figure 6.2(e) is generated using L_1. Figure 6.2(f) compares Figures 6.1(a) and 6.2(e) for MMS agreement. 82

6.3 Convergent region of Lorenz oscillator. Figure 6.3(a) is the boundary of convergent region. Above the surface, Eq. (6.8) is satisfied. Figures 6.3(b) and 6.3(c) are the same as Figures 6.1(a) and 6.1(b) except adding the boundary of convergent regions. Figure 6.3(d) compares Figures 6.3(b) and 6.3(c) for MMS agreement. 84

6.4 Convergent region of Rössler oscillator and comparison between numerical results and manufactured solutions. Figure 6.4(a) is integrated using DLSODA with relative error tolerance 1.0e-15 and absolute error tolerance 1.0e-18. Figure 6.4(b) is simulated using DLSODA with relative and absolute error tolerances 1.0e-6 and 1.0e-8, respectively. In both figures, green dots denote agree with manufactured solutions, and red circles denote disagree with manufactured solutions. 86

6.5 Safe basin and direct comparison with manufactured solution using (S/D)LSODA. Figures 6.5(a) and 6.5(b) are simulated using SLSODA and DLSODA, respectively, with relative error tolerance 1.0e-6 and absolute error tolerance 1.0e-8 and checking for capsize every $dt = 0.1$s. Figure 6.5(c) is integrated using DLSODA with relative error tolerance 1.0e-12 and absolute error tolerance 1.0e-16, and checking for capsize every $dt = 0.01$s. Figure 6.5(d) compares Figures 6.5(a) and 6.5(c) for capsize/non-capsize agreement. 91

6.6 Safe basins and direct comparison of manufactured analytic solution to numerical simulation using (S/D)LSODA for the biased model. Figures 6.6(a) and 6.6(b) are simulated using SLSODA and DLSODA respectively, with relative tolerance=1.0e-6 and absolute tolerance=1.0e-8, and checking for capsize every $dt = 0.1$s. Figure 6.6(c) is integrated using DLSODA with relative tolerance=1.0e-12 and absolute tolerance=1.0e-16, and checking for capsize every $dt = 0.01$s. Figure 6.6(d) compares Figures 6.6(a) and 6.6(c) for capsize/non-capsize agreement. 93

6.7 Safe basins and direct comparison of manufactured analytic solution to numerical simulation using (S/D)LSODA for Falzarano and biased models. Figures 6.7(a) and 6.7(c) are integrated using SLSODA with relative tolerance=1.0e-6 and absolute tolerance=1.0e-8, and checking for capsize every $dt = 0.1$s. Figures 6.7(b) and 6.7(d) are integrated using DLSODA with relative tolerance=1.0e-12 and absolute tolerance=1.0e-16, and checking for capsize every $dt = 0.01$s. 95

List of Tables

3.1 Data for non-dimensional parameters for $Patti - B$ from Jiang et al. [2000] . 32

3.2 Critical values of σ for different δ_1 33

3.3 Critical values of σ for different β 41

5.1 Some coefficients for $Patti - B$ from Chen et al. [1999] 70

Chapter 1

Introduction

1.1 Background and motivation

Ship stability is a key aspect for ship design as well as operation. Modern ship stability theory is primarily based on static stability theory. This theory was first investigated by Bouguer and Euler separately in the 18th century. Bouguer found the role of a metacenter in ship stability, and discovered an easy way to calculate metacenter location. Euler studied ship stability based on the restoring moment. Comprehensive historical reviews can be found in works such as Nowachi and Fereiro [2003] and Spyrou [2006].

Froude [1863] pointed out that a ship having its natural frequency of pitch twice that of roll would encounter undesirable roll characteristics. Froude's work is the basis of modern research in nonlinear dynamics on ship motions. A century later, Paulling and Rosenberg [1959] showed that roll and pitch coupling presented parametric instability and can be modeled by the Mathieu equation. A full review of the research in nonlinear ship dynamics can be found in Spyrou and Thompson [2000] and Thompson [1997].

Despite the scientific background in nonlinear ship dynamics, current stability criteria are still mostly based on what we have known by the end of the 19th century. Therefore, it is important to combine nonlinear dynamics into the development of ship stability criteria. 'This appears either in the form of simple formula that offer guidance at very early design stage or as detailed numerical codes that can be used when hull shape and load distribution are known' (Spyrou [2006]).

A next generation of intact stability criteria are now under development by the International Maritime Organization (IMO). Belenky et al. [2008] and Umeda et al. [2009] have reviewed this new stability criteria which will mainly consider capsizing related stability problems in three cases: harmonic resonance for dead ship, maneuvering related problems such as broaching and stability variation problems such as parametric rolling. These problems are all related to nonlinear ship dynamics. And the criteria likely will include performance based criteria and vulnerability criteria.

One purpose of this research is to use nonlinear dynamics tools to propose draft criteria that relate to the development of new stability criteria in IMO. In this thesis, an analytical method called Melnikov's method has been applied. The advantage of this method is that it shows the dynamical property of the whole system by only solving the unperturbed subsystem. Thus this method can greatly reduce computational time compared to numerical simulations. And for some cases, it can provide closed-form formulas. The constraint of this method is a small perturbation assumption, requiring small forcing and damping, which is not always true for nonlinear ship dynamical system. To address this constraint, the extended Melnikov's method is employed. This method can be applied to systems with large perturbation terms at the expense of not being able to produce closed-form formula. Computational efficiency still exists compared to numerical simulations.

The harmonic resonance of a dead ship requires a combination of the effects of wind and

waves on a vessel without power. The simplest model is the single-degree-of-freedom roll motion in beam seas. This model is considered in Chapter 3. Broaching is defined as the uncontrollable turn of a vessel in following or quartering seas (Belenky et al. [2008]). And during the turn, the ship may develop large roll angle, which may lead to capsize. Surf-riding is viewed as the precursor of broaching. A single-degree-of-freedom surf-riding model is considered in Chapter 4. In Chapter 5, Melnikov's method has been used to a roll-heave-sway coupled model in order to find the possibility of applying this method to the coupled parametric roll problem and other multi-degree-of-freedom ship motions problems.

Background on Melnikov's method is presented is Chapter 2 and a literature review on the application of Melnikov's method on nonlinear ship dynamics is given in the next section.

1.2 Literature review

During the last two decades, a great deal of work has been done using Melnikov's method to predict possible capsize, with emphasis on roll motion.

Falzarano [1990], Falzarano et al. [1992] applied Melnikov's method to the single-degree-of-freedom roll motion using a cubic polynomial for the GZ curve with a nonlinear damping term for both heteroclinic and homoclinic cases. The heteroclinic orbit is an approximation of ship rolling between positive and negative angles of vanishing stability. The typical GZ curve for this case is shown in Figure 1.1. The homoclinic case is an approximation of rolling ship with damage or water on deck, which results when the initial GM of the ship is negative. Therefore, the ship will oscillate around a loll angle. The GZ diagram of this case is shown in Figure 1.2. The critical forcing that might lead to capsize was calculated as a function of amplitude for both cases.

Thompson et al. [1987] and Thompson [1997] used a second order polynomial to fit the restoring function for the roll equation, which is known as the Helmholtz-Thompson equation. Closed-form critical wave heights were given with accuracy confirmed by numerical simulation. Later work by Spyrou et al. [2002] focused on the roll model which has an asymmetric restoring function. This model is a good approximation for the dynamics of a ship affected by wind and waves. Spyrou used Melnikov's method based on the calculation over homoclinic orbits and heteroclinic orbits. The relationships between capsizing and closed-form critical wave slope in terms of the amount of bias and damping are found for both cases in close forms.

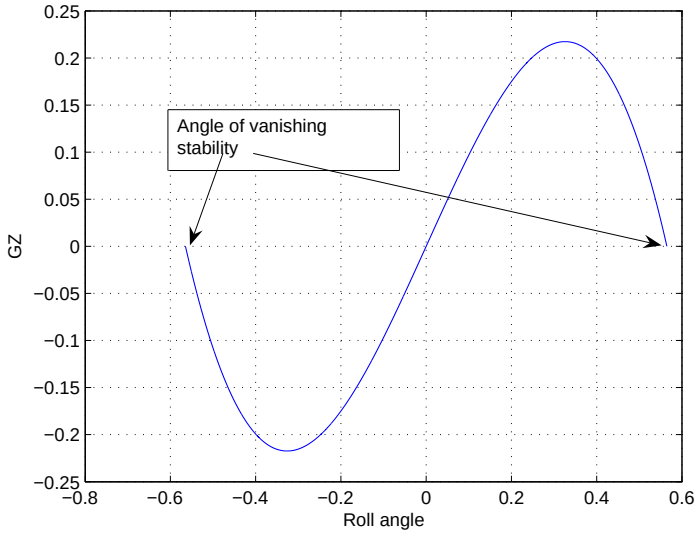

Figure 1.1: Typical GZ diagram.

The work by Bikdash et al. [1994] used Melnikov's method to analyze ship roll motion with general roll damping. Different types of damping models were considered. The influence of different damping terms on Melnikov integral, *i.e.* on ship capsizing, was analyzed in a so called "sensitivity analysis". Kan [1992] analyzed several roll motion models in his work. One is a single degree of freedom parametric roll model, which can be expressed as a Mathieu

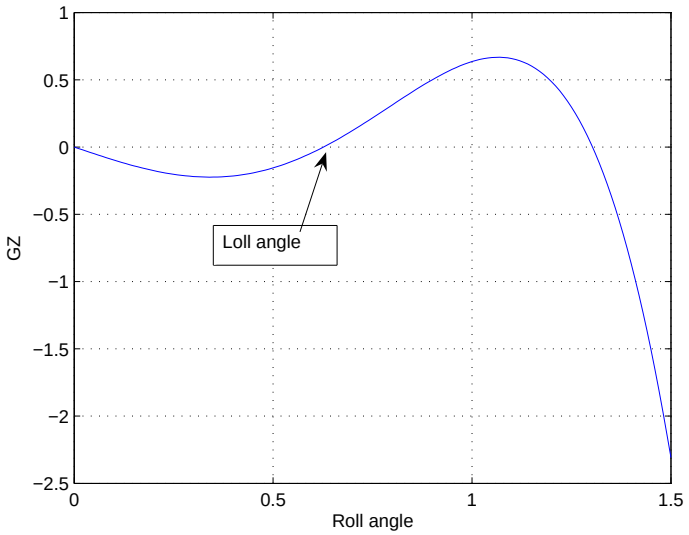

Figure 1.2: GZ diagram with negative GM.

type equation. Another model is for the ship which has negative GM due to water on deck, or flooded water into compartments. This model is called 'loll type capsize equation'. The Melnikov analysis was carried out for both models.

As all previous work are using periodic beam sea as a simplified sea state, a more realistic work by Hsieh et al. [1994] used random beam sea in his single-degree-of-freedom roll model. In this case, the Melnikov's function related to the external force was also a random process $\tilde{M}$. The formulas for mean and mean square of $\tilde{M}$ were obtained for given sea spectrum. Based on these results, the rate of phase space flux was studied which is related to the probability of capsizing. A finite number for rate of phase space flux implies a non-zero probability capsizing. Critical values for significant wave height were determined in the limit of no phase flux rate therefore little chance of capsizing.

An extension of Hsieh's work is by Jiang et al. [1996], who applied a similar method to a biased ship rolling in random beam sea. He carried out similar study for the biased model, and gave the results on how the bias would influence the probability of the onset of ship

capsizing. A more complex application is by Jiang et al. [2000]. In his model, he considered the memory effects for the hydrodynamics force as well as the random sea state for external forcing. The memory effects correspond to frequency and time dependence of the radiation force. This force was approximated from an auxiliary system. The critical significant wave height was derived. Another interesting part in his work was the comparison of different frequencies on the influence of linear and quadratic damping terms. All previous work were setting the coefficients of linear and nonlinear damping terms as constant by assuming a fixed frequency, however, the influence of frequency on these terms even on the onset of capsizing cannot be ignored. After investigation, Jiang et al. [2000] concluded that there was no singular frequency that can be used to formulate capsizing in all cases. Numerical simulation was carried out to compare with the analytical results.

Over the years, surf-riding has been studied numerically, experimentally and analytically. Kan [1990] did experimental and numerical analysis for the 1 DOF surge motion in following waves. His analysis confirmed that surf-riding occurs when the ship surge velocity, after decay of transitional motion, reaches the wave phase speed. Umeda [1990] observed that stable surf-riding is the result when the maximum velocity of surging reaches wave celerity. And he used a two-point boundary formulation to predict the transition to surf-riding. A multi-DOF coupled model was investigated by Spyrou [1995]. The surf-riding in quartering seas was studied using the continuation method. It is revealed that stable surf-riding occurs mostly at wave trough, while at wave crest, instability is dominated. In the middle, the transition occurs which results in complex dynamics.

Grochowalski et al. [1994] performed experiments on surf-riding, broaching and capsize events. According to the experimental data, surf-riding mostly likely occurs at a heading angle between $0^\circ - 20^\circ$. The experimental data showed that when wave length is approximately ship length, surf-riding occurs at $Fn = 0.3$. When the wave length is longer than

twice of ship length, surf-riding was observed at $Fn = 0.23$. Therefore, Grochowalski *et al.* indicated that the speed $V = 1.4\sqrt{L}$ can be used to predict surf-riding. The majority of surf-riding occurs with wave length $\lambda/L = 1.5 - 3.0$, and concentrated in $\lambda/L = 2.0 - 2.5$.

De Kat and Thomas [2000] and De Kat and Thomas [1998] carried out model tests to obtain data for ship extreme motions including surf-riding. And these experimental data were used to validate numerical simulation codes. The experimental data showed that the maximum ship speed can reach a very high value before captured into surf-riding, which may result in bow-diving and possibly broaching. Numerical analysis based on linear wave theory underestimated the wave celerity and the highest speed that the ship can reach before surf-riding.

The work by Spyrou [2000] combined a 2-DOF roll-surge coupled model to a 1-DOF roll model by changing the differentiation variable from time t to relative position x. The influence of surge motion on capsize was studied using this new model. Most recent work is by Spyrou [2006]. In Spyrou's work, a new formula has been developed, which includes propulsion, resistance, and general hull characteristic of the ship. Based on this model, a simple formula was obtained to predict the threshold of global surf-riding using the Melnikov's method. The water particle velocity was also considered by Spyrou, and it showed that for a given wave, the effect of water particle velocity is to shift the threshold of global surf-riding to a higher propeller rate.

The research on multi-DOF ship dynamics is mainly focused on numerical simulations as well as experimental approaches. Comparably little work has been done using the Melnikov's method to analyze multi-DOF ship dynamics.

Falzarano and Zhang [1994] studied a roll-sway coupled system. Since the sway displacement does not explicitly appear in the equation of motion, the coupled system contains three state

variables: roll angle, roll velocity and sway displacement. And the sway motion is slowly varying compared to roll motion. Falzarano used the Melnikov's method to predict the chaotic dynamics in this system. The critical values for manifolds intersection have been obtained numerically based on the Melnikov's function.

Chen and Shaw [1997] used Melnikov's method to study a reduced multi-degree-of-freedom model which was obtained by Chen et al. [1999]. This model is a roll-sway-heave coupled three degree of freedom model. Chen *et al.* used a wave fixed coordinate system and used singular perturbation theory to reduced the system to a roll dominated model with fast varying heave and slowly varying sway. Since heave motion is fast compared to roll and sway, the dynamics of heave will settle in the invariant manifold of slow dynamics. The system is then reduced to a three state variable system. Chen and Shaw [1997] used the Melnikov's method to show the phase space transport and the rate of erosion safe basin. And Chen's results were compared with single-degree-of-freedom model.

1.3 Equations of motion of ship dynamics

The motion of the ship in a seaway is very complex. In the study of vessel dynamics, the vessel is typically treated as 'rigid body'. The full six-degree-of-freedom equations of motions of a ship in seaway have been introduced in several publications (for example, Lewandowski [2004]). These equations are highly nonlinear and coupled. In order to simplify the problem, the equations are linearized under the assumption of small motions, as shown in Eq. (1.1). These equations are listed in the sequence of $1-surge$, $2-sway$, $3-heave$, $4-roll$, $5-pitch$ and $6-yaw$. X, Y, Z, K, M, N are general forces (moments), which contain hydrostatic forces $\mathbf{C}$ and hydrodynamic forces. The hydrostatic forces are proportional to displacement. The hydrodynamical forces that result from incident and diffracted waves are exciting forces $\mathbf{F}$.

The added mass **A** and damping **B** come from radiation forces. **A**, **B**, and **C** are matrices and **F** is a vector. Therefore, we can write the equations of motion in time domain as in Eq. (1.2). **M** is the mass matrix which contains mass and moment of inertial terms. x is a general coordinate representing each of the six-degrees-of-freedom.

$$X = m(\dot{u} + z_G\dot{q}) \tag{1.1a}$$

$$Y = m(\dot{v} + x_G\dot{r} - z_G\dot{p}) \tag{1.1b}$$

$$Z = m(\dot{w} - x_G\dot{q}) \tag{1.1c}$$

$$K = I_{44}\dot{p} - I_{64}\dot{r} - mz_G\dot{v} \tag{1.1d}$$

$$M = I_{55}\dot{q} + m(z_G\dot{u} - x_G\dot{w}) \tag{1.1e}$$

$$N = I_{66}\dot{r} - I_{64}\dot{p} + mx_G\dot{v} \tag{1.1f}$$

It is worth mentioning that in the linearized equations, there are no inertial coupling terms between the longitudinal motions (surge, heave, pitch) and lateral motions (sway, roll, yaw). And for a ship with port-starboard side symmetry, there are no hydrodynamical coupling between theses two.

$$(\mathbf{M} + \mathbf{A})\ddot{x} + \mathbf{B}\dot{x} + \mathbf{C}x = \mathbf{F}(t) \tag{1.2}$$

In the roll motion, the nonlinear terms in restoring and damping terms are essential for understanding the performance in roll. A typical restoring moment is shown in Figure 1.1.

If ignoring the coupling terms, the single-degree-of-freedom roll equation of motion can be

expressed as

$$(I_{44} + A_{44})\ddot{\phi} + B(\phi, \dot{\phi}) + \Delta GZ(\phi) = F(t) \tag{1.3}$$

in which, ϕ is the roll angle. I_{44} is the moment of inertial to the roll axis; A_{44} is the added mass in roll. The form of the damping term $B(\phi, \dot{\phi})$ has been discussed using empirical formula based on experimental data (for example Ikeda et al. [1976], Bikdash et al. [1994]). The restoring moment $GZ(\phi)$ is a polynomial obtained through curve fitting. Eq. (1.3) is used in Chapter 3 to predict capsize.

If there is no coupling between roll and surge motions, the single-degree-of-freedom surge motion is expressed as in Eq. (1.1(a)).

$$X = m\dot{u} \tag{1.4}$$

in which u is the velocity in surge direction. X is the forces in surge consisted of wave forces, propeller forces as well as resistance forces. In Chapter 4, this equation is used to predict threshold of global surf-riding.

For large motions, the coupling between longitudinal and lateral motions may exit. Parametric roll can be found as the coupling between roll and pitch motions when the frequency of roll and pitch are related. In Chapter 5, a heave-sway-roll coupling model is used (Chen et al. [1999]). The selection of coordinate systems is very important in ship dynamics. Sometimes a proper coordinate system can greatly simplify the problem. In Chapter 3, the body-fixed coordinate system is used to obtain the equations. The wave-fixed coordinate system is used in Chapters 4 and 5, which can greatly simplify the problem.

1.4 Nonlinear vessel dynamics

As mentioned in previous sections, the dynamics related to single-degree-of-freedom ship capsize is called a *homoclinic tangency* or a *heteroclinic tangency* (Spyrou and Thompson [2000]). The homoclinic case is related to ship capsize problem with water on deck as shown in Figure 1.2. The heteroclinic case is the classic capsize model as shown in Figure 1.1. When the tangency occurs, the stable and unstable manifolds originating from same saddle coincide (homoclinic orbit) or from different saddles coincide (heteroclinic orbit). Increasing some critical parameters will lead to chaotic motions, which means orbit starting from a certain initial condition develops in a random manner or the presence of a critical sensitivity to initial conditions (Guckenheimer and Holmes [2002]). For the ship capsize models, the saddle points correspond to angles of vanishing stability. If the roll angle is beyond the angle of vanishing stability, there is no restoring moment available. Thus, the vessel will capsize. The occurrence of chaotic motions can be used as a warning of potential capsize.

Another nonlinear dynamics behavior that is studied in ship dynamics is called a *homoclinic connection* (see for example Guckenheimer and Holmes [2002]). This phenomena is related to surf-riding in ship dynamics (Spyrou and Thompson [2000]) discussed in Chapter 4. In a recent IMO document the onset of surf-riding is described as follows: "when a ship is situated on the steep forefront of a high wave in following or quartering sea conditions, the ship can be accelerated to ride on the wave" (IMO [2007]). As mentioned earlier this phenomenon may work as precursor of broaching. Before the homoclinic connection, the system possesses periodic motions in phase plane which corresponds to the periodic surging motion in ship dynamics. After the homoclinic connection, the orbits are attracted to the nearby sink which corresponds to global surf-riding in ship dynamics.

1.5 Background on method of manufactured solution

This dissertation also used the method of manufactured solutions for chaotic dynamical systems. The purpose of this work is to demonstrate the usefulness of applying the method of manufactured solutions to the investigation and understanding of simulations of chaotic systems.

Numerical code development requires systematic verification and validation (V&V) of any tool developed where verification and validation are defined as follows:

- Verification: The process of ensuring that the simulations are sufficiently accurate approximations of the solution to the continuous mathematical model. (*i.e.*, are you solving the equations correctly?)
- Validation: the process of demonstrating that the mathematical model represents the physical reality for the intended usage of the model. (*i.e.* are you solving the correct equations?)

These definitions are broadly used and consistent with AIAA [1998], ASME Performance Test Code Committee 60 [2006], Department of Defense [2003] and the Department of the Navy [1999]. Verification can be further divided as code verification and solution verification (Oberkampf and Roy [to appear 2010], Roache [1998]). Solution verification estimates numerical errors, while code verification is primarily used to find mistakes in the computer code by comparing to benchmark solutions. Ideally, the benchmark solutions are exact analytical solutions to the mathematical model; however, analytical solutions do not exist for most cases. The method of manufactured solution (MMS) provides a way to generate analytical solutions for complex mathematical models. MMS was originally proposed by Steinberg and Roache [1985]. Shih [1985] was among the first to apply MMS to code debugging. The MMS

has been applied to code verification in computational fluid dynamics (Roache [2002], Roy et al. [2004]) and computational solid mechanics (ASME Performance Test Code Committee 60 [2006], Batra and Liang [1997]) and many other fields.

Yee *et al* have done a great deal of work investigating the application of nonlinear dynamics theory to computational fluid mechancis (Yee and Sweby [1994, 1996, 1997], Yee et al. [1997]). In this research, the standard approach in CFD-MMS is applied to nonlinear dynamics problems. We are trying to determine whether MMS can be used to increase the efficiency of numerical solutions to chaotic systems. Chaotic systems are identified as dynamical systems whose behavior is highly sensitive to initial conditions. Generally speaking, the MMS is applied with relatively loose error tolerances. Those specific cases where the MMS solution and numerical solution have significant difference are identified as requiring further investigation. The purpose of this work is to go through the large region of parameter space of initial conditions with loose error tolerances and only further refine those data showing numerical errors in a related MMS problem using tight error tolerences. In the first part of the work, two classic chaotic models are applied, followed by two ship capsize models. This thesis shows the work of Wu et al. [2009a].

1.6 Summary of coming chapters

Chapter 2 first introduces the physical meaning of Melnikov's function and the details on how the standard Melnikov's integral is calculated for single-degree-of-freedom dynamical system which possesses a Hamiltonian as unperturbed sub-system. Then the extended Melnikov's method is obtained for the 1 DOF dynamical system which the unperturbed sub-system is a non-Hamiltonian. At last, the Melnikov's method for slowly varying dynamical system is discussed.

In Chapter 3, two single-degree-of-freedom roll models are analyzed. When the linear damping term is assumed to be large, the extended Melnikov's method is applied to calculate the critical forcing beyond which the ship may capsize. The results are compared to numerical simulation results as well as standard Melnikov's method results to show the validity of this method. Safe basins are obtained to show how the change of wave force can result in the rapid erosion of safe region in phase space.

Chapter 4 is the application of the extended Melnikov's method on a 1DOF surge model related to surf-riding problem. The mathematical model is discussed which contains resistance, thrust from propeller and wave force in surge direction. This method is applied to predict global surf-riding by first treating the linear damping term as large, and then both linear and nonlinear damping terms are treated as large. Numerical results are obtained to compared with the results from extended Melnikov's method.

Chapter 5 is an initial trial of using the extended Melnikov's method to a multi-degree-of-freedom system in ship dynamics. This system is reduced to a slowly varying system from a roll-heave-sway coupled model. The extended Melnikov's method is used by assuming the quadratic damping term is large. The results are compared with those from standard Melnikov's method.

In Chapter 6, the method of manufactured solution is first applied to two classic chaotic models: Lorenz and Rössler oscillators. Simple sinusoidal functions are chosen as manufactured solutions for both cases. Numerical simulations are carried out using different values of error tolerances. The convergent region from chaotic control theory is used to help understand the system. This is followed by the analysis of the two ship capsize models discussed in Chapter 3. Similar simulations are performed with different precisions and values of error tolerances. The computational time has been kept to show how the method of manufactured solution can potentially improve computational efficiency. At last, other manufactured solu-

tions are tried for the same models to see how the form of manufactured solution influences the solutions.

Chapter 7 is a brief review of the practical impact of this dissertation: the application of the extended Melnikov's method to nonlinear ship dynamics and the application of the method of manufactured solution to chaotic dynamical systems simulation.

Chapter 8 is the summary of what have been learned in this dissertation and some recommendations on future work.

Chapter 2

Melnikov's Method

2.1 Melnikov's method for single-DOF dynamical systems

Melnikov's method is one of relatively few analytical methods used to predict the global behavior of dynamical systems. The idea was first presented by Melnikov [1963]. The basic concept is to use the solutions of the unperturbed Hamiltonian system to obtain the solutions of the perturbed system (Guckenheimer and Holmes [2002]). This method has been discussed in many nonlinear dynamics works (e.g. Guckenheimer and Holmes [2002] and Nayfeh and Balachandran [1995]). This section followed the procedure of derivation of Melnikov's function in Guckenheimer and Holmes [2002].

For a dynamic system expressed in Eq. (2.1),

$$\dot{\mathbf{x}} = \mathbf{f}(\mathbf{x}) + \varepsilon \mathbf{g}(\mathbf{x}, t); \qquad \mathbf{x} \in \mathbb{R}^2 \tag{2.1}$$

$\dot{\mathbf{x}} = \mathbf{f}(\mathbf{x})$ is assumed to be a Hamiltonian, which possesses a homoclinic or heteroclinic orbit. $\varepsilon\mathbf{g}(\mathbf{x}, t)$ represents periodic small perturbation terms. Let $\mathbf{q}^0(t - t_0)$ be the homoclinic orbit of $\dot{\mathbf{x}} = \mathbf{f}(\mathbf{x})$. $\mathbf{q}^s_\varepsilon(t, t_0)$ and $\mathbf{q}^u_\varepsilon(t, t_0)$ are the stable and unstable orbits of the perturbed system Eq. (2.1), respectively. These stable and unstable orbits can be mathematically expressed as the sum of the unperturbed orbits and a perturbation term $\mathbf{q}^{u,s}_1(t)$. Under these expressions, the distance between the stable and unstable manifolds becomes the distance between the perturbation terms.

By definition, the Melnikov's function is the distance of the separation between stable and unstable orbits projected on the normal of the unperturbed manifolds. The time dependent distance function can be defined as

$$\begin{aligned} d(t, t_0) &= \frac{\varepsilon\Delta(t)}{\|\mathbf{f}(\mathbf{q}^0(t - t_0))\|} \\ &= \varepsilon\frac{\mathbf{f}(\mathbf{q}^0(t - t_0)) \wedge (\mathbf{q}^u_1(t, t_0) - \mathbf{q}^s_1(t, t_0))}{\|\mathbf{f}(\mathbf{q}^0(t - t_0))\|} \\ &\overset{def}{=} \varepsilon\frac{\Delta^u(t, t_0) - \Delta^s(t, t_0)}{\|\mathbf{f}(\mathbf{q}^0(t - t_0))\|} \end{aligned} \tag{2.2}$$

The time derivative of $\Delta^u(t, t_0)$ is then

$$\dot{\Delta}^u(t, t_0) = D\mathbf{f}(\mathbf{q}^0(t - t_0))\dot{\mathbf{q}}^0(t - t_0) \wedge \mathbf{q}^u_1(t, t_0) + \mathbf{f}(\mathbf{q}_0(t - t_0)) \wedge \dot{\mathbf{q}}^u_1(t, t_0) \tag{2.3}$$

where $D\mathbf{f}(\mathbf{q}^0)$ is the Jacobian matrix of $\mathbf{f}$ at $\mathbf{q}^0$.

After some mathematical formulation, we have

$$\dot{\Delta}^u(t, t_0) = Trace D\mathbf{f}(\mathbf{q^0})(\mathbf{f}(\mathbf{q}^0) \wedge \mathbf{q}^u_1) + \mathbf{f}(\mathbf{q}^0) \wedge \mathbf{g}(\mathbf{q}^0, t) \tag{2.4}$$

Since $\mathbf{f}(\mathbf{q}^0)$ is a Hamiltonian, $TraceD\mathbf{f}(\mathbf{q}^0) = 0$, and Eq. (2.4) is simplified to

$$\dot{\Delta}^u(t, t_0) = \mathbf{f}(\mathbf{q}^0(t - t_0)) \wedge \mathbf{g}(\mathbf{q}^0(t - t_0), t) \tag{2.5}$$

Similarly,

$$\dot{\Delta}^s(t, t_0) = \mathbf{f}(\mathbf{q}^0(t - t_0)) \wedge \mathbf{g}(\mathbf{q}^0(t - t_0), t) \tag{2.6}$$

Integrating Eq. (2.5) and Eq. (2.6) on $(-\infty, t_0]$ and $[t_0, \infty)$ respectively,

$$\Delta^u(t_0, t_0) - \Delta^u(-\infty, t_0) = \int_{-\infty}^{t_0} \mathbf{f}(\mathbf{q}^0) \wedge \mathbf{g}(\mathbf{q}^0, t)dt \tag{2.7a}$$

$$\Delta^s(+\infty, t_0) - \Delta^s(t_0, t_0) = \int_{t_0}^{+\infty} \mathbf{f}(\mathbf{q}^0) \wedge \mathbf{g}(\mathbf{q}^0, t)dt \tag{2.7b}$$

When $t \to -\infty$, $\mathbf{q}^0$ approaches the saddle; $\mathbf{f}(\mathbf{q}^0) = 0$. Therefore $\Delta^u(-\infty, t) = 0$. Similarly, $\Delta^s(t, +\infty) = 0$. Adding Eq. (2.7a) and Eq. (2.7b) together, we have

$$\begin{aligned} \Delta^u(t_0, t_0) - \Delta^s(t_0, t_0) &= \int_{-\infty}^{+\infty} \mathbf{f}(\mathbf{q}^0(t)) \wedge \mathbf{g}(\mathbf{q}^0(t), t + t_0)dt \\ &= M(t_0) \end{aligned} \tag{2.8}$$

This is the form that is used to calculate the Melnikov's function.

2.2 Melnikov's function for system with large damping terms

The Melnikov's function in Eq. (2.8) is based on the assumption that $\dot{\mathbf{x}} = \mathbf{f}(\mathbf{x})$ is a Hamiltonian and all the perturbation terms are small. However, in the real engineering and physical world, there are many systems for which some perturbation terms cannot be assumed to be small. For example, in ship dynamics, the damping forces in surge, pitch, heave, sway and yaw cannot be assumed to be small. In order to address the constraint of small damping, Salam [1987]'s extended Melnikov's method is applied to ship dynamics in Chapter 3 and Chapter 4. This section presents a summary of obtaining the extended Melnikov's method in Salam [1987].

Salam [1987] started with the same dynamical system as in Eq. (2.1). $\dot{\mathbf{x}} = \mathbf{f}(\mathbf{x})$ still contains a homoclinic (or heteroclinic) orbit. But since the damping terms cannot be assumed to be small, they cannot be grouped in $\mathbf{g}$. In this case, these terms have to be group in $\mathbf{f}(\mathbf{x})$. Therefore, $\mathbf{f}(\mathbf{x})$ is no longer a Hamiltonian. The same assumptions and procedures can be followed as the standard Melnikov's method to obtain the distance function $\Delta^s(t, t_0)$ and $\Delta^u(t, t_0)$. And the same differential equations can be obtained as shown in Eq. (2.4). The first term in this equation cannot be eliminated due to the fact that $\mathbf{f}$ is not Hamiltonian. Thus $\Delta^u(t, t_0)$ cannot be solved directly by integrating Eq. (2.4).

Let $a(t-t_0) = TraceD\mathbf{f}(\mathbf{q}^0(t-t_0))$ and $b(t-t_0) = \mathbf{f}(\mathbf{q}^0(t-t_0)) \wedge \mathbf{g}(\mathbf{q}^0(t-t_0), t)$. Multiplying $\exp[\int_t^{t_0} a(s-t_0)ds]$ on both sides of Eq. (2.4). This equation can now be expressed as

$$\frac{d}{dt}\left[\Delta^u(t, t_0)\exp\left[\int_t^{t_0} a(s-t_0)ds\right]\right] = b(t-t_0)\exp\left[\int_t^{t_0} a(s-t_0)ds\right] \tag{2.9}$$

Integrate both sides of Eq. (2.9) from $-\infty$ to t_0, we have

$$\begin{aligned}\Delta^u(t_0,t_0) = \quad & \left\{\exp\left[\int_t^{t_0} a(s-t_0)ds\right]\right\}\Delta^u(-\infty,t_0) \\ & + \int_{-\infty}^{t_0} b(t'-t_0)\left\{\exp\left[\int_{t'}^{t_0} a(s-t_0)ds\right]\right\}dt' \end{aligned} \tag{2.10}$$

Similar forms of equation for $\Delta^s(t_0,t_0)$ can be obtained

$$\begin{aligned}\Delta^s(t_0,t_0) = \quad & \left\{\exp\left[-\int_{t_0}^{t} a(s-t_0)ds\right]\right\}\Delta^s(+\infty,t_0) \\ & - \int_{t_0}^{+\infty} b(t'-t_0)\left\{\exp\left[-\int_{t_0}^{t'} a(s-t_0)ds\right]\right\}dt' \end{aligned} \tag{2.11}$$

Salam [1987] proved that $\left\{\exp\left[-\int_{t_0}^{t} a(s-t_0)ds\right]\right\}\Delta^s(t,t_0)$ tends to 0 when $t\to+\infty$. And similarly, $\left\{\exp\left[\int_{t}^{t_0} a(s-t_0)ds\right]\right\}\Delta^u(t,t_0)$ tends to 0 when $t\to-\infty$. The first terms in Eq. (2.10) and Eq. (2.11) can be eliminated. The final form of the Melnikov's function is

$$\begin{aligned} M(t_0) &= \Delta^u(t_0.t_0) - \Delta^s(t_0.t_0) \\ &= \int_{-\infty}^{\infty} \mathbf{f}(\mathbf{q}^0)\wedge\mathbf{g}(\mathbf{q}^0,t+t_0)\left\{\exp\left[-\int_0^t TraceD\mathbf{f}(\mathbf{q}^0)ds\right]\right\}dt \end{aligned} \tag{2.12}$$

This is the form of Melniko'v function for highly dissipative systems. It is worth mentioning that $Trace\mathbf{A}$ can be either constant or time dependent. And when $Trace\mathbf{A}=0$, it reduces to the standard Melnikov's function.

Essentially to the implementation of Melinkov's method is the presence of a heteroclinic (or homoclinic) orbit in the unperturbed sub-system. The existence of such an orbit remains essential in the new formulation; and, if it does not arise naturally, it has to be artificially created, yet it should be done in such a way that does not violate the structure of the system studied in the first place. For this, it often suffices to introduce an initially unknown

constant σ, whose value could be identified on the basis of the condition of formation of a heteroclinic orbit. This constant is subsequently subtracted when the original (i.e. the "perturbed") system is examined. Hence this constant should represent a "small" quantity, so that the final system remains identical to the original one. Thereafter, the integration over the heteroclinic (or homoclinic) orbit that is required for the application of the Melnikov's method, can be performed without difficulties. Figure 2.1 shows how the value of the constant

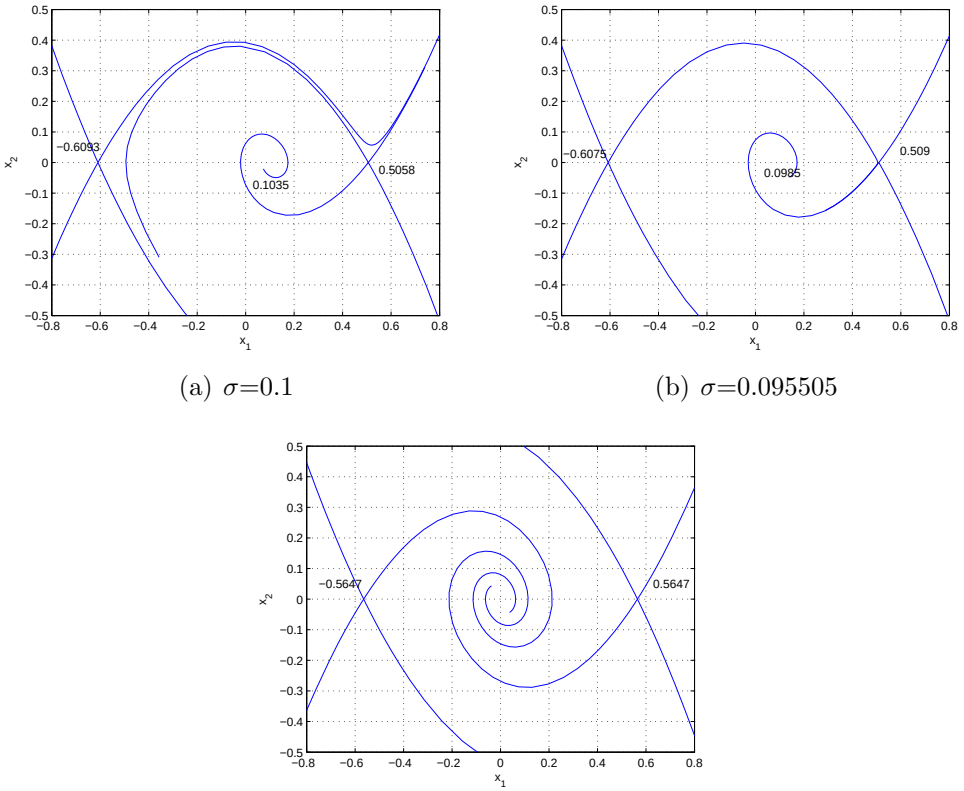

(a) σ=0.1

(b) σ=0.095505

(c) σ=0

Figure 2.1: Phase planes of the unperturbed sub-system for different σ.

will influence the unperturbed system. When σ is relatively "small", as shown in Figure 2.1(c), the stable and unstable manifolds separate. When σ is relatively large, the stable and unstable manifolds also separate as shown in Figure 2.1(a). For some intermediate value of σ in Figure 2.1(b), a saddle to saddle connection can be realized. The stable and unstable

manifolds intersect tangentially. This is the heteroclinic orbits that are needed. The system now is

$$\dot{\mathbf{x}} = \mathbf{f(x)} + \sigma + \varepsilon(\mathbf{g(x,t)} - \sigma/\varepsilon) = \tilde{\mathbf{f}}(\mathbf{x}) + \varepsilon\tilde{\mathbf{g}}(\mathbf{x}, t) \tag{2.13}$$

By adding σ in $\mathbf{f}$ and subtracting it in $\mathbf{g}$, the original dynamical system does not change. But the unperturbed and perturbed systems defined in the Melnikov's function do become different. The Melnikov's function in this case becomes

$$M(t_0) = \int_{-\infty}^{\infty} \tilde{\mathbf{f}}(\tilde{\mathbf{q}}^0(t)) \wedge \tilde{\mathbf{g}}(\tilde{\mathbf{q}}^0(t), t + t_0) \left\{ \exp\left[- \int_0^t Trace D\tilde{\mathbf{f}}(\tilde{\mathbf{q}}^0(s)) ds \right] \right\} dt \tag{2.14}$$

where $\tilde{\mathbf{q}}^0(t)$ is the heteroclinic orbit of $\tilde{\mathbf{f}}$.

In particular for calculating σ, two points are selected in the vicinity of the saddle of the unperturbed sub-system of $\tilde{\mathbf{q}}^0(t)$, one very close to its outset and the other very close to its inset (their directions are known from linear analysis around the saddle - to be noted that we refer to a cylindrical phase plane where the two saddles of the sub-system coincide). The unstable manifold coming from the one fixed point will end up at the other one in finite time T. The coordinates of these points (x_1, x_2) can be expressed in terms of σ. Moreover, the coordinates of the heteroclinic orbit (X, Y) are functions of σ and T. Then there are two equations and two unknowns.

$$\begin{aligned} F_1(T, \sigma) &= X(T, \sigma) - x_1(\sigma) = 0 \\ F_2(T, \sigma) &= Y(T, \sigma) - x_2(\sigma) = 0 \end{aligned} \tag{2.15}$$

The value of σ can be determined by numerically solving Eq. (2.15) using the Newton-

Raphson method according to the scheme described by (2.16).

$$\begin{pmatrix} T_{k+1} \\ \sigma_{k+1} \end{pmatrix} = \begin{pmatrix} T_k \\ \sigma_k \end{pmatrix} - \begin{pmatrix} J_1 & J_2 \\ J_3 & J_4 \end{pmatrix}^{-1} \begin{pmatrix} F_1(T_k, \sigma_k) \\ F_2(T_k, \sigma_k) \end{pmatrix}. \tag{2.16}$$

$J_i, i = 1, ..., 4$ are the elements of the Jacobian matrix of $\begin{pmatrix} F_1(T_k, \sigma_k) \\ F_2(T_k, \sigma_k) \end{pmatrix}$. Each term can be calculated numerically using the chain rule. Details of obtaining the value of σ can be found in Endo et al. [1989].

2.3 Melnikov's method for multi-degree-of-freedom system

The Melnikov's functions we discussed so far are for the dynamical systems with single-degree-of-freedom, which have 2 dimensional phase plane. However, not every dynamical system is or can be reduced to single-degree-of-freedom system. In order to extend the idea of Melnikov's method to multiple-degree-of-freedom systems, Wiggins and Holmes [1987] obtained Melnikov's function for 3 dimensional flows. The derivation of Melnikov's function described by Wiggins and Holmes [1987] has been summarized in this section.

The system they considered is in the form of Eq. (2.17). Systems like this are called slowly varying system, in which z is the slowly varying term. When $\varepsilon = 0$, the unperturbed

sub-system has a planar Hamiltonian $H(x, y, z)$ which satisfies Eq. (2.18).

$$\begin{aligned} \dot{x} &= f_1(x, y, z) + \varepsilon g_1(x, y, z) \\ \dot{y} &= f_2(x, y, z) + \varepsilon g_2(x, y, z) \\ \dot{z} &= \varepsilon g_3(x, y, z) \end{aligned} \tag{2.17}$$

For every constant z, the system in Eq. (2.18) contains a plane homoclinic (or heteroclinic) orbit to a saddle point.

$$\begin{aligned} \dot{x} &= f_1(x, y, z) = \frac{\partial H}{\partial y} \\ \dot{y} &= f_2(x, y, z) = -\frac{\partial H}{\partial x} \\ \dot{z} &= 0 \end{aligned} \tag{2.18}$$

Wiggins and Holmes [1987] proposed the following proposition:

Proposition 1 *"Let* $\overline{g_3(\gamma(z))} = 1/T \int_0^T g_3(\gamma(z), s)ds$. *If there exists* $z_0 \in J$ *such that* $\overline{g_3(\gamma(z_0))} = 0$, *and* $(d/dz)\overline{g_3(\gamma(z_0))} \neq 0$, *then* $\gamma(z_0, \varepsilon) = \gamma(z_0) + \mathcal{O}(\varepsilon)$ *is a hyperbolic periodic orbit with period* T*."*

This proposition can be proven by the averaging theorem (Guckenheimer and Holmes [2002]). It can help us to find the periodic orbits in perturbed systems. And based on this proposition, the perturbed orbits can be expressed as the sum of the unperturbed orbits and a perturbation term, similar to the planar Melnikov's method.

The first variational equations for $\mathbf{q}_1^u$ and $\mathbf{q}_1^s$ can be obtained as in Eq. (2.19).

$$\dot{\mathbf{q}}_1^{u,s} = \begin{bmatrix} \dot{x}_1^{u,s} \\ \dot{y}_1^{u,s} \\ \dot{z}_1^{u,s} \end{bmatrix} = \begin{bmatrix} \frac{\partial f_1}{\partial x} & \frac{\partial f_1}{\partial y} & \frac{\partial f_1}{\partial z} \\ \frac{\partial f_2}{\partial x} & \frac{\partial f_2}{\partial y} & \frac{\partial f_2}{\partial z} \\ 0 & 0 & 0 \end{bmatrix} \begin{bmatrix} x_1^{u,s} \\ y_1^{u,s} \\ z_1^{u,s} \end{bmatrix} + \begin{bmatrix} g_1 \\ g_2 \\ g_3 \end{bmatrix} \tag{2.19}$$

In the perturbed phase space, the intersection of stable and unstable manifolds is expected to be one-dimensional. Therefore, the distance function can be defined as in Eq. (2.20).

$$\begin{aligned} d(t,t_0) &= \varepsilon \frac{(-f_2(\mathbf{q}^0(t-t_0)), f_1(\mathbf{q}^0(t-t_0)), 0) \cdot (\mathbf{q}_1^u(t,t_0) - \mathbf{q}_1^s(t,t_0))}{\|\mathbf{f}(\mathbf{q}^0(t-t_0))\|} \\ &= \varepsilon \frac{\Delta^u(t,t_0) - \Delta^s(t,t_0)}{\|\mathbf{f}(\mathbf{q}^0(t-t_0))\|} \end{aligned} \tag{2.20}$$

in which, "." is the dot product. $(-f_2(\mathbf{q}^0(t-t_0)), f_1(\mathbf{q}^0(t-t_0)), 0)$ is the normal to the $\mathbf{f}(\mathbf{q}^0(t-t_0))$. The distance function is measured the same way as previous as the distance of stable and unstable manifolds project on the normal of $\mathbf{f}(\mathbf{q}^0(t-t_0))$.

The time derivative of $\Delta^u(t,t_0)$ is

$$\begin{aligned} \dot{\Delta}^u(t,t_0) &= \left(\frac{\partial f_1}{\partial x}(\mathbf{q}^0) + \frac{\partial f_2}{\partial y}(\mathbf{q}^0) \right) \Delta^u(t,t_0) + f_1(\mathbf{q}^0) g_2(\mathbf{q}^0) - f_2(\mathbf{q}^0) g_1(\mathbf{q}^0) \\ &\quad + \left(f_1(\mathbf{q}^0) \frac{\partial f_2}{\partial z}(\mathbf{q}^0) - f_2(\mathbf{q}^0) \frac{\partial f_1}{\partial z}(\mathbf{q}^0) \right) z_1^u(t,t_0) \end{aligned} \tag{2.21}$$

Since the unperturbed sub-system is Hamiltonian, $\frac{\partial f_1}{\partial x}(\mathbf{q}^0) + \frac{\partial f_2}{\partial y}(\mathbf{q}^0) = 0$. Integrate Eq. (2.21) from $-\infty$ to t_0, we have

$$\Delta^u(t_0,t_0) - \Delta^u(-\infty,t_0) = \int_{-\infty}^{0} \left[f_1 g_2 - f_2 g_1 + (f_1 \frac{\partial f_2}{\partial z} - f_2 \frac{\partial f_1}{\partial z}) z_1^u(t,t_0) \right] dt \tag{2.22}$$

Similarly, we can have

$$\Delta^s(+\infty, t_0) - \Delta^s(t_0, t_0) = \int_0^{+\infty} \left[f_1 g_2 - f_2 g_1 + (f_1 \frac{\partial f_2}{\partial z} - f_2 \frac{\partial f_1}{\partial z}) z_1^s(t, t_0) \right] dt \qquad (2.23)$$

$\Delta^u(-\infty, t_0)$ and $\Delta^s(+\infty, t_0)$ are both zero due to the saddle points.

According to the fact that the unperturbed system is a Hamiltonian and z is constant for each unperturbed system, the Melnikov's function can be finally reduced to the form of

$$\begin{aligned} M(t_0) &= \int_{-\infty}^{+\infty} \left(f_1 g_2 - f_2 g_1 + \frac{\partial H}{\partial z} g_3 \right) (\mathbf{q}^0(t), t + t_0) dt - \frac{\partial H}{\partial z}(\gamma(z_0)) \int_{-\infty}^{+\infty} g_3(\mathbf{q}_0(t), t + t_0) dt \\ &= \int_{-\infty}^{+\infty} (\nabla H \cdot \mathbf{g})(\mathbf{q}^0(t), t + t_0) dt - \frac{\partial H}{\partial z}(\gamma(z_0)) \int_{-\infty}^{+\infty} g_3(\mathbf{q}_0(t), t + t_0) dt \qquad (2.24) \end{aligned}$$

where H is the Hamiltonian from the unperturbed sub-system as mentioned before. If g_3 is zero, Eq. (2.24) is reduced to the Melnikov's function for single-degree-of-freedom system as in Eq. (2.8). The additional term is coming from the slowly varying variable z. Based on the theorem in Wiggins and Holmes [1987], if the Melnikov's function in Eq. (2.24) has simple zeros, the stable and unstable manifolds intersect transversly, which means chaotic dynamics may occur.

2.4 Melnikov's method for multi-DOF system with large damping

If the damping terms in the fast dynamics in Eq. (2.17) cannot be assumed to be small, then they have to be grouped in the unperturbed sub-system. This unperturbed sub-system is no longer a Hamiltonian. The first term in Eq. (2.21) cannot be eliminated. Let $a(t - t_0) = \partial f_1/\partial x(\mathbf{q}^0) + \partial f_2/\partial y(\mathbf{q}^0)$. Similar to the approach of Salam [1987] which is summarized

in Section 2.2, to solve Eq. (2.21), $\exp[\int_t^{t_0} a(s-t_0)ds]$ is multiplied to both sides of the equation. Then integrate from $-\infty$ to t_0, we have

$$\begin{aligned}\Delta^u(t_0,t_0) - \Delta^u(-\infty,t_0)\exp\left[\int_{-\infty}^{t_0} a(s-t_0)ds\right] = \\ \int_{-\infty}^{t_0}(f_1g_2 - f_2g_1)\left\{\exp\left[\int_t^{t_0} a(s-t_0)ds\right]\right\}dt + \\ \int_{-\infty}^{t_0}(f_1\frac{\partial f_2}{\partial z} - f_2\frac{\partial f_1}{\partial z})z_1^u(t,t_0)\left\{\exp\left[\int_t^{t_0} a(s-t_0)ds\right]\right\}dt \end{aligned} \tag{2.25}$$

Similarly, we can have

$$\begin{aligned}\Delta^s(\infty,t_0)\exp\left[\int_{\infty}^{t_0} a(s-t_0)ds\right] - \Delta^s(t_0,t_0) = \\ \int_{t_0}^{+\infty}(f_1g_2 - f_2g_1)\left\{\exp\left[\int_t^{t_0} a(s-t_0)ds\right]\right\}dt + \\ \int_{t_0}^{+\infty}(f_1\frac{\partial f_2}{\partial z} - f_2\frac{\partial f_1}{\partial z})z_1^s(t,t_0)\left\{\exp\left[\int_t^{t_0} a(s-t_0)ds\right]\right\}dt \end{aligned} \tag{2.26}$$

In this case, the unperturbed sub-system still contains a planar homoclinic orbit connecting to the saddle. From Eq. (2.20), the distance function is defined as $\Delta^u(t,t_0) = (-f_2(\mathbf{q}^0), f_1(\mathbf{q}^0), 0)\cdot \mathbf{q}_1^u$, in which $\mathbf{q}^0$ is the new homoclinic orbit in this case. Therefore, similar to the proof in Section 2.2, $\Delta^u(-\infty,t_0)\exp\left[\int_{-\infty}^{t_0} a(s-t_0)ds\right]$ approaches zero. Similarly, $\Delta^s(\infty,t_0)\exp\left[\int_{\infty}^{t_0} a(s-t_0)ds\right]$ approaches zero.

$z^{s,u}(t,t_0)$ can be solved by integrating Eq. (2.19),

$$z_1^{s,u}(t,t_0) = \int_{t_0}^{t} g_3(\mathbf{q}^0(s-t_0),s)ds \tag{2.27}$$

Adding Eq. (2.25) and (2.26), and substituting Eq. (2.27), the Melnikov's function in this

case is

$$\begin{aligned}
&\Delta^u(t_0,t_0)-\Delta^s(t_0,t_0)= \\
&\int_{-\infty}^{+\infty}(f_1g_2-f_2g_1)\left\{\exp\left[\int_0^t a(s)ds\right]\right\}dt+ \\
&\int_{-\infty}^{+\infty}(f_1\frac{\partial f_2}{\partial z}-f_2\frac{\partial f_1}{\partial z})\int_0^t g_3(\mathbf{q}^0,s+t_0)ds\left\{\exp\left[\int_0^t a(s)ds\right]\right\}dt
\end{aligned} \tag{2.28}$$

As mentioned in Section 2.4, in order to obtain a homoclinic orbit from the unperturbed sub-system, a constant σ is added to the unperturbed system. The dynamical system is now in the form of

$$\begin{aligned}
\dot{x} &= f_1(x,y,z)+\varepsilon(g_1(x,y,z)) \\
\dot{y} &= f_2(x,y,z)+\sigma+\varepsilon(g_2(x,y,z)-\sigma/\varepsilon) \\
\dot{z} &= \varepsilon g_3(x,y,z)
\end{aligned} \tag{2.29}$$

in which the unperturbed sub-system in Eq. (2.30) possessed a homoclinic orbit $\tilde{\mathbf{q}}^0$.

$$\begin{aligned}
\dot{x} &= f_1(x,y,z) \\
\dot{y} &= f_2(x,y,z)+\sigma
\end{aligned} \tag{2.30}$$

2.5 Summary

In this chapter, the Melnikov's function of different forms has been summarized (for example Guckenheimer and Holmes [2002], Salam [1987] and Wiggins and Holmes [1987]). The physical meaning of the Melnikov's function is the distance between the perturbed stable and unstable manifolds projected on the line which is perpendicular to the unperturbed

manifolds. If the distance is zero and the first derivative is not zero, the stable and unstable manifolds intersect transversely. According to the Smale-Birkhoff homoclinic theorem, this kind of orbits implies *Smale horseshoe*, *i.e.* chaos may occur (Guckenheimer and Holmes [2002]). Therefore, the Melnikov's function can be used to predict the occurrence of chaos in dynamical systems.

By only solving the unperturbed sub-system, the Melnikov's function can show the property of the whole dynamical system. Therefore, it has great computational advantage compared to numerical methods. The standard Melnikov's method has been reviewed for both planar system and slowly varying system. The advantage of the standard Melnikov's method is that if we can solve the unperturbed sub-system analytically, we can have the Melnikov's function in closed-form. However, the constraint of the standard Melnikov's method is the unperturbed sub-system needs to be a Hamiltonian. In order to address this constraint, the extended Melnikov's function for both planar and slowly varying systems are discussed. The extended Melnikov's function can deal with systems with non-Hamiltonian unperturbed sub-systems. However one cannot obtain closed-form Melnikov's function anymore. This is one of the disadvantages of the extended Melnikov's method.

In the following chapters, the extended Melnikov's method has been applied to several dynamical systems which represent a cross section of vessel dynamical stability issues. The standard Melnikov's functions have also be calculated or referenced in order to compare the results.

Chapter 3

Melnikov's Method for the 1DOF Rolling Problem without Damping Constraint [1]

3.1 Introduction

Roll motion is one of the key motions related to a vessel's dynamic stability. The complexity of the problem is due to its strong nonlinear restoring moment GZ (such as Figure 1.1) and nonlinear damping terms. In recent years, nonlinear dynamics techniques have been applied in order to better understand the physical background of capsize (for example Thompson et al. [1987], Falzarano [1990] and Thompson [1997]). One of these methods is Melnikov's method. In the standard Melnikov's method, damping terms are required to be small so that they can be treated as perturbation terms. The small damping assumption is reasonable for one degree-of-freedom roll motion, but not typically true for other and/or multiple degree

[1] This chapter has in large part been published as Wu and McCue [2007] and Wu and McCue [2008].

of freedom motions. In order to extend this method for other and/or multiple degrees of freedom, the constraint of small damping must be addressed.

In this chapter, the extended Melnikov's method discussed in Section 2.2 is used to analyze ship motions without assuming small linear damping. Two single degree of freedom roll motion models are analyzed here as applications to this method.

3.2 Simple roll motion

The simple single-degree-of-freedom roll equation of motion from Falzarano [1990] is used here and given in Eq. (3.1).

$$(I_{44} + A_{44})\ddot{\phi} + B_{44}\dot{\phi} + B_{44q}\dot{\phi} \mid \dot{\phi} \mid + \Delta(C_1\phi + C_3\phi^3) = F\cos(\omega\tau) \tag{3.1}$$

In this equation, I_{44} is the moment of inertia of the ship about the roll axis. A_{44} is the added mass. B_{44} and B_{44q} are the linear and quadratic damping terms, respectively. $C_1\phi + C_3\phi^3$ is a cubic polynomial approximation for the restoring moment curve (GZ curve), in which C_1 is the linear restoring moment coefficient and C_3 is the nonlinear coefficient. For small angle rolling the linear restoring term is dominant. Therefore, the slope of GZ curve at the origin is GM. The nonlinear term is effective as roll angle increases. For a typical GZ curve, when the roll angle exceeds some angle dubbed the 'angle of vanishing stability', GZ becomes negative. This means the restoring moment becomes negative, which will results in the loss of stability as shown in Figure 1.1. This angle can be uniquely determined by the coefficients in the restoring moment. F is the amplitude of the external force due to induced wave with frequency ω. Following from Jiang et al. [2000], Eq. (3.1) can be scaled

into non-dimensional form

$$\ddot{x} + \delta_1 \dot{x} + \varepsilon\delta_2 \dot{x} \mid \dot{x} \mid + x - \alpha x^3 = \varepsilon f \cos(\Omega t) \tag{3.2}$$

where

$$\begin{aligned}
&\phi = x, \quad \omega_n = \sqrt{\frac{C_1\Delta}{I_{44} + A_{44}}}, \quad t = \omega_n \tau \\
&\Omega = \omega/\omega_n, \quad \delta_1 = \frac{B_{44}\omega_n}{C_1\Delta}, \quad \varepsilon\delta_2 = \frac{B_{44q}}{I_{44} + A_{44}}, \\
&\alpha = -\frac{C_3}{C_1}, \quad \varepsilon f = \frac{F}{C_1\Delta}.
\end{aligned}$$

The data for the $Patti - B$ from Jiang et al. [2000] is used here for convenient results comparison, as shown in Table 3.1. $Patti - B$ is an oft-studied fishing boat which capsized twice. Because a large volume of research has been done toward this ship, it is used here for easy comparison with other research work. Although A_{44}, B_{44} and B_{44q} are all functions of frequencies, for the non-dimensional equation, δ_1 and δ_2 are all taken as constants. This is because the damping coefficients are non-dimensionalized by Δ and $I + A_{44}$ respectively. These parameters are always at higher order than B_{44} and B_{44q}. Therefore, these non-dimensional coefficients do not change sharply in a small range of frequency, it is reasonable to assume they are constants within this range. Therefore, for the validity of these data, the formulation in this work are all carried out in a frequency range around the natural frequency.

Table 3.1: Data for non-dimensional parameters for $Patti - B$ from Jiang et al. [2000]

parameter	value
δ_1	0.0037
$\varepsilon\delta_2$	0.0672
α	3.1355

3.2.1 Calculation of Melnikov's integral for simple roll motion

In order to calculate the Melnikov's integration, Eq. (3.2) can be expressed in state-space form as

$$\mathbf{f} = \begin{bmatrix} x_2 \\ -\delta_1 x_2 - x_1 + \alpha x_1^3 + \sigma \end{bmatrix}$$
$$\varepsilon\mathbf{g} = \begin{bmatrix} 0 \\ f\cos(\Omega t) - \delta_2 x_2 \mid x_2 \mid -\sigma/\varepsilon \end{bmatrix}. \tag{3.3}$$

σ is added since the linear damping term is no longer treated to be small. Table 3.2 gives values of σ for different values of δ_1 [2]. 0.0037 is the linear damping coefficient for $Patti - B$, while 0.037 and 0.37 are artificially inflated values.

Table 3.2: Critical values of σ for different δ_1

δ_1	σ_c
0.0037	0.000985
0.037	0.009847
0.37	0.095505

The Melnikov's integral from Eq. (2.12) is

$$M(t_0) = f[\cos(\Omega t_0)I_1(\Omega) - \sin(\Omega t_0)I_2(\Omega)] - \delta_2 I_3 - \sigma_c I_4; \tag{3.4}$$

[2]Different values of δ_1 are used here to verify the effectiveness of this method for large linear damping ratios. This does not mean the actual linear damping ratio for roll motion will be large, in fact it is typically small. It is artificially inflated in this work to test the methodology prior to extending this concept to other degrees of freedom which will have large damping.

where

$$\begin{aligned} I_1(\Omega) &= \int_{-\infty}^{+\infty} x_2 \cos(\Omega t) \exp(\delta_1 t) dt; \\ I_2(\Omega) &= \int_{-\infty}^{+\infty} x_2 \sin(\Omega t) \exp(\delta_1 t) dt; \\ I_3 &= \int_{-\infty}^{+\infty} x_2^2 \mid x_2 \mid \exp(\delta_1 t) dt; \\ I_4 &= \int_{-\infty}^{+\infty} x_2 \exp(\delta_1 t) dt. \end{aligned}$$

The Melnikov integral has simple zeros if $M(t_0) = 0$ and $dM(t_0)/dt_0 \neq 0$.

The condition $M(t_0) = 0$ can be expressed as

$$f[\cos(\Omega t_0) I_1(\Omega) - \sin(\Omega t_0) I_2(\Omega)] - \delta_2 I_3 - \sigma_c I_4 = 0$$

Therefore, the critical amplitudes of external forcing that lead to chaotic motions and may therefore capsize is

$$f = \frac{\delta_2 I_3 + \sigma_c I_4}{\sqrt{I_1^2 + I_2^2}} \tag{3.5}$$

The condition $dM(t_0)/dt_0 \neq 0$ is equivalent to

$$\frac{dM(t_0)}{dt_0} = -\Omega f \cos(\Omega t_0) I_1 + \Omega f \sin(\Omega t_0) I_2 \neq 0 \tag{3.6}$$

The inequality holds when I_1 and I_2 are not both zero. Since Ωs are discrete constants, this is true for most Ω.

The standard Melnikov's integral found when treating δ_1 as a small term from Falzarano [1990] is given in Eq. (3.7) for convenient comparison

$$M(t_0) = \cos(\Omega t_0)\frac{f}{\sqrt{2\alpha}}\int_{-\infty}^{\infty} sech^2(\frac{t}{\sqrt{2}})\cos(\Omega t)dt - \frac{\delta_1}{2\alpha}\int_{-\infty}^{\infty} sech^4(\frac{t}{\sqrt{2}})dt$$
$$-\frac{\delta_2}{(2\alpha)^{3/2}}\int_{-\infty}^{\infty} sech^4(\frac{t}{\sqrt{2}})\left|sech^2(\frac{t}{\sqrt{2}})\right|dt \tag{3.7}$$

and the critical forcing amplitudes are

$$f_c = \frac{\frac{2\sqrt{2}\delta_1/\varepsilon}{3\alpha} + \frac{8\delta_2}{15\alpha^{3/2}}}{\frac{\pi\Omega\sqrt{2}}{\sqrt{\alpha}}csch(\frac{\Omega\pi}{\sqrt{2}})}. \tag{3.8}$$

3.2.2 Numerical simulation for simple roll motion

Since σ_c and T can be calculated for given δ_1, numerical integration is carried out to solve for the system $\mathbf{f}$ in Eq. (3.3) from 0 to T. Setting one of the saddle points as the initial condition, these ordinary differential equations can be numerically integrated using Runge-Kutta method. The values of points on heteroclinic orbit are obtained. Therefore, each term in Eq. (3.4) can be numerically integrated along this heteroclinic orbit from 0 to T.

The critical forcing is calculated for different linear damping ratios δ_1 and different Ω values as shown in Figure 3.1. These results are compared with Falzarano's results in Eq. (3.8). The remaining percentage of safe basin is also shown in Figure 3.1, as the results of numerical simulation of the system in Eq. (3.2).

The remaining percentage is the amount of remaining safe basin compared to the zero forcing case. When the linear damping ratios are $\delta_1 = 0.0037$ and $\delta_1 = 0.037$, the two Melnikov's methods get the same critical forcing, as shown in Figures 3.1(a) and 3.1(b). These results are conservative and all below the 90% remaining safe basin lines. This line shows the forcing

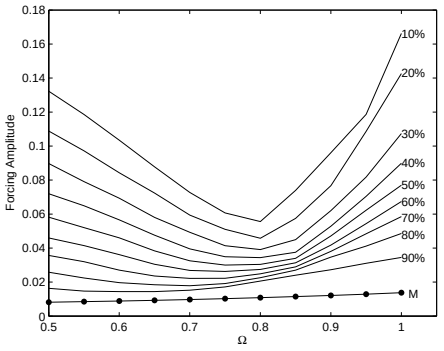

(a) δ_1=0.0037

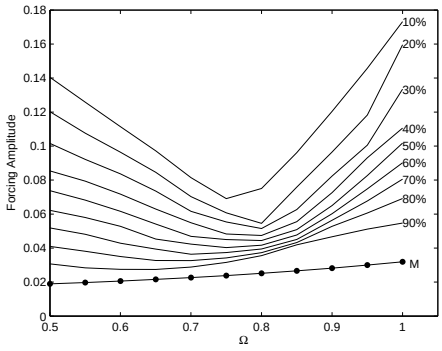

(b) δ_1=0.037

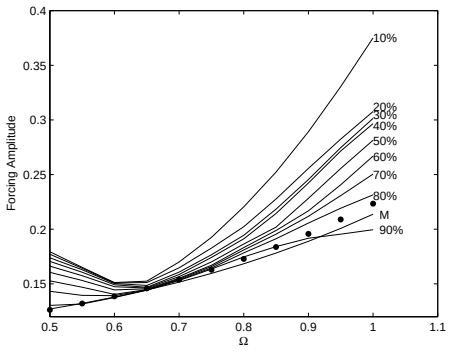

(c) δ_1=0.37

Figure 3.1: Critical forcing for different Ω at different δ_1 as well as the remaining of safe basin. '.': Critical forcing from extended Melnikov method. '-M': Critical forcing from Falzarano's results.

at which 90% of initial conditions will not lead to capsize compared to zero forcing case for different frequencies. When linear damping ratio is $\delta_1 = 0.37$, which cannot be treated as a small term, the results from the extended Melnikov method and Falzarano's results become different, as shown in Figure 3.1(c). As Ω gets larger, results obtained by using the extended Melnikov's method approach, or even exceed, the 90% remaining safe basin line. These results show the extended Melnikov method is properly applied and works for small damping, via comparison to the work of Falzarano [1990], and produces less conservative results as damping increases, an intuitive result. Safe basins for different frequency ratios, Ω, and forcing frequencies, f, are also plotted for the case $\delta_1 = 0.37$. This is calculated using 200×200 initial conditions within $-1.5 < x < 1.5$ and $-1.5 < \dot{x} < 1.5$. The system is integrated using each of the initial conditions for 10 cycles of external forcing period. If the roll angle is beyond the angle of vanishing stability within 10 cycles, which means the restoring moment becomes negative. The ship will lose stability. It is said to capsize at this initial condition, which is denoted as the dark region. If the roll angle is smaller than the angle of vanishing stability within this period, which means the ship still has positive restoring moment. The ship has the ability to gain stability, as shown in Figure 1.1. It is said to be safe for this initial condition, which corresponds to the blank region. Two typical cases of interest are considered here. One is $\Omega = 1.0$, which means the external force frequency is equal to the natural frequency of the system, as shown in Figure 3.2.

In this case, the extended Melnikov's method and the traditional one are all above the 90% safe basin remaining case. Figure 3.2(b) shows the onset of safe basin erosion at the critical height determined from the extended Melnikov's method lending validity to this extended method. The other case is $\Omega = 0.65$, as shown in Figure 3.3. From the numerical simulation in Figure 3.1, this is the case that the ship is most likely to capsize. The basin erosion appears numerically at a forcing amplitude just below the critical one predicted by the Melnikov's

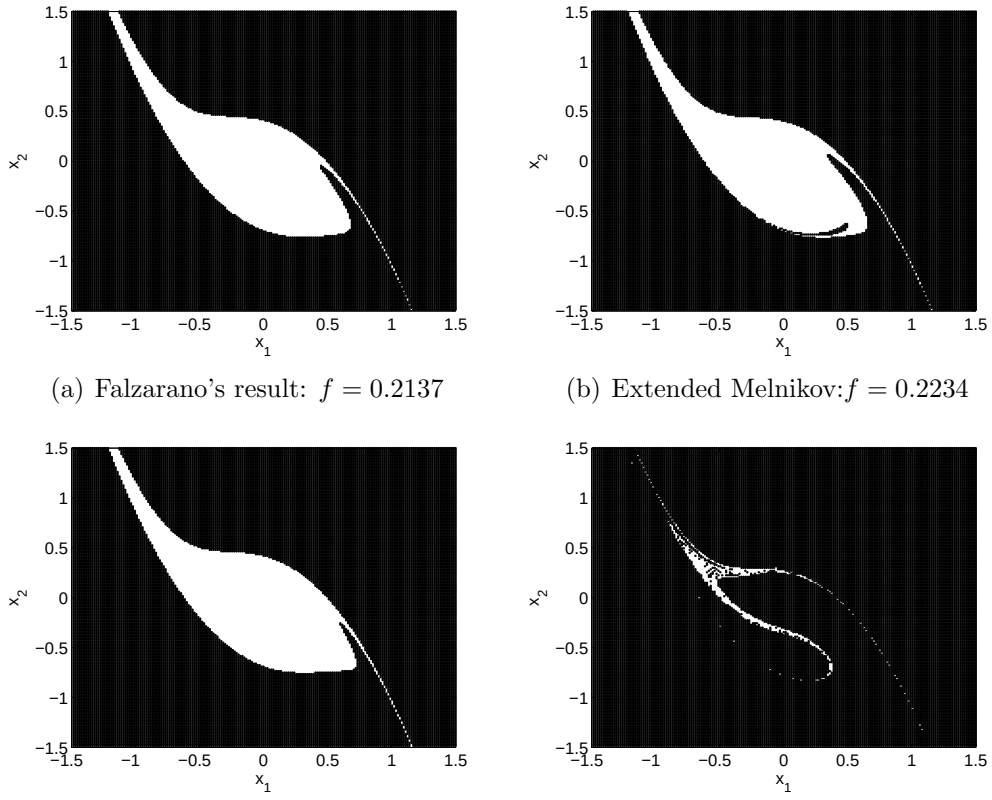

(a) Falzarano's result: $f = 0.2137$

(b) Extended Melnikov:$f = 0.2234$

(c) 90% safe basin remaining:$f = 0.1996$

(d) 10% safe basin remaining:$f = 0.3750$

Figure 3.2: Safe basin for different forcing at $\Omega = 1.0$ with $\delta_1 = 0.37$.

method. We believe this is due to the instability and tolerance of the numerical methods used, particularly considering the exceedingly small variation in forcing between Figures 3.3(a), 3.3(b) and 3.3(c). This is a region where all curves clump, persay, in Figure 3.1 and is thus highly sensitive to numerical variations.

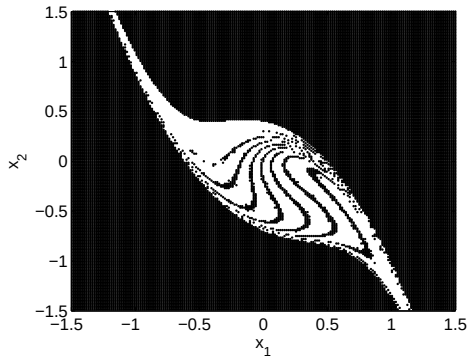

(a) Falzarano's result: $f = 0.1444$

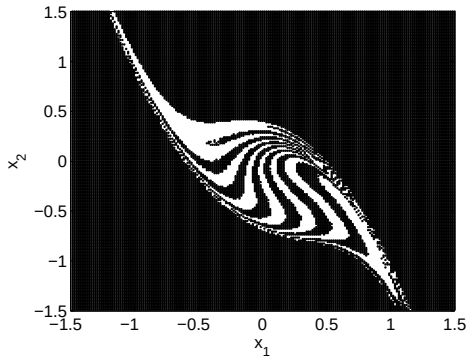

(b) Extended Melnikov: $f = 0.1458$

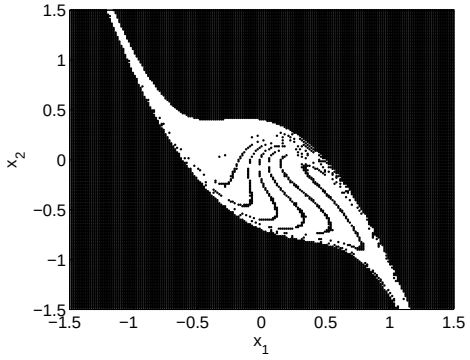

(c) 90% safe basin remaining:$f = 0.1442$

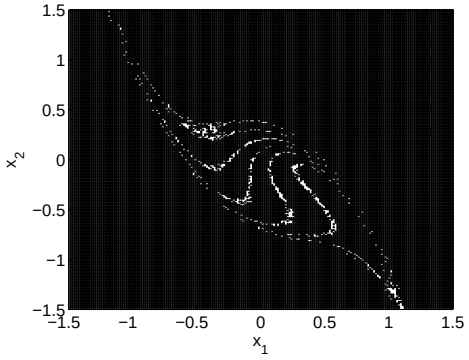

(d) 10% safe basin remaining:$f = 0.1525$

Figure 3.3: Safe basin for different forcing at $\Omega = 0.65$ with $\delta_1 = 0.37$.

3.3 Biased roll motion

The model of biased roll motion is from Spyrou et al. [2002]

$$\ddot{x} + \beta\dot{x} + x(1-x)(1+ax) = F\sin(\omega t) \tag{3.9}$$

in which a is a parameter between 0 and 1, and it is a measure of the amount of bias. Generally, the biased roll model is an approximation for ships affected by waves, winds or cargo shifting during large angles of roll. When $a = 1$, the restoring moment is a symmetric cubic polynomial, which means no bias. This is similar to Falzarano [1990] model. When $a = 0$, the restoring moment is a second order polynomial. This is the extreme case of bias. In this case, the ship can only capsize from one side. It is called Helmholtz-Thompson equation as shown in Thompson [1997] and Spyrou and Thompson [2000]. Spyrou et al. [2002] pointed out that in realistic situation, the value of a is closer to 1 than 0. Therefore, $(1 - a)$ is a small number. Eq. (3.9) can be expressed as

$$\ddot{x} + x - x^3 + \beta\dot{x} = (1 - a)(x^2 - x^3) + F\sin(\omega t) \tag{3.10}$$

3.3.1 Calculation of the Melnikov's integral for biased roll model

When calculating the Melnikov's integral, Eq. (3.10) is written in state-space form as

$$\begin{aligned} \dot{x_1} &= x_2; \\ \dot{x_2} &= -\beta x_2 - x_1 + x_1^3 + \sigma + \varepsilon[f\sin(\omega\tau) + \alpha(x_1^2 - x_1^3) - \sigma/\varepsilon]. \end{aligned} \tag{3.11}$$

in which $f = F/\varepsilon$, $\alpha = (1 - a)/\varepsilon$.

Similarly, the constant σ is added to create the heteroclinic orbits. Different values of σ_c are calculated for different damping ratio β as shown in Table 3.3.

Thus the Melnikov's function of this system is

$$M(t_0) = \int_{-\infty}^{\infty} x_2[f\sin(\omega t + t_0) - \sigma/\varepsilon + \alpha(x_1^2 - x_1^3)]\exp\left[\int_0^t \beta ds\right] dt \tag{3.12}$$

Table 3.3: Critical values of σ for different β

β	σ_c
0.05	0.023557
0.1	0.047036

The critical forcing according to the Melnikov's function is

$$f = \frac{I_3 - I_4}{\sqrt{I_1^2 + I_2^2}} \tag{3.13}$$

in which

$$\begin{aligned} I_1 &= \int_{-\infty}^{\infty} x_2 \sin(\omega\tau) \exp(\beta t) dt; \\ I_2 &= \int_{-\infty}^{\infty} x_2 \cos(\omega\tau) \exp(\beta t) dt; \\ I_3 &= \frac{\sigma}{\varepsilon} \int_{-\infty}^{\infty} x_2 \exp(\beta t) dt; \\ I_4 &= \alpha \int_{-\infty}^{\infty} (x_1^2 - x_1^3) x_2 \exp(\beta t) dt. \end{aligned}$$

Similar analysis can be carried out for this system for the existence of simple zeros. The critical forcing calculated by Spyrou et al. [2002] that assuming linear damping is small is listed in Eq. (3.14) for comparison.

$$f = \left(\frac{2\beta}{3} - \frac{\sqrt{2}(1-a)}{3} \right) \frac{\sinh \frac{\pi\omega}{\sqrt{2}}}{\pi\omega} \tag{3.14}$$

3.3.2 Numerical simulation for biased roll model

Similar to the simple roll model, these integrations can not be calculated analytically. Therefore, numerical integration is carried out. The critical forcing from the extended Melnikov

method and from Eq. (3.14) are both calculated for different values of β and a, as shown in Figures 3.4 and 3.5. These values are taken from Spyrou et al. [2002] for ready comparison [3]. Numerical simulation of Eq. (3.9) is carried out; the 90% remaining percentage lines are given for each case.

When the damping is relatively small, as shown in Figure 3.5, the critical forcing from the extended Melnikov method is almost the same as Spyrou's results. And they are both conservative compared with the 90% remaining safe basin line. When the damping gets a little bit larger, although both results are still conservative compared with 90% line, the critical forcing from the extended Melnikov method grows larger than Spyrou's results, as shown in Figure 3.4. The extent of bias also has influence on the results. For the same damping ratio, when the bias is larger, i.e. the a parameter is smaller, the extended Melnikov method will yield a less conservative value for critical forcing, as a direct comparison in Figure 3.4.

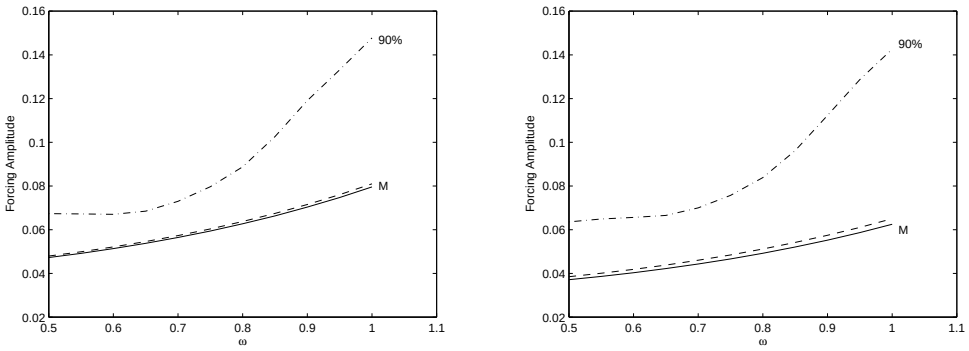

(a) $a = 0.975$ (b) $a = 0.95$

Figure 3.4: Critical forcing for different ω at $\beta = 0.1$. '-': Critical forcing from Spyrou's results. '–': Critical forcing from extended Melnikov method. '-.': Forcing at which 90% of safe basin left.

[3]These values are not for a specific ship. They were selected by Spyrou et al. [2002] to show the validity of the method.

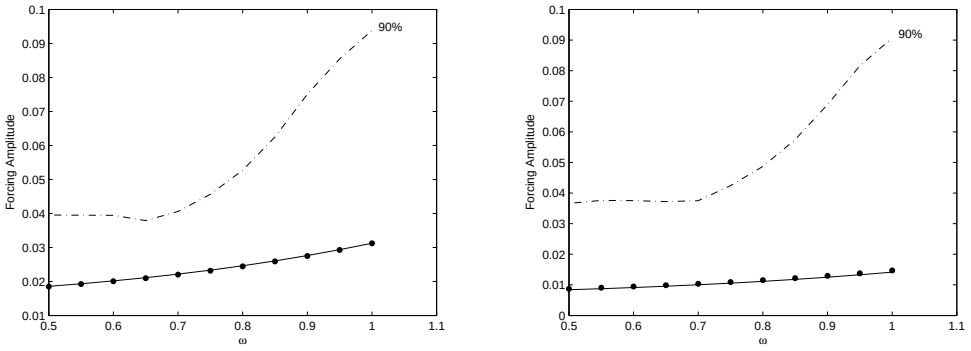

(a) $a = 0.975$ (b) $a = 0.95$

Figure 3.5: Critical forcing for different ω at $\beta = 0.05$. '-': Critical forcing from Spyrou's results. '.': Critical forcing from extended Melnikov method. '-.': Forcing at which 90% of safe basin left.

3.4 Conclusions

The extended Melnikov's method is applied to the roll equation of motion without the constraint of small linear damping. Results of this method coincide with the results from the standard Melnikov's method when damping is relatively small demonstrating feasibility and validating the approach to prior literature. This demonstration opens the possibility of using the Melnikov's method to calculate ship motions in other degrees of freedom or for multiple degrees of freedom problems, which do not necessarily have small damping. The extended Melnikov's method shows tremendous promise for predicting ship motions in other degrees of freedom, and even more complicated, multi-DOF motions, even when damping is significant.

Chapter 4

Melnikov's Method and the 1DOF Surf-riding Problem [1]

To the scientific community the phenomenon of surf-riding has been known for about 60 years and during this period it has been studied analytically, numerically and experimentally. The occurrence of surf-riding is determined by a combination of ship and environmental parameters; such as ship form, speed, heading angle, and wave characteristics. At the International Maritime Organization (IMO), the critical speed for the occurrence of surf-riding is defined semi-empirically as $V = 1.8\sqrt{L}/\cos(180 - \alpha)$ (knots) (L is the ship length and α is the angle of encounter)(IMO [2007]). This corresponds to a Froude number higher than, approximately, 0.3. However, this threshold refers to the first appearance of surf-riding from certain initial conditions; whereas global attraction to surf-riding occurs at a higher Froude number. Incidentally, the latter phenomenon has been identified as key for the manifestation of broaching-to behavior. For predicting the latter, one needs to apply advanced analytical techniques of strongly nonlinear systems, such as the Melnikov's method.

[1] This chapter has in large part been submitted for publication as Wu et al. [2009b] and part has been published as Wu and Spyrou [2009].

As mentioned in Chapter 1, the condition of global capture into surf-riding ("upper threshold") corresponds to a phenomenon that is referred-to in nonlinear dynamics as *homoclinic connection*, a method that is suitable for predicting its occurrence is the Melnikov's method (see for example Guckenheimer and Holmes [2002]). The Melnikov's method key advantage in the present context is that, it produces a very simple formula that is useful when one assesses a ship's tendency for broaching-to. On the other hand, accruing from the fact that the method treats the studied system as comprised by a Hamiltonian 'unperturbed' sub-system plus a small perturbation, this method is mathematically valid if the terms that play the role of damping can be reasonably assumed as"small". This applies for the terms that represent the external forcing as well. In order to overcome the constraint set by the assumption of small damping and small forcing, the extended Melnikov's method is applied in this chapter.

Real ship data has been used in order to evaluate the extended Melnikov's method against alternative predictions of the locus of global surf-riding as one of the key parameters, the Froude number or the wave height, are varied. The results obtained were very close to the numerical values and consistently closer than the results of its "standard" version; at the expense however of not been able to produce a handy "closed-form" expression, like the standard Melnikov's method does.

4.1 Mathematical model

A rudimentary mathematical model for the nonlinear surging of a ship in following seas can be derived using Newton's second law (e.g. Kan [1990]; Spyrou [2006]):

$$(m - X_{\dot{u}})\dot{u} + [R(u) - T(u, n)] + X_w = 0. \tag{4.1}$$

in which, m and $X_{\dot{u}}$ are the mass and added mass of surge, respectively. R is the resistance force in surge direction, T is the propeller thrust and X_w is the wave force in surge direction. For a harmonic incident wave, the Froude-Krylov force in surge can be calculated as

$$X_w \approx f \sin(kx). \tag{4.2}$$

where x is the distance from the center of gravity of the ship to a reference wave trough (therefore the axes origin is moving with the wave). k is the wave number and f is a constant for a given harmonic wave.

Resistance could be expressed as a polynomial of velocity u:

$$R(u) = r_1 u + r_2 u^2 + r_3 u^3. \tag{4.3}$$

where $r_i, i = 1, 2, 3$ are coefficients. The propeller thrust is expressed in terms of thrust coefficient K_T in Eq. (4.4).

$$T(u; n) = (1 - t_p)\rho n^2 D_p^4 K_T(u; n). \tag{4.4}$$

where t_p is the thrust-deduction coefficient, ρ is water density, n is propeller rate and D_p is the diameter of propeller. K_T can be written as simple polynomial of speed of advance $J(u; n)$

$$K_T = \kappa_0 + \kappa_1 J(u; n) + \kappa_2 J^2(u; n). \tag{4.5}$$

in which

$$J(u;n) = \frac{u(1-w_p)}{nD_p}. \tag{4.6}$$

where $\kappa_i, i = 0, 1, 2$ are coefficients and w_p is wake fraction. Substituting Eq. (4.6) and Eq. (4.5) into Eq. (4.4), we have

$$T(u;n) = \tau_2 u^2 + \tau_1 un + \tau_0 n^2. \tag{4.7}$$

where

$$\tau_2 = \kappa_2(1-t_p)(1-w_p)^2\rho D_p^2,\ \tau_1 = \kappa_1(1-t_p)(1-w_p)\rho D_p^3,\ \tau_0 = \kappa_0(1-t_p)\rho D_p^4.$$

Since x is the distance from a wave trough, $\dot{x}$ is the relative velocity of ship to the wave celerity, *i.e.* $\dot{x} = u - c$. Substituting Eq. (4.2) - Eq. (4.7) into Eq. (4.1) and expressing everything in x:

$$\begin{aligned}(m - X_{\dot{u}})\ddot{x} &+ \{\underbrace{[3r_3c^2 + 2(r_2 - \tau_2)c + r_1]}_{A_1} - \tau_1 n\}\dot{x} \\ &+ \underbrace{[3r_3c + (r_2 - \tau_2)]}_{A_2}\dot{x}^2 + \underbrace{r_3}_{A_3}\dot{x}^3 + f\sin(kx) \\ &= \underbrace{(\tau_2c^2 + \tau_1cn + \tau_0n^2)}_{T} - \underbrace{(r_1c + r_2c^2 + r_3c^3)}_{R}.\end{aligned} \tag{4.8}$$

This equation can be re-arranged into the form

$$y'' + p_1y' + p_2y'^2 + p_3y'^3 + \sin y = \frac{r}{q} + by'. \tag{4.9}$$

in which

$$y = kx, \quad \tau = \sqrt{q}t, \quad q = \frac{fk}{(m - X_{\dot{u}})}, \quad r = \frac{[T - R]k}{(m - X_{\dot{u}})}, \quad b = \frac{\tau_1 n}{\sqrt{fk(m - X_{\dot{u}})}}$$
$$p_1 = \frac{A_1}{\sqrt{fk(m - X_{\dot{u}})}}, \quad p_2 = \frac{A_2}{k(m - X_{\dot{u}})}, \quad p_3 = \frac{A_3 f^{1/2}}{k^{3/2}(m - X_{\dot{u}})^{3/2}}.$$

The prime denotes derivative with respect to the introduced scaled time τ. For a given ship under given wave condition, $p_i, i = 1, 2, 3$ are constants. If the wave environment is fixed, then the only unknown parameter in Eq. (4.9) is the propeller rates n, appearing in the expressions that provide r and b. This is the reason why we opted to keep by' separated from $p_1 y'$ in Eq. (4.9). The main purpose of current work is to find out whether the extended Melnikov's method is suitable for determining directly the propeller rates (and the corresponding nominal Froude number), which results in global surf-riding.

4.2 Formulation of Melnikov's function

For the surf-riding problem, the occurrence of homoclinic orbit corresponds to the break of periodic surging and the capture into surf-riding. If the standard Melnikov's method was applied for predicting this event, the unperturbed sub-system should be Hamiltonian with a homoclinic (or heteroclinic) orbit and, damping and forcing terms should be small. Unfortunately, in the surf-riding problem, the damping terms cannot be assumed, in general, to be small. As a matter of fact, it is doubtful whether the standard Melnikov's method can produce results of reasonable accuracy in all cases. Hence, there is scope for trying the extended Melnikov's method discussed here. As shown in Spyrou [2006], the standard Melnikov's method produces the following closed-form prediction formula, relating the unknown

terms r and b (these are functions of the propeller rate):

$$\frac{r}{q} + b\frac{4}{\pi} = -\frac{4}{\pi}p_1 + 2p_2 - \frac{32}{3\pi}p_3 = C \tag{4.10}$$

This formula will be used for comparison against the results obtained by the new method.

In the following, we shall describe two different implementations of the new method:

- Treating the linear damping as large but damping nonlinearities as small.
- Treating both linear and nonlinear damping terms as large.

4.2.1 Treating linear damping as large term

When the linear damping term is treated as large, the unperturbed system of Eq. (4.9) is

$$\begin{aligned} \dot{y}_1 &= f_1 = y_2 \\ \dot{y}_2 &= f_2 = p_1 y_2 + \sin y_1 + \sigma. \end{aligned} \tag{4.11}$$

in which, $y_1 = y$ and $y_2 = y'$. One notes that, an initially unknown constant σ has been added to the unperturbed sub-system in order to enable the formation of the necessary heteroclinic orbit. Then, the perturbation described by Eq. (4.9) should be expressed now as:

$$\begin{aligned} g_1 &= 0 \\ g_2 &= \varepsilon(\frac{b}{\varepsilon}y_2 - \frac{p_2}{\varepsilon}y_2^2 - \frac{p_3}{\varepsilon}y_2^3 + \frac{r}{\varepsilon q} + \frac{\sigma}{\varepsilon}) \end{aligned} \tag{4.12}$$

Following substituting of Eq. (4.11) and (4.12) into Eq. (2.12), the corresponding Melnikov's

function $M(t_0)$ is finally expressed as follows:

$$M(t_0) = \frac{b}{\varepsilon} I_3 - \frac{p_2}{\varepsilon} I_2 - \frac{p_3}{\varepsilon} I_1 + \frac{1}{\varepsilon}(\frac{r}{q} + \sigma) I_4 \tag{4.13}$$

in which

$$\begin{aligned} I_1 &= \int_{-\infty}^{\infty} y_2^4 \exp(p_1 t) dt, \\ I_2 &= \int_{-\infty}^{\infty} y_2^3 \exp(p_1 t) dt, \\ I_3 &= \int_{-\infty}^{\infty} y_2^2 \exp(p_1 t) dt, \\ I_4 &= \int_{-\infty}^{\infty} y_2 \exp(p_1 t) dt. \end{aligned}$$

(y_1, y_2) are the coordinates of the heteroclinic orbits corresponding to Eq. (4.11). According to what was said earlier, the threshold of global surf-riding should be found when the Melnikov's function becomes zero. In this case:

$$\frac{r}{q} + \frac{bI_3}{I_4} = \frac{p_2 I_2 + p_3 I_1}{I_4} - \sigma = C \tag{4.14}$$

Note that it is independent of ε. p_2, p_3 and q are system parameters, and for the ship model used here, these are constants. Alike σ, I_1, I_2, I_3 are essentially constants that can be calculated with above integrations.

Details of obtaining the value of σ can be found in Appendix A.1. The heteroclinic orbit (y_1, y_2) needs to be determined numerically, because analytical solution of Eq. (4.11) seems to be unlikely. For the same reason, numerical integrations should be carried out for I_1, I_2 and I_3. The truly unknown terms are r and b, which are functions of propeller rate n.

Given the wave height, the critical propeller rate that may lead to global surf-riding can be obtained from Eq. (4.14).

4.2.2 Treating linear damping and nonlinear damping as large terms

In Eq. (4.9), one might have assumed all linear and nonlinear damping terms as large, without facing any difficulty in the implementation of the method. However, in the sample ship investigated here for the purpose of demonstrating the method, the cubic damping term was indeed a small number, when the scaled velocity obtained realistic values. Subsequently, in this case only linear and quadratic damping terms needed to be treated as large quantities. When considering both linear and quadratic damping terms as large, the unperturbed subsystem becomes as follows:

$$\begin{aligned} \dot{y}_1 &= f_1 = y_2 \\ \dot{y}_2 &= f_2 = p_1 y_2 + p_2 y_2^2 + \sin y_1 + \sigma. \end{aligned} \tag{4.15}$$

The perturbation terms are

$$\begin{aligned} g_1 &= 0 \\ g_2 &= \varepsilon(\frac{b}{\varepsilon} y_2 - \frac{p_3}{\varepsilon} y_2^3 + \frac{r}{\varepsilon q} + \frac{\sigma}{\varepsilon}). \end{aligned} \tag{4.16}$$

which is a function of unknown propeller rate n.

According to the definition in Eq. (2.12), the Melnikov's function for this system is

$$M(t_0) = -\frac{p_3}{\varepsilon} I_1 + \frac{b}{\varepsilon} I_2 + \frac{1}{\varepsilon}(\frac{r}{q} + \sigma) I_3 \tag{4.17}$$

in which

$$\begin{aligned}
I_1 &= \int_{-\infty}^{\infty} y_2^4 \exp(p_1 t + 2p_2 \int_0^t y_2 ds) dt, \\
&= \int_{-\infty}^{\infty} y_2^4 \exp(p_1 t + 2p_2 y_1) dt, \\
I_2 &= \int_{-\infty}^{\infty} y_2^2 \exp(p_1 t + 2p_2 \int_0^t y_2 ds) dt \\
&= \int_{-\infty}^{\infty} y_2^2 \exp(p_1 t + 2p_2 y_1) dt, \\
I_3 &= \int_{-\infty}^{\infty} y_2 \exp(p_1 t + 2p_2 \int_0^t y_2 ds) dt, \\
&= \int_{-\infty}^{\infty} y_2 \exp(p_1 t + 2p_2 y_1) dt.
\end{aligned}$$

The critical condition is

$$\frac{r}{q} + \frac{bI_2}{I_3} = \frac{p_3 I_1}{I_3} - \sigma = C \tag{4.18}$$

Similarly, q and p_3 are system parameters. For a specific ship and a specific wave, these are constants. I_1, I_2, I_3 and σ are constants too that can be calculated. Details of calculating σ in this case can be found in Appendix A.2. The heteroclinic orbit (y_1, y_2) in Eq. (4.15) is calculated numerically, as well as I_1, I_2 and I_3. Then from Eq. (4.18), the critical propeller rate n that should give rise to global surf-riding can be determined.

4.3 Numerical results

4.3.1 Simulation of transition from periodic surfing to surf-riding

To verify the mathematical model we performed time simulation and recreated the well-known behavior of the transition from periodic surging to surf-riding, on the basis of a well-known ITTC purse-seiner with length $L = 34.5$m that has been studied several times in the past (e.g. Spyrou [1996]). The wave length λ was fixed throughout this study at twice the ship length. Several values of the wave steepness $h = H/\lambda$ (H is the wave height) were investigated. It has been shown in many studies that the Froude-Krylov force in the surge direction is significant, and the diffraction force can be ignored for the surge motion. Therefore, in this study, only the Froude-Krylov force was calculated.

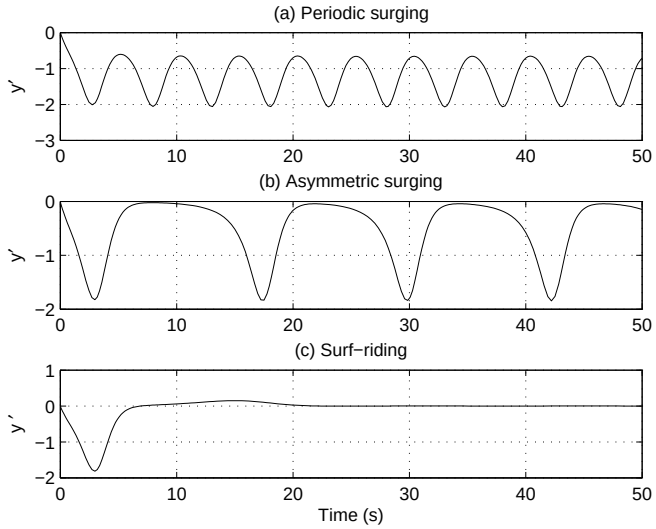

Figure 4.1: Time series of surging velocity at different propeller rates.

In Figure 4.1 is shown a series of simulations for the considered ship, as the propeller rate is increased. The wave steepness was $h = 0.05$. All simulations were started with the ship at wave crest and having zero surge velocity. When the propeller rate n is small, the surge

velocity changes periodically in time (Figure 4.1(a)). Increasing of the propeller rate causes the periodic motion to become strongly asymmetric, as shown in Figure 4.1(b). In such a case, the ship spends, per wave cycle, much more time around the wave crest than around the wave trough. When the propeller rate is greater than some critical value, surf-riding occurs (Figure 4.1(c)).

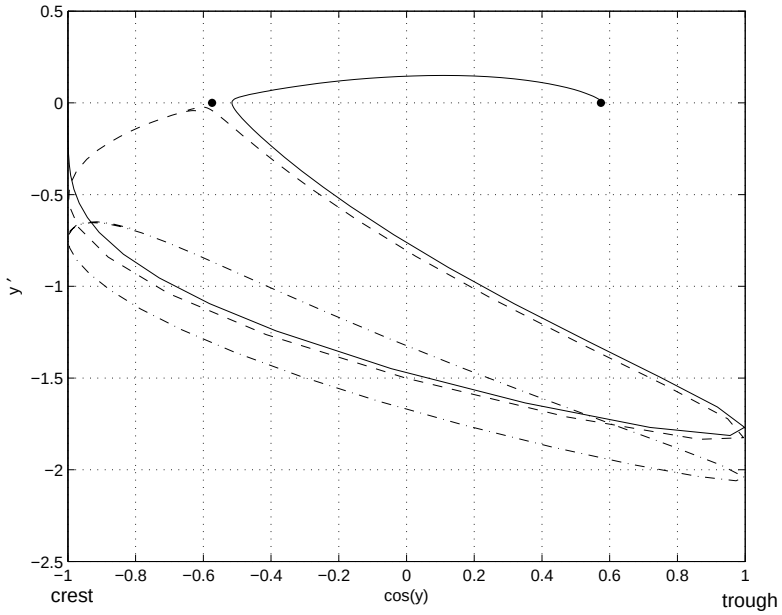

Figure 4.2: Phase plane of the surge motion. Dash-dotted line: periodic motion. Dashed line: asymmetric surging. Solid line: surf-riding.

In Figure 4.2 is shown a phase plane $[\cos(y), y']$ of the surge motion. The dash-dotted line is the periodic motion corresponding to Figure 4.1(a). When the propeller rate increases, the periodic orbits approaches the unstable equilibrium point at the crest, which results in asymmetric periodic motion. This is shown as the dashed line in Figure 4.2. The corresponding time series was already shown in Figure 4.1(b). When the propeller rate n is greater than the critical value, the periodic orbit breaks and is attracted to the stable equilibrium point close to the trough, shown as the solid line in Figure 4.2. This scenario corresponds

to surf-riding, as seen in the time domain Figure 4.1(c).

4.3.2 Treating the linear damping as large

For different linear damping values, the critical values of σ have been calculated. These were plotted versus the linear damping coefficient p_1 in Figure 4.3. The obtained numerical values of σ are compared against those based on the function $-4\tanh p_1/\pi$, which was proposed by Kan [1990]. It should be noted that Kan's model only contains a linear damping term and a constant torque which is a function of speed. He numerically calculated the critical value of the constant torque beyond which the global surf-riding occurs and showed graphically the change of the critical torque with the linear damping. Superposed on his data, in Figure 4.3 are shown the critical values of σ_c obtained by the current method. According to our notation, the relationship between the critical torque and linear damping coefficient can be fitted into the line $\alpha = -4\tanh\beta/\pi$, in which α is the torque and β is linear damping coefficient.

In the model considered here, σ_c is the value that enables the formation of the heteoclinic orbit for the unperturbed system. If the nonlinear damping coefficients p_2 and p_3 are all zero in Eq. (4.14), and if the dependence on propeller rate of the partial linear damping coefficient b can be ignored, our model can be reduced to Kan's model. σ_c corresponds to the critical torque value r/q of surf-riding. Our results agree well with Kan [1990] in this sense.

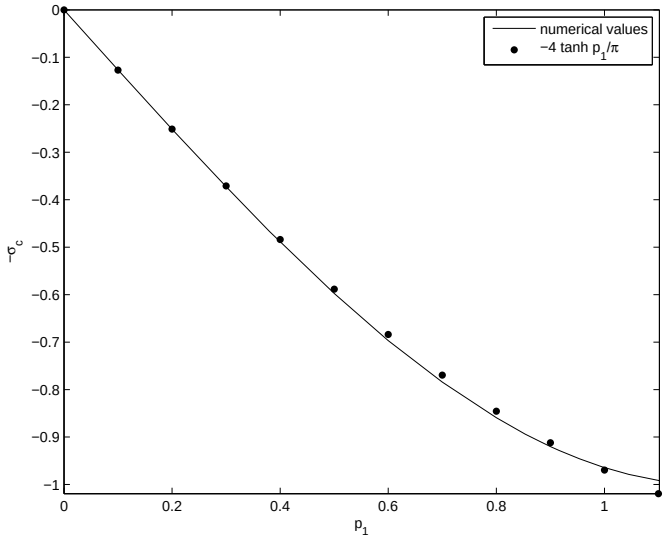

Figure 4.3: The numerical values of σ_c for different values of p_1 compared with empirical formula.

4.3.3 Treating both the linear and nonlinear damping terms as large

Figures 4.4 - 4.6 show σ_c for different linear damping coefficient p_1 and quadratic damping coefficient p_2. From Eq. (4.9), p_2 is not a function of wave force. In fact, for the ship model used in this work, p_2 is a constant. However, in order to show more general relationship on p_2 and σ_c, we picked different values of p_2. Figure 4.4 is the surface of σ_c as a function of p_1 and p_2. Figures 4.5 and Figure 4.6 are cross sections of the surface (p_1, p_2, σ_c). The dashed lines are results from Eq. (4.10) the standard Melnikov's results $-4p_1/\pi + 2p_2$. The dots represent $-4\tanh(p_1 - p_2\pi/2)/\pi$. This formula is inspired by the formula found from the application of the standard Melnikov's method as well as the formula from Kan [1990].

Since the primary drawback of the extended Melnikov's method is it's inability to provide a closed-form formula, we are trying to use this formula as a 'best fit' approximation based on the numerical results. As shown in Figure 4.5(a)-(c), when p_2 is small, this empirical

formula shows strong agreement with numerical results. However, when p_2 is large, as shown in Figure 4.6(a)-(b), the empirical formula is not a suitable replacement for the results from direct calculation of the extend Melnikov's method.

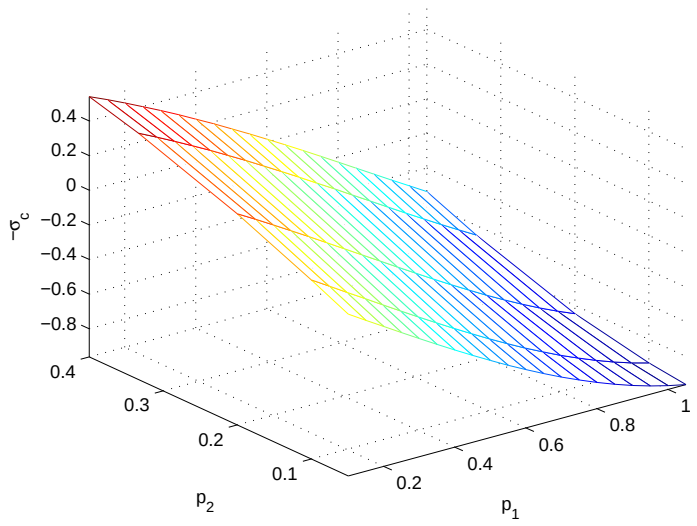

Figure 4.4: Numerical values of σ_c for different values of p_1 and p_2 when treating both linear and quadratic damping terms large.

The nominal Froude numbers for different methods are compared in Figure 4.7. These Froude numbers are calculated using the maximum speeds of the ship in still water under the critical propeller rates. In the numerical simulations, different initial conditions and propeller rates are considered with different wave steepness. According to the simulation, the Froude numbers of the ship on still water are divided into three regions depending on the occurrence of surf-riding. This corresponds to the solid lines in the figure. In region I, below the lower solid line, no surf-riding occurs. This region corresponds to periodic motions. From the dynamics point of view, if the equilibrium points exist, the coordinates should be $(\arcsin(r/q) + n\pi, 0)$. The eigenvalues at these equilibrium points are $\lambda_{1,2} = \frac{-p_1 \pm \sqrt{p_1^2 - 4cos(\arcsin(r/q)+n\pi)}}{2}$. For any positive p_1 and any r/q that make $\arcsin(r/q)$ exist,

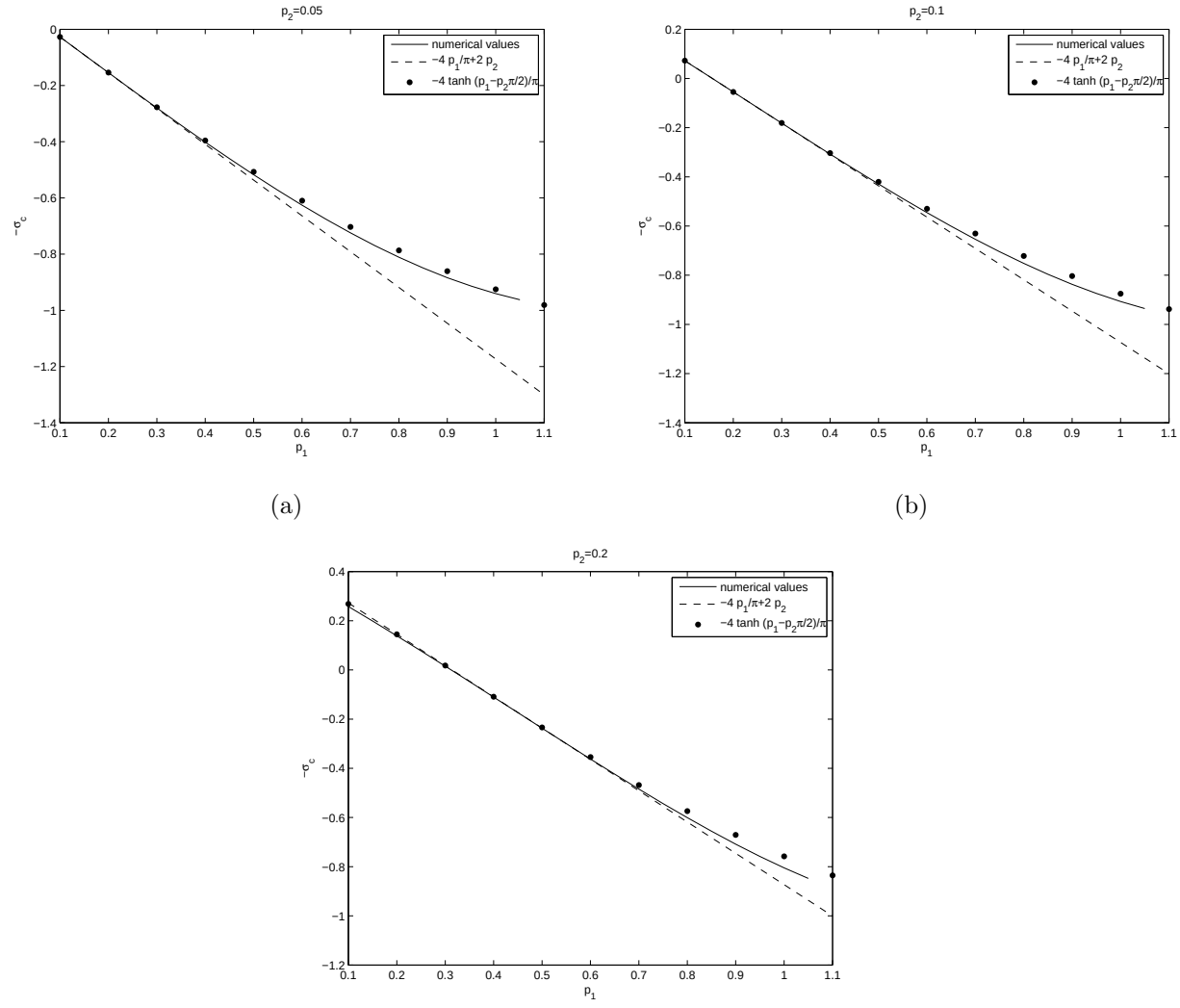

Figure 4.5: Numerical values of σ_c compared with empirical formula.

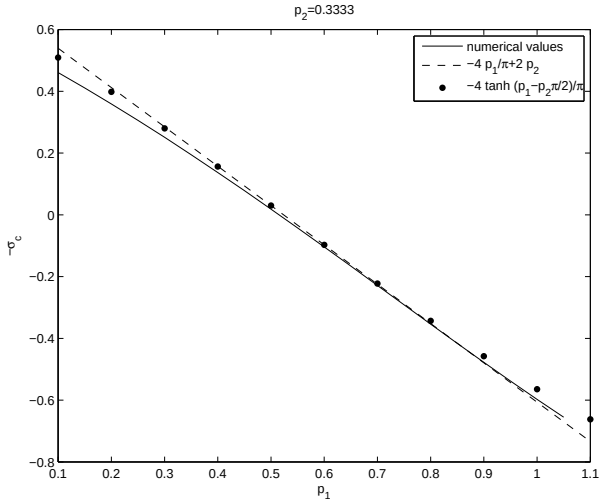

(a)

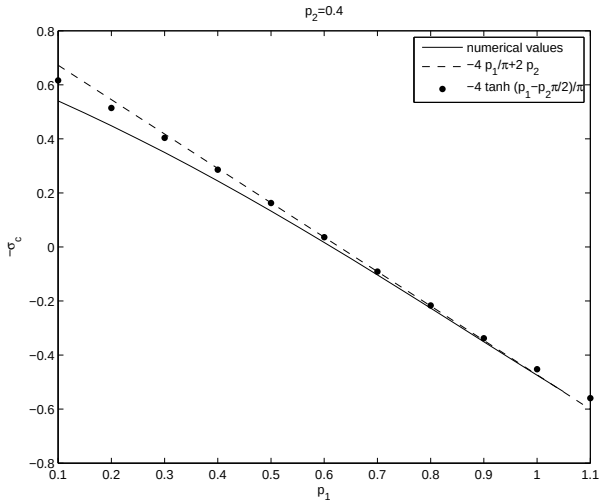

(b)

Figure 4.6: Numerical values of σ_c compared with empirical formula.

at least one eigenvalue at the equilibrium points is negative. This means the existence of stationary solution, *i.e.* surf-riding in this case. Therefore, in order to have all periodic motions, there should be no stable equilibrium points, which means $r/q > 1$ or $r/q < -1$. Since $r < 0$, the condition $r/q < -1$ can be used to calculate the boundary where there are only periodic motions.

In region II, the area between two solid lines, surf-riding occurs at some initial conditions, while other initial conditions remain periodic surging. Region III is the area above the higher solid line. This is the area that all initial conditions result in surf-riding, *i.e.* global surf-riding. The Melnikov's method is actually a method used to predict when this will happen. Results from the extended Melnikov's method which treating linear and quadratic damping terms large and the results from the traditional Melnikov's method from Spyrou [2006] are all plotted in Figure 4.7. These lines are all follow the trends of the line for global surf-riding, but the results from extended Melnikov's method are more accurate.

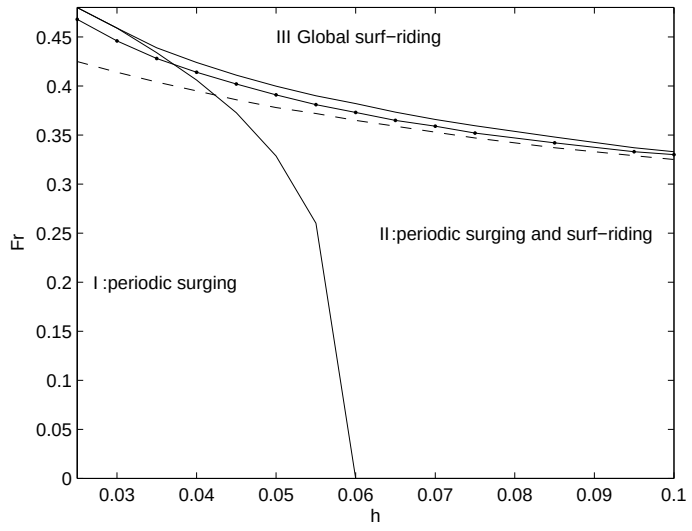

Figure 4.7: Critical Froude's number and wave height. Solid lines: results from numerical simulations. Dashed line: results from standard Melnikov's method. Solid-dotted line: results from extended Melnikov's method treating linear and quadratic damping large.

4.4 Concluding remarks

The extended Melnikov's method has been used in order to predict global surf-riding while overcoming the small damping constraint. This method seems to produce a result with consistent accuracy, however, the elegant simplicity of an analytical formula which one could use as guidance for safe operation is not feasible. In addition, if the linear damping term is larger than some value, it is impossible to find σ_c to yield the homoclinic orbit, which presents a secondary constraint on this approach. The empirical formula $-4\tanh p_1/\pi$ which is provided by Kan is verified using the numerical values of σ_c for treating linear damping term as large. When treating both linear and quadratic damping terms as large, the formula $-4\tanh(p_1 - p_2\pi/2)/\pi$ is a good fitting to the numerical values when p_2 is small. This provides the possibility of a semi-empirical correction of the standard Melnikov's formula in the light of new results. More general formula is needed for the surface of σ_c. Of course, this semi-empircal formula needs to be validated further, by carrying out comparisons based on other ships.

Chapter 5

Melnikov's Method and a Multi-DOF Ship Model

5.1 Introduction

Analytical modeling of full 6-degrees of freedom vessel motions is complex. Most previous work on multi-degree-of-freedom vessel motions either reduced the problems to single-degree-of-freedom problem or used numerical simulations, as reviewed in Chapter 1. Compared to 1DOF problems, relatively little work has been done using analytical methods for multi-DOF ship motion problems. In this chapter, the Melnikov's method has been used to a coupled roll-sway-heave model derived by Chen et al. [1999]. By changing the coordinates and applying the singular perturbation technique (Khalil [1996]), Chen et al. [1999] shows the model can be simplified to a slowly varying system with three variables, in which sway velocity is the slowly varying variable; roll displacement and roll velocity are the fast varying variables. This kind of system can be manageable using the Melnikov's method discussed in Section 2.3. The purpose of this work is to show the possibility of applying the extended

Melnikov's method to multi-degree-of-freedom problems. It is worth to be noted that while the ship roll-sway-heave problem was the motivation, we were led to consider a modified system, the reason being a technical obstacle in the implementation of the method that needs to be theoretically resolved.

5.2 Mathematical model

In this section, the derivation of the mathematical model in Chen et al. [1999] has been summarized. It provides the basis for the work in the next section. In an earth-fixed coordinate system, the equation of motion of the coupled roll-sway-heave can be expressed in Eq. (5.1).

$$\begin{aligned} my_c'' &= Y \\ mz_c'' &= Z \\ I_{44}\phi'' &= K \end{aligned} \tag{5.1}$$

in which, ϕ is roll angle, (y_c, z_c) is the center of gravity. I_{44} is the moment of inertial in roll about the center of gravity. m is the mass of the vessel. K, Y and Z are generalized forces, which contains hydrostatic and hydrodynamic forces as mentioned in Chapter 1. In this model, the vessel is considered to move in beam seas and the wave length is large compared to the beam of the ship. Chen et al. [1999] transformed the model into a wave-fixed coordinate system. In this system, the vessel is viewed as a particle rides on the surface of the wave. The sway motion is now parallel to the local wave surface and the heave motion is perpendicular to the local wave surface.

The hydrostatic forces under this new coordinate system can be expressed as in Eq. (5.2).

$$\begin{aligned} Y_s &= 0 \\ Z_s &= g_e R(z_0, \phi) \\ K_s &= -g_e[m + R(z_0, \phi)]GZ(z_0, \phi) \end{aligned} \tag{5.2}$$

in which, z_0 is heave displacement in the new coordinate system. $g_e R(z_0, \phi)$ is the force in heave direction, and GZ is the righting arm. In this coordinate system, the vessel is viewed as a water particle moving on the wave surface. From linear wave theory, the wave particle is moving in circular path. Therefore, the vessel experiences not only gravity force, but also centrifugal force. This can be denoted by the 'effective gravitational acceleration' g_e in Eq. (5.3) (Chen et al. [1999]).

$$g_e = g - \omega_w^2 a \cos \omega_w t \tag{5.3}$$

where ω_w is the wave frequency; a is the wave amplitude.

The hydrodynamical forces consisting of added mass and damping can be expressed per Chen et al. [1999] in Eq. (5.4).

$$\begin{aligned} Y_{hd} &= -(a_{24}\phi'' + b_{24}\phi' + a_{22}y_0'' + b_{22}y_0' + a_{23}z_0'' + b_{23}z_0') \\ Z_{hd} &= -(a_{34}\phi'' + b_{34}\phi' + a_{32}y_0'' + b_{32}y_0' + a_{33}z_0'' + b_{33}z_0') \\ K_{hd} &= -(a_{44}\phi'' + b_{44}\phi' + b_{44q}\phi'|\phi'| + a_{42}y_0'' + b_{42}y_0' + a_{43}z_0'' + b_{43}z_0') \end{aligned} \tag{5.4}$$

in which y_0 is the sway displacement in new coordinate system. The coefficients a_{ij} are the added mass in i direction due to a unit acceleration in j direction. And b_{ij} are the damping forces in i direction due to a unit velocity in j direction. Here, $2 - sway$, $3 - heave$ and

$4 - roll$. For a vessel with starboard-port side symmetry, $a_{ij} = a_{ji}$ and $b_{ij} = b_{ji}$. Note, for simplicity, this equation is the linearized equation. And the only nonlinear term is the quadratic damping term in roll.

Assuming a constant horizontal wind pressure P_w, the wind forces can be calculated in Eq. (5.5) (Chen et al. [1999]).

$$\begin{aligned} Y_w &= p_2 \cos\varphi \\ Z_w &= p_2 \phi_0 \cos\varphi \\ K_w &= p_1 \cos^2\varphi \end{aligned} \tag{5.5}$$

where p_1 and p_2 are constant coefficients. ϕ_0 is the angle of the wave surface relative to the horizontal plane, which can be expressed as $\phi_0 = \frac{\omega_w^2 a}{g} \sin\omega_w t$. φ is the angle of the center line of the vessel to the vertical plane.

Substituting Eqs. (5.2)-(5.5) into Eq. (5.1), the full roll-heave-sway equation of motion can be obtained, though this system is still too complicated to analyze directly. Chen et al. [1999] did a systematic simplification to reduce the system to a manageable form. First of all, the natural frequency of heave (ω_h) is much larger than the natural frequency in roll (ω_r). This is generally true for typical ships in typical loading conditions (Lewis [1988]). This implies that heave motion will damp much faster than roll and sway motion. Additionally, all terms containing sway displacement y_0 are higher order term. Therefore, the equation of motion

can be reduced to a special perturbation form in Eq. (5.6).

$$\begin{aligned}
\dot{x}_1 &= x_2 \\
\dot{x}_2 &= f_1(x_1, y) + \varepsilon g_a(x_1, x_2, y, z_1, z_2, \tau) \\
\dot{y} &= \varepsilon g_b(x_1, x_2, y, z_1, z_2, \tau) \\
\varepsilon \dot{z}_1 &= z_2 \\
\varepsilon \dot{z}_2 &= f_2(z_1, z_2) + \varepsilon g_c(x_1, x_2, y, z_1, z_2, \tau)
\end{aligned} \tag{5.6}$$

in which $x_1 = \phi$, $x_2 = \dot{\phi}$, $z_1 = z_0/h$ where h is the draft of the ship. y is a transformed coordinate which contains sway velocity and other variables. z_0 is small compared to h. $\dot{(\cdot)}$ is the derivative relative to τ, where $\tau = \omega_r t$.

From Khalil [1996], the singular perturbation theory deals with system in a form of

$$\begin{aligned}
\dot{\zeta} &= f(t, \zeta, \eta, \varepsilon) \\
\varepsilon \dot{\eta} &= g(t, \zeta, \eta, \varepsilon)
\end{aligned} \tag{5.7}$$

in which ε is the ratio of the slow dynamics ζ to the fast dynamics η. The steady state of this system is $g(t, \zeta, \eta, 0) = 0$. By solving this equation, the fast dynamics can be represented by the slow dynamics as $\eta = \varsigma(t, \zeta)$. Then the slow dynamics can be expressed as

$$\dot{\zeta} = f(t, \zeta, \varsigma(t, \zeta), 0) \tag{5.8}$$

The theory of singular perturbation points out that the dynamics of the system in Eq. (5.7) can be represented by the system in Eq. (5.8).

When applying the singular perturbation theory in to the roll-heave-sway model in Eq. (5.6),

the heave motion is the fast dynamics, while roll and y are slow dynamics. Therefore, z_1 and z_2 can be solved from the steady state equation and plug into the slow dynamics. The model is now reduced to

$$\begin{aligned} \dot{x}_1 &= x_2 \\ \dot{x}_2 &= f_1(x_1, y) + \varepsilon g_1(x_1, x_2, y, \varepsilon, \tau) \\ \dot{y} &= \varepsilon g_2(x_1, x_2, y, \varepsilon, \tau) \end{aligned} \tag{5.9}$$

in which

$$\begin{aligned} f_1(x_1, y) &= -x_1 + k_{13}x_1^3 - \delta_{42}y \\ g_1(x_1, x_2, y, \varepsilon, \tau) &= \sigma_{41}\cos x_1 + \sigma_{42}\cos^2 x_1 - \delta_{44}x_2 - \\ &\quad \delta_{44q}x_2|x_2| - \lambda f_1(x_1, y)\cos\Omega\tau + \gamma_{41}\sin\Omega\tau \\ g_2(x_1, x_2, y, \varepsilon, \tau) &= \sigma_{21}\cos x_1 - \delta_{24}x_2 - \delta_{22}y + \gamma_{21}\sin\Omega\tau \end{aligned}$$

$\Omega = \omega_w/\omega_r$ is the normalized wave frequency. $-x_1 + k_{13}x_1^3$ is the restoring moment in roll. Other coefficients are functions of ship system constants and wind force constant, which are obtained by Chen et al. [1999].

5.3 Melnikov's function

In this research, we are trying to apply the Melnikov's method discussed in Section 2.4 to the slowly varying system in Eq. (5.9) while assuming the damping terms are large. And the results are compared to the results from the standard Melnikov's method of Chen and Shaw [1997] in which the roll damping terms are assumed to be small.

As pointed out in Proposition 1 in Section 2.4, the periodic orbits exits when

$$\frac{1}{2\pi/\Omega}\int_0^{2\pi/\Omega} g_2(\bar{x}_1, \bar{x}_2, \bar{y}, \varepsilon, \tau) = 0 \tag{5.10}$$

where $(\bar{x}_1, \bar{x}_2, \bar{y})$ is the equilibrium points of the unperturbed system. Therefore, the sway equilibrium can be expressed as

$$\bar{y} = \frac{\sigma_{21}}{\delta_{22}} \cos \bar{x}_1 \tag{5.11}$$

In Eq. (5.9), the damping force is approximated using formula $-\delta_{44}x_2 - \delta_{44q}x_2|x_2|$. For the Melnikov's method in slowly varying system, the unperturbed system should be kept as a homoclinic orbit (Wiggins [1988]). If the linear damping term is assumed to be large, then in the unperturbed sub-system, the center will become a sink, which makes it impossible to have a homoclinic orbit. In this research, we assume the damping is in the form of Eq. (5.12).

$$B(x_2) = ax_2 + bx_2^2 + cx_2^3 \tag{5.12}$$

where a, b and c are coefficients. Although it is physically unrealistic to have quadratic damping term in roll damping, we used it here to see the possibility of using the extended Melnikov's method to multi-DOF problems. The quadratic damping term is assumed to be large in this research. The unperturbed sub-system is now

$$\begin{aligned} \dot{x}_1 &= x_2 \\ \dot{x}_2 &= -x_1 + k_{13}x_1^3 - \frac{\delta_{42}\sigma_{21}}{\delta_{22}} \cos \bar{x}_1 - bx_2^2 + \sigma \end{aligned} \tag{5.13}$$

And in order to have a homoclinic orbit, the constant is set as $\sigma = \frac{\delta_{42}\sigma_{21}}{\delta_{22}} \cos \bar{x}_1$. Thus, the

unperturbed sub-system has reduced to the form of

$$\begin{aligned} \dot{x}_1 &= x_2 \\ \dot{x}_2 &= -x_1 + k_{13}x_1^3 - bx_2^2 \end{aligned} \tag{5.14}$$

This system contains a homoclinic orbit starting from a saddle and connecting to itself as shown in Figure 5.3.

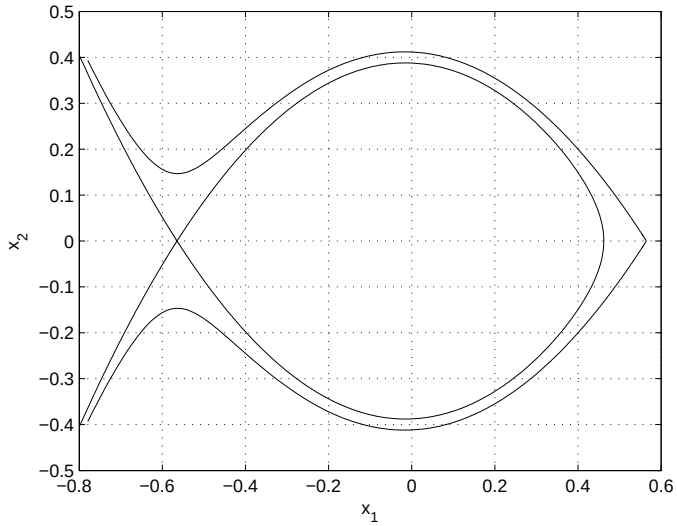

Figure 5.1: Homoclinic orbit for the unperturbed sub-system.

The perturbation terms are now

$$\begin{aligned} g_1(x_1, x_2, y, \varepsilon, \tau) &= \sigma_{41}\cos x_1 + \sigma_{42}\cos^2 x_1 - ax_2 - \\ &\quad cx_2^3 - \lambda f_1(x_1, \bar{y})\cos\Omega\tau + \gamma_{41}\sin\Omega\tau - \sigma \\ g_2(x_1, x_2, y, \varepsilon, \tau) &= \sigma_{21}\cos x_1 - \delta_{24}x_2 - \delta_{22}y + \gamma_{21}\sin\Omega\tau \end{aligned} \tag{5.15}$$

From Eq. (2.28), the Melnikov's function for this system is

$$M(t_0) = \int_{-\infty}^{\infty} x_2 g_1(x_1, x_2, \bar{y}, \tau + t_0) \left\{ \exp\left[\int_0^t 2b x_2 ds \right] \right\} dt - \delta_{42} \int_{-\infty}^{\infty} x_2 \left\{ \int_0^t g_2(x_1, x_2, \bar{y}, s + t_0) ds \right\} \left\{ \exp\left[\int_0^t 2b x_2 ds \right] \right\} dt \quad (5.16)$$

in which (x_1, x_2) is the coordinates of the homoclinic orbits in Eq. (5.14). And $\exp[\int_0^t 2b x_2 ds] = \exp[2b(x_1 - \bar{x}_1)]$. The integration in Eq. (5.16) can be numerically performed without any difficulty.

5.4 Numerical results

The data from the twice capsized fishing boat *Patti-B* is used here for numerical investigation. This is the ship model used in Chapter 3. But due to the different selection of the coordinate systems, some coefficients are different from Chapter 3. Chen et al. [1999] has obtained some hydrostatic and hydrodynamic coefficients for *Patti-B* at $\omega_w = 0.6$. Some of the values of the coefficients used in this research are shown in Table 5.1. Other coefficients are either functions of wave amplitude or wind force constants. In this research, the wind forces are fixed and wave amplitudes are varied.

Table 5.1: Some coefficients for $Patti - B$ from Chen et al. [1999]

parameter	value
k_{13}	3.1355
δ_{42}	-0.0024
$\varepsilon\delta_{22}$	0.0308
Ω	1.0055

From Eq. (5.14), the equilibrium points for the unperturbed sub-system are $(\pm 0.5647, 0)$ and $(0, 0)$. This corresponds to two different values of $\bar{y}$. And as mentioned before, the

quadratic damping term is an artificially created term. In this research, it is set to $b = 0.1$.

5.4.1 Case 1: the equilibrium position $\bar{x}_1 = \pm 0.5647$

In this case, $\bar{y} = 5.0793$ and $\sigma = -0.0124$. The numerical integration of Eq. (5.16) is performed for different values of wave amplitude a. The Melnikov's function is a function of t_0, as shown in Figure 5.2, in which t_0 is the Poincaré section. In Figure 5.2(a), the Melnikov's function is negative, which means the stable and unstable manifolds do not intersect. In Figure 5.2(b), the Melnikov's function touches the zero axis. This is when the stable and unstable manifolds begin to intersect. And in Figure 5.2(c), part of the Melnikov's function is positive, which indicates the manifolds intersect transversely. Therefore, whether or not the maximum value of Melnikov's function crosses the zero line can be used as an indication of transverse intersection between stable and unstable manifolds.

The maximum value of the Melnikov's function for different wave amplitudes is plotted in Figure 5.3. The point where the maximum Melnikov's function is zero corresponds to the critical wave amplitude. The results from standard Melnikov's function per Chen et al. [1999] are also plotted in this figure for comparison. As can be seen, and is to be expected in the figure the critical wave amplitude predicted by the extended Melnikov's method is larger than that from the standard Melnikov's method.

5.4.2 Case 2: the equilibrium position $\bar{x}_1 = 0$

In this case, $\bar{y} = 6.0129$ and $\sigma = -0.0024$. The maximum values of Melnikov's function are plotted in Figure 5.4 for both standard and extended Melnikov's methods. Similar to Figure 5.3, the critical wave amplitude predicted by the extended Melnikov's function is larger than that from the standard Melnikov's method.

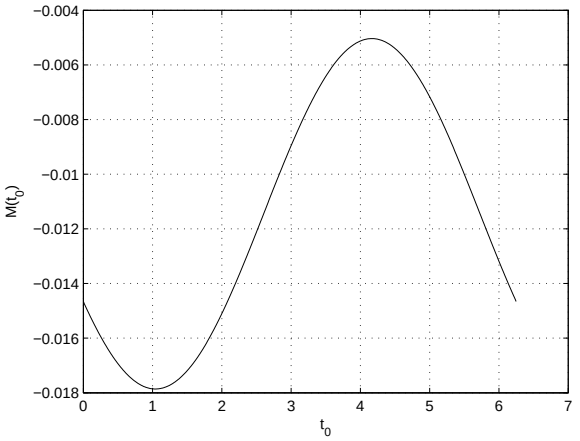

(a) a=0.2

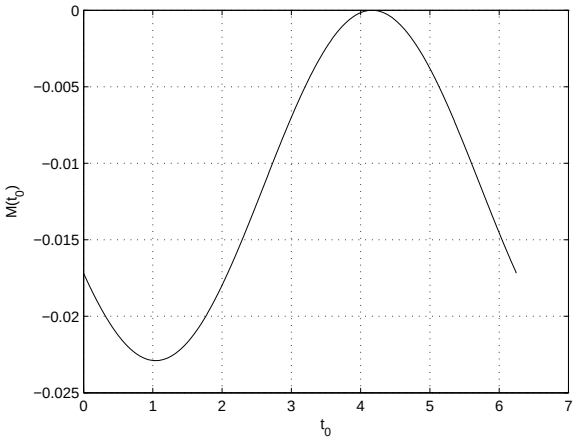

(b) a=0.3571

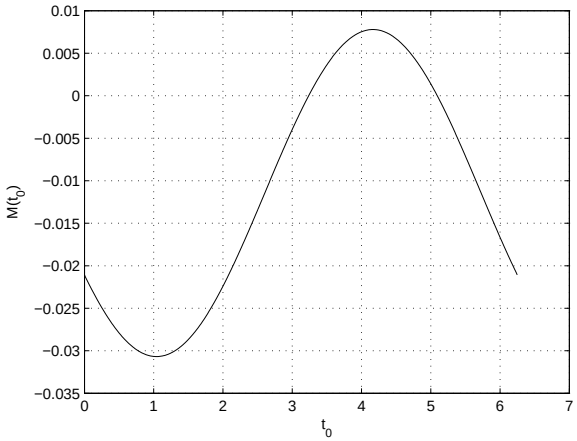

(c) a=0.6

Figure 5.2: The Melnikov's function for different values of wave amplitude.

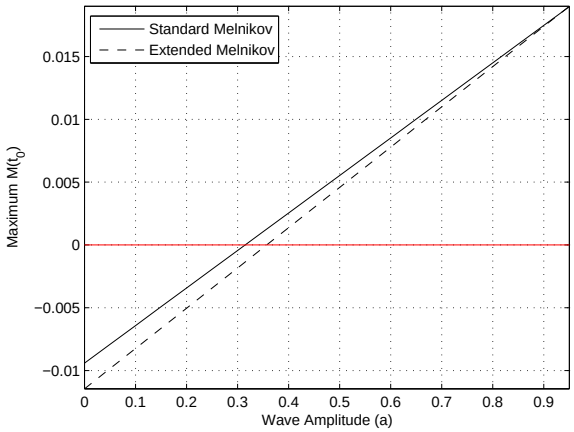

Figure 5.3: The maximum values of Melnikov's function for different values of wave amplitude.

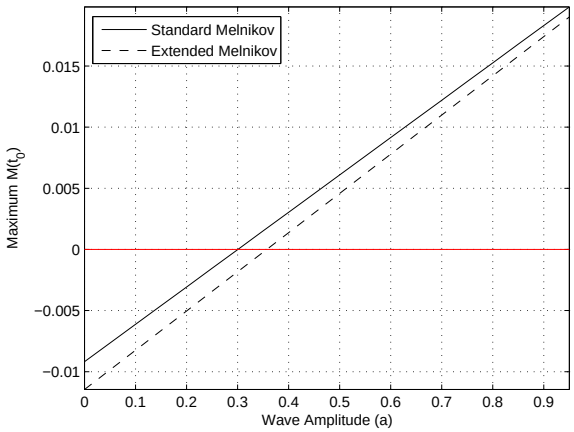

Figure 5.4: The maximum values of Melnikov's function for different values of wave amplitude.

5.5 Some remarks

In this chapter, a three-degree-of-freedom roll-heave-sway model that has been reduced by Chen *et al.* to a slowly varying system through changing coordinate system and using singular perturbation method. The final system contains roll displacement and roll velocity as the fast dynamics and a slow dynamics. The extended Melnikov's method has been applied to this system. In order to obtain a homoclinic orbit in the unperturbed sub-system, the quadratic damping term is treated as large. Although it is not physically reasonable to have the quadratic damping term in roll damping, it is used here just to demonstrate the validity of the method. A constant σ is added to eliminate the constant term in the unperturbed sub-system brought in by the sway displacement. Therefore, different from previous chapters, the calculation of σ is straightforward. The work in this chapter is just the first step of applying the extended Melnikov's method to a special form of multi-degree-of-freedom dynamical systems. But it provides the possibility of applying the method to other multi-degree-of-freedom systems.

Chapter 6

The Method of Manufactured Solutions Applied to Chaotic Systems[1]

6.1 Introduction

As mentioned in Chapter 1, method of manufactured solutions (MMS) is normally used as code verification in computational fluid dynamics or computational solid mechanics. This research applied the method of manufactured solutions in a non-traditional way to the investigation and understanding of simulations of chaotic systems.

The basic idea of MMS is as following:

- Choose an analytical manufactured solution.
- Analytically calculate what prescribed 'source' function results in the chosen solution

[1]This chapter has in large part been accepted for publication with minor revisions as Wu et al. [2009a].

correctly solving the mathematical model.

- Implement said 'source' function into the numerical algorithm.
- Compare the exact solution to that calculated numerically.

The solution should be general enough that every term in the original equation can be exercised. The manufactured solution should also have a significant number of non-trivial derivatives. This means that if the equation is second-order in time, the manufactured solution should be at least twice differentiable in time, meanwhile, the solution derivatives should be bounded in order to ensure the solution is not a strongly varying function. More guidance about choosing proper manufactured solutions can be found in Knupp and Salari [2002].

6.2 Classic chaotic models

The Lorenz system is a heavily studied chaotic system. The governing equation for the Lorenz system is

$$\begin{aligned} \dot{x} &= \sigma(y - x) \\ \dot{y} &= x(R - z) - y \\ \dot{z} &= xy - bz \end{aligned} \tag{6.1}$$

For simplicity, the following sinusoidal functions are used as the manufactured solution to the Lorenz system.

$$\begin{aligned} X &= \cos(t) + c_1 \\ Y &= \sin(t) + c_2 \\ Z &= \sin(t) + c_3 \end{aligned} \tag{6.2}$$

where c_1, c_2 and c_3 are constants. Different initial conditions for position can be obtained by varying the constant terms. Therefore, the requisite source terms Q_1, Q_2 and Q_3 can be calculated as below.

$$\begin{aligned} Q_1 &= -\sin(t) - \sigma(Y - X) \\ Q_2 &= \cos(t) - X(R - Z) + Y \\ Q_3 &= \cos(t) - XY + bZ \end{aligned} \tag{6.3}$$

Thus, if we integrate Eq.(6.4), which include the source terms Qs, then we will have X, Y, and Z from Eq.(6.2) as exact, analytical solutions.

$$\begin{aligned} \dot{x} &= \sigma(y - x) + Q_1 \\ \dot{y} &= x(R - z) - y + Q_2 \\ \dot{z} &= xy - bz + Q_3 \end{aligned} \tag{6.4}$$

In this problem, the parameters are set to be $\sigma = 16.0$, $R = 40.0$, and $b = 4.0$. Under these parameters, the Lorenz equations possess chaotic behavior. Using these parameters

and the manufactured solutions, a 3D grid of $20 \times 20 \times 20$ initial conditions are used for position (x, y, z) to calculate solutions and compared with manufactured solution, as shown in Figures 6.1(a)-6.1(c). Figures 6.1(a)-6.1(c) are the results of using numerical integrator package DLSODA (Hindmarsh [2006]). This package solves first order differential equations with initial conditions. It uses Adams methods (predictor-corrector) for non-stiff problems and Backward Differentiation Formula (BDF) methods for stiff problems. It uses the explicit method to generate the initial guess (predictor) and the implicit method corrects the initial guess until it reaches a reasonable solution as explained by Radhakrishnan and Hindmarsh [1993].

Figures 6.1(a)-6.1(b) are the results of simulating each point until either a manufactured solution discrepancy or $t_{max} = 100s$. The discrepancy is defined as occuring when the absolute difference of the numerical solution and the manufactured solution is more than $1.0e-3$ [2]. The numerical results are compared with manufactured solution every $dt = 0.01s$. Figure 6.1(a) uses stringent error tolerances, and Figure 6.1(b) uses loose error tolerances. In Figure 6.1(c), Figure 6.1(a) is treated as a benchmark to which Figure 6.1(b) is compared. The comparison is the agreement/disagreement with the manufactured solution between the two figures. Of the 8,000 data points, 136 points disagreed. All these points indicated agreement with manufactured solution in Figure 6.1(a), and disagreement with manufactured solution in Figure 6.1(b).

In DLSODA package, the local truncation error d_n is estimated for each step. For easy control of the local truncation error, an error weigh vector EWT_n is calculated using Eq.(6.5).

[2] 1.0e-4 has also been tried for Lorenz and Rossler systems. When using tight error tolerances, the results are the same as using $1.0e-3$ for the Rossler system. While for the Lorenz system, there are a couple of points disagreed between these two values. In this work, for simplicity, $1.0e-3$ is used for both systems.

$$EWT_{i,n} = RTOL_i|Y_{i,n-1}| + ATOL_i \tag{6.5}$$

n represents n^{th} step. $Y_{i,n-1}$ is the numerical solution of i^{th} component at step $n-1$. $RTOL_i$ and $ATOL_i$ are local relative and absolute error tolerances. They are input parameters provided by the user. And they are be either scalar or vector. A solution Y_n is accepted if Eq.(6.6) is satisfied.

$$\|d_n\| = \sqrt{\frac{1}{N}\sum_{i=1}^{N}\left(\frac{d_{i,n}}{EWT_{i,n}}\right)^2} \leq 1 \tag{6.6}$$

The package also periodically changes the step size and/or method order to minimize computational time and to satisfy error tolerances. when the error tolerances are relatively loose, the time steps and error weights are larger and easier to be satisfied. The calculation takes much less time, but numerical integration errors will be larger. When the error tolerances are relatively stringent (tight), the time steps and error weights are smaller, and in order to satisfy the error weights, the time steps may be reduced several times. This calculation takes much more time, but with much less numerical errors. More details about the error estimation and control of this package can be found in Radhakrishnan and Hindmarsh [1993].

In order to show how the different error definitions will influence the numerical results, three different definitions of agreement with the manufactured solutions have been used, which are mathematically shown in Eq. (6.7).

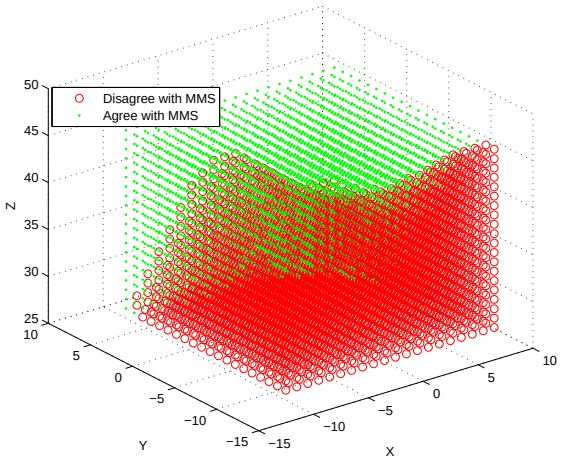

(a)

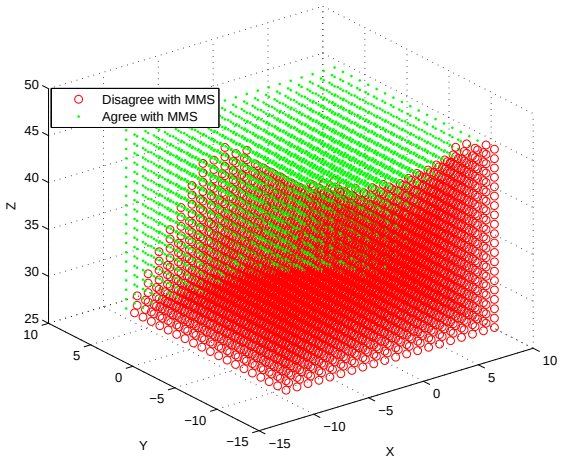

(b)

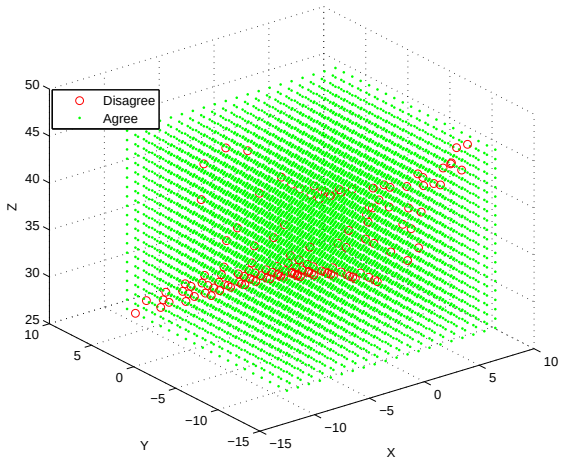

(c)

Figure 6.1: Direct comparison between manufactured solution and numerical simulation results using DLSODA. Figure 6.1(a) is given with relative and absolute error tolerances of 1.0e-12 and 1.0e-16 respectively. Figure 6.1(b) is simulated using relative error tolerance 1.0e-6 and absolute error tolerance 1.0e-8. Figure 6.1(c) compares Figures 6.1(a) and 6.1(b) for MMS agreement.

$$\begin{aligned} L_\infty &= max(|e_i|) \\ L_1 &= \frac{\sum |e_i|}{N} \\ L_2 &= \sqrt{\frac{\sum (e_i^2)}{N}} \end{aligned} \tag{6.7}$$

in which e_i is the local difference between the numerical solution and the manufactured solution. In this work, e_i is treated as scalar. N is the total number of steps taken. Figures 6.2(a)-6.2(d) are generated using the error definitions in Eq. (6.7). Figure 6.2(a) was generated with tight error tolerances and used L_∞ to check the agreement. If L_∞ is less than $1.0e-3$, the numerical solution is said to agree with the manufactured solution. Figure 6.2(b) compares Figures 6.1(a) and 6.2(a) by setting Figure 6.1(a) as benchmark. Direct comparison of agreement/disagreement with manufactured solution was carried out. Figure 6.2(c) was generated using L_2. Figure 6.2(d) compares Figures 6.1(a) and 6.2(c). Of the 8,000 points, 27 disagreed and are all labeled as agreeing with manufactured solution by using L_2. Similarly, Figure 6.2(e) was generated by setting the agreement condition as L_1 is less than $1.0e-3$. Figure 6.2(f) compares Figures 6.1(a) and 6.2(e). Of the 8,000 points, 45 disagreed. All these points are indicated by using L_1 as agreeing with manufactured solution. This means that L_1 provides a least stringent condition for checking for agreement than L_∞ (L_∞ is the same as checking for agreement at every time step) and L_2. In the simulation carried out in this research, the most stringent condition L_∞ is used as the criterion.

By analogy with control theory, the MMS can be interpreted as adding a control (*i.e.* source) term to the original system and in order to force the system to achieve some goal dynamics (*i.e.* the manufactured solution). Control of this form is called entrainment and was studied by Hübler and Lüscher [1989] and Jackson [1991a,b]. The region where system is

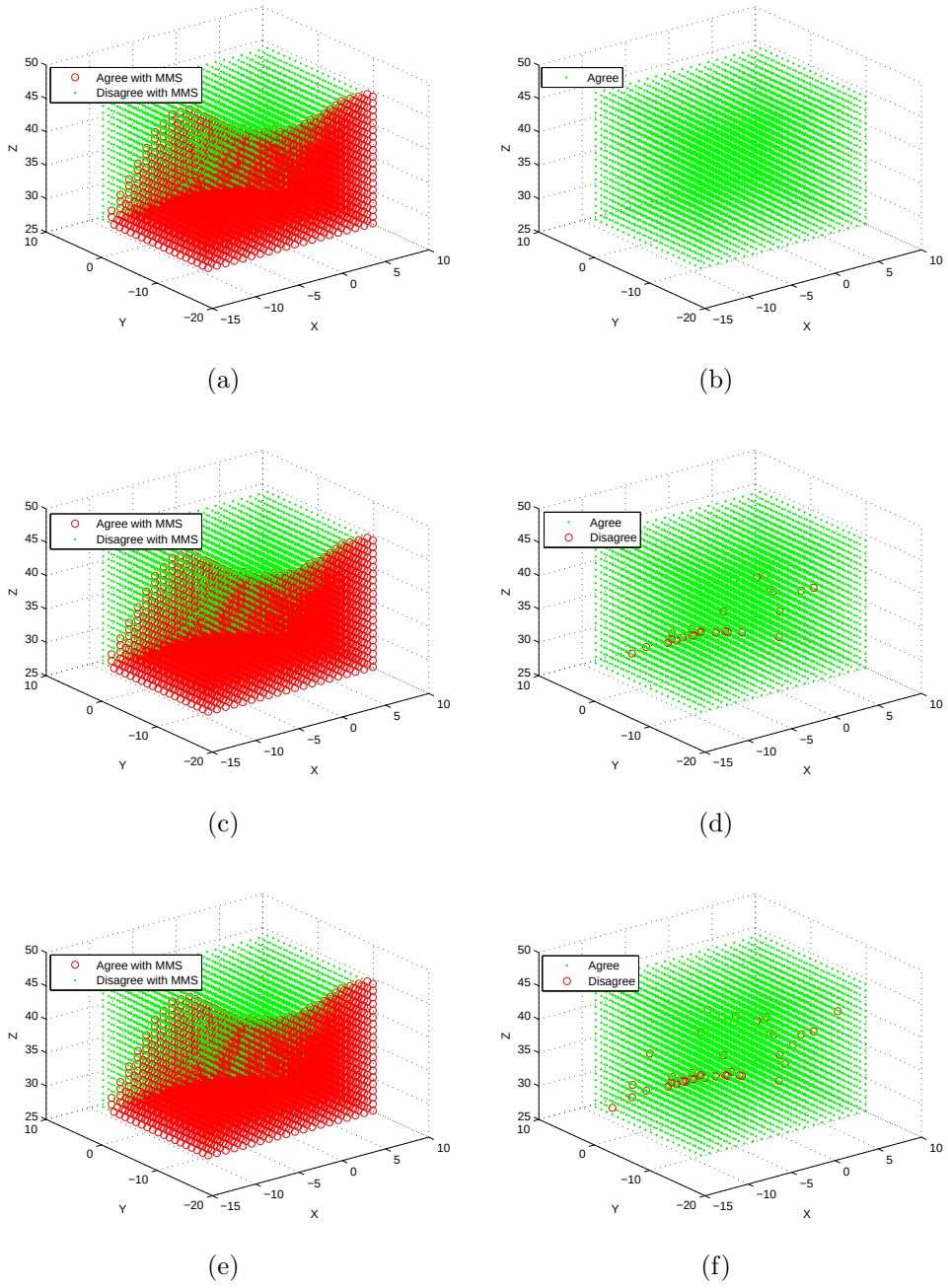

(a) (b)

(c) (d)

(e) (f)

Figure 6.2: Comparison between manufactured solution and numerical simulation results using DLSODA for different agreement definitions. Figures 6.2(a), 6.2(e) and 6.2(c) are all generated with relative and absolute error tolerances of 1.0e-12 and 1.0e-16 respectively. Figure 6.2(a) is generated using L_∞ criterion. Figure 6.2(b) compares Figures 6.1(a) and 6.2(a) for MMS agreement. Figure 6.2(c) is generated using L_2. Figure 6.2(d) compares Figures 6.1(a) and 6.2(c) for MMS agreement. Figure 6.2(e) is generated using L_1. Figure 6.2(f) compares Figures 6.1(a) and 6.2(e) for MMS agreement.

entrained to goal dynamics is called basin of entrainment (BE). Entrainment is possible only if the Lyapunov exponents associated with the goal dynamics are negative (Jackson [1991b]). Therefore, the determination of this basin is challenging, especially for high dimensional systems. As an approximation, part of this basin can be estimated with the help of 'convergent region'. For dynamical systems that contain attractor sets, there is a so-called 'convergent region'. This region is defined as set of data points at which the real parts of the eigenvalues of the Jacobian matrix of the system of first order ordinary differential equations are negative. Therefore, in this region, all nearby orbits converge along the eigenvectors. It is proven by Jackson [1991a] that having the goal dynamics (manufactured solution) entirely contained in the convergent region is the sufficient but not necessary condition for entrainment. This is expressed mathematically for the Lorenz system in Eq. (6.8)(Jackson [1991b]).

$$
\begin{aligned}
&b(z - R + 1) + x(x + y) > 0; \\
&(1 + \sigma)(z - R + 1) + (1 + b)x^2 - \sigma xy + b(1 + \sigma)(1 + \sigma + b) > 0.
\end{aligned} \tag{6.8}
$$

The boundary that satisfies Eq. (6.8) is shown in Figure 6.3(a). The region above the surface is the convergent region. Figure 6.3(b) is created by adding the convergent boundary to Figure 6.1(a). Every point in this figure corresponds to a manufactured solution, *i.e.* different initial condition. Given the form of Eq. (6.2), the values of the manufactured solutions do not oscillate in a large range during the whole time span. For the points far above the boundary, the entire manufactured solutions are within the convergent region. Therefore, the data points far above the boundary all agree with manufactured solutions (entrainment). These are shown both in stringent tolerance case (Figure 6.3(b)) and loose tolerance case (Figure 6.3(c)). Figure 6.3(d) gives the points that showed disagreement from

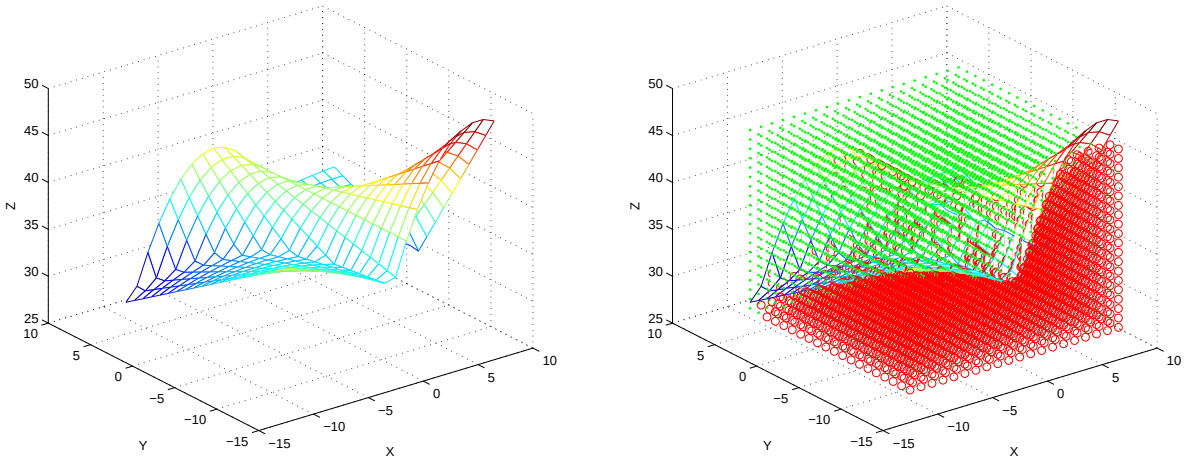

(a) (b)

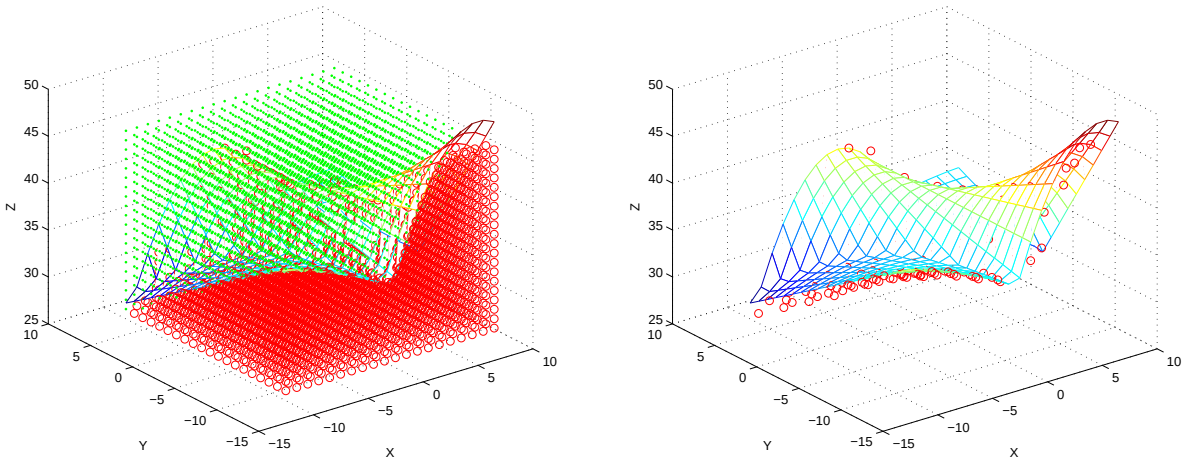

(c) (d)

Figure 6.3: Convergent region of Lorenz oscillator. Figure 6.3(a) is the boundary of convergent region. Above the surface, Eq. (6.8) is satisfied. Figures 6.3(b) and 6.3(c) are the same as Figures 6.1(a) and 6.1(b) except adding the boundary of convergent regions. Figure 6.3(d) compares Figures 6.3(b) and 6.3(c) for MMS agreement.

Figure 6.1(c) with convergent boundary as shown. The disagreed points between stringent and loose tolerances are all close to the boundary. The manufactured solution of these points may enter or exit the convergent region during the time span; thus, the system may or may not entrained to the goal dynamics. Further investigation is needed for these points. As shown in Figures 6.3(b) and 6.3(c), the points far below the boundary are those do not agree with manufactured solutions.

Similar to the Lorenz system, the Rössler system also has chaotic behavior. The equations of motion for the Rössler system are

$$\begin{aligned} \dot{x} &= -(y+z) \\ \dot{y} &= x + ay \\ \dot{z} &= b + z(x-c) \end{aligned} \tag{6.9}$$

One can assume the manufactures solutions in the form below.

$$\begin{aligned} X &= \cos(t) + c_1 \\ Y &= \cos(t) + c_2 \\ Z &= \cos(t) + c_3 \end{aligned} \tag{6.10}$$

where $c_i, i = 1, 2, 3$ are constants. Following the same procedure of the Lorenz system, this system is simulated with $a = 0.2$, $b = 0.2$, and $c = 5.7$, under which the system has chaotic behavior.

It is easy to show that the boundary of the convergent region of Rössler attractor is simply

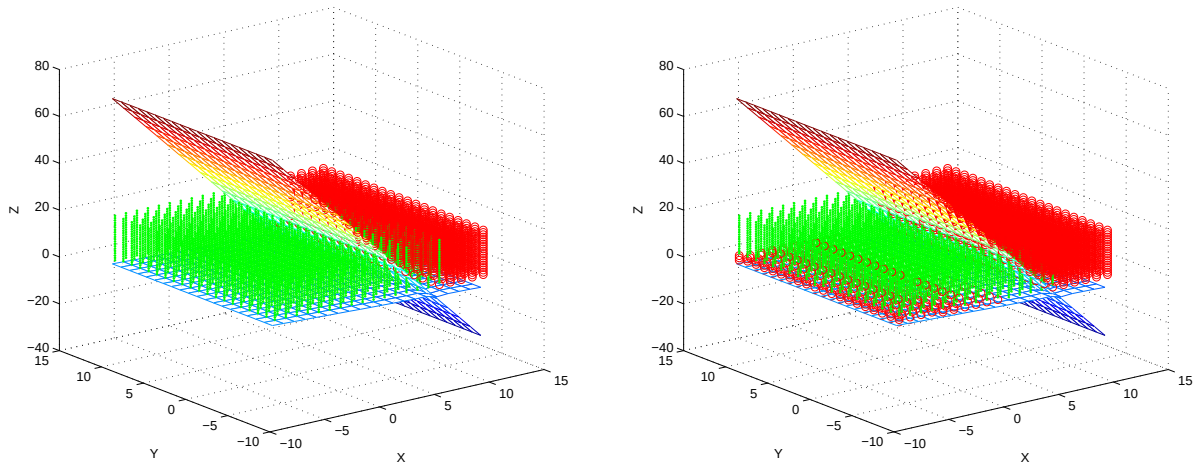

(a) (b)

Figure 6.4: Convergent region of Rössler oscillator and comparison between numerical results and manufactured solutions. Figure 6.4(a) is integrated using DLSODA with relative error tolerance 1.0e-15 and absolute error tolerance 1.0e-18. Figure 6.4(b) is simulated using DLSODA with relative and absolute error tolerances 1.0e-6 and 1.0e-8, respectively. In both figures, green dots denote agree with manufactured solutions, and red circles denote disagree with manufactured solutions.

two planes and is shown in Figure 6.4. The volume between the two surfaces is the convergent region. When using stringent error tolerances, as shown in Figure 6.4(a), all the data points within the convergent region agree with the manufactured solutions (entrained). And all the points that disagree with manufactured solutions are outside of convergent region. As stated before, having the goal dynamics (manufactured solution) entirely contained in the convergent region is the sufficient but not necessary condition for entrainment. Therefore, there are some points that agree with manufactured solution but outside of convergent region. When relatively loose error tolerances are used in Figure 6.4(b), there are some data points close to the boundary within the convergent region that disagree with manufactured solutions. Numerical discrepancies may exist between the loose error tolerance solutions and the exact manufactured solutions. Therefore, if points are marked by MMS as potential erroneous when using loose error tolerances and are proximity to the convergent boundary, further investigations are needed for these points using tight error tolerances.

6.3 Ship capsizing models

In order to gain additional insight into the use of the MMS on chaotic systems, the two single-degree-of-freedom ship rolling models in Chapter 3 are studied. The equation of motion of the roll model from Falzarano [1990] is repeated here in Eq. (6.11). The data from $Patti-B$ are used here with the values of parameters $\delta_1 = 0.0037$, $\delta_2 = 0.0672$, $\alpha = 3.1355$, $\omega_n = 0.587$ rad/s. In this work, $\omega_e = 0.8$ and f is set to be 0.03 to result in a combination of capsize and non-capsize behavior.

$$\ddot{x} + \delta_1\dot{x} + \delta_2\dot{x} \mid \dot{x} \mid + x - \alpha x^3 = f\cos(\omega_e t) \tag{6.11}$$

The manufactured solution is assumed to be in the form of: $X = \Theta_{amp}\sin(\omega_e t + \phi)$. The corresponding source term $Q(t)$ is defined by Eq.(6.12).

$$\begin{aligned} Q(t) &= \ddot{X} + \delta_1\dot{X} + \delta_2\dot{X} \mid \dot{X} \mid + X - \alpha X^3 - f\cos(\omega_e t); \\ Q(t) &= -\omega_e^2\Theta_{amp}\sin(\omega_e t + \phi) + \delta_1\omega_e\Theta_{amp}\cos(\omega_e t + \phi) + \\ &\quad \delta_2\omega_e^2\Theta_{amp}\cos(\omega_e t + \phi)|\Theta_{amp}\cos(\omega_e t + \phi)| + \Theta_{amp}\sin(\omega_e t + \phi) \\ &\quad -\alpha\Theta_{amp}^3\sin^3(\omega_e t + \phi) - f\cos(\omega_e t) \end{aligned} \tag{6.12}$$

Thus Eq. (6.13) is simulated to get the numerical solutions.

$$\ddot{x} + \delta_1\dot{x} + \delta_2\dot{x} \mid \dot{x} \mid + x - \alpha x^3 = f\cos(\omega_e t) + Q(t) \tag{6.13}$$

Different roll (x) and roll velocity ($\dot{x}$) initial conditions can be obtained by varying Θ_{amp} and ϕ. The safe basin of Falzarano's model is simulated using (S/D)LSODA shown in Figure 6.5. 100×100 initial conditions are used to calculate the solutions. These points are integrated until capsize (roll angle greater than the angle of vanishing stability, *i.e.* 0.5647 rad in this case) or $t_{max} = 16t_e$, where t_e is the period of encounter wave. Figure 6.5 are generated by integrating Eq. (6.11) and Eq. (6.13) simultaneously. Eq. (6.11) is used to determine capsize versus non-capsize, whereas Eq. (6.13) is used to determine agreement with the manufactured solution. If the difference of the final results between the numerical solution and manufactured solution is larger than $1.0e-3$ [3], this point is treated as disagreeing with

[3]The number $1.0e-4$ has also been tried as the measurement of discrepancy for Falzarano's model and the biased model. For the error tolerances specified in Figure 6.5(c), the results are the same as using $1.0e-3$. Therefore, for both models, $1.0e-3$ is used in this work.

the manufactured solution and is marked with black 'o' on top of the capsize/non-capsize figure (MMS warning). Unstable numerical solutions occur in some cases when integrating Eq. (6.13). A point is defined as having an unstable solution if the numerical value from the integration is 10 times larger than the angle of vanishing stability. When an unstable solution is found before the ship capsizes as determined from Eq. (6.11), this point is marked with blue '*'.

Figures 6.5(a) and 6.5(b) show the sensitivity to round-off errors by going from single to double precisions using (S/D)LSODA integration package (Hindmarsh [2006]) using relatively loose error tolerances. This argues that single precision is sufficient to keep round-off errors less than discretization errors for loose error tolerances. Figure 6.5(c) was calculated using DLSODA with relatively tight error tolerances, and checking for capsize every $dt = 0.01$s. There are 6 points marked with MMS discrepancies, of which 5 are capsize cases and one is non-capsize case. This is probably due to the chaotic nature of capsize, *i.e.* sensitivity to initial conditions. 54 points are marked as having unstable numerical solutions. Figure 6.5(d) compares Figures 6.5(a) and 6.5(c) for capsize/safe agreement by setting Figure 6.5(c) as benchmark solution. Of the 10,000 data points, 9,985 points agreed, 2 disagreed and were marked with discrepancies with this method, 10 disagreed with unstable solution warning, and the other 3 disagreed without any warning. On a work station with Intel 2.66GHz CPU chips, the computation of Figure 6.5(a) took about 31.8 seconds to obtain the safe basin and to detect MMS discrepancies and unbounded solutions. The cost of detecting capsize/safe of flagged points in Figure 6.5(a) using the same error tolerances specified in Figure 6.5(c) is 133.5 seconds. While integrating Eq. (6.13) alone with the same error tolerances specified in Figure 6.5(c) and without checking for MMS discrepancies took 570.5 seconds, nearly 3.5 times longer than the sum of previous computation.

Therefore, to improve computational efficiency, the MMS is first applied using single preci-

sion, loose error tolerances. The points with numerical discrepancies when compared with the manufactured solution and points with numerical instability are flagged. Further numerical investigation is needed for these points to check for the capsize/safe results using double precision, tight error tolerances.

Since this model is a time-dependent system, the Jacobian matrix of the system is solution dependent. Therefore, it is difficult to determine the convergent region for this system. The concept of entrainment and convergent regions have not been applied on the ship capsize models.

The biased ship roll motion model from Spyrou et al. [2002] is repeated in Eq. (6.14).

$$\ddot{x} + \beta\dot{x} + x(1-x)(1+ax) = F\sin(\omega_e t) \tag{6.14}$$

Similar to Falzarano's model, the manufactured solution is selected as $X = \Theta_{amp}\sin(\omega_e t+\phi)$. Following the same procedure as before, Eq. (6.15) can be obtained.

$$\ddot{x} + \beta\dot{x} + x(1-x)(1+ax) = F\sin(\omega_e t) + Q(t) \tag{6.15}$$

in which

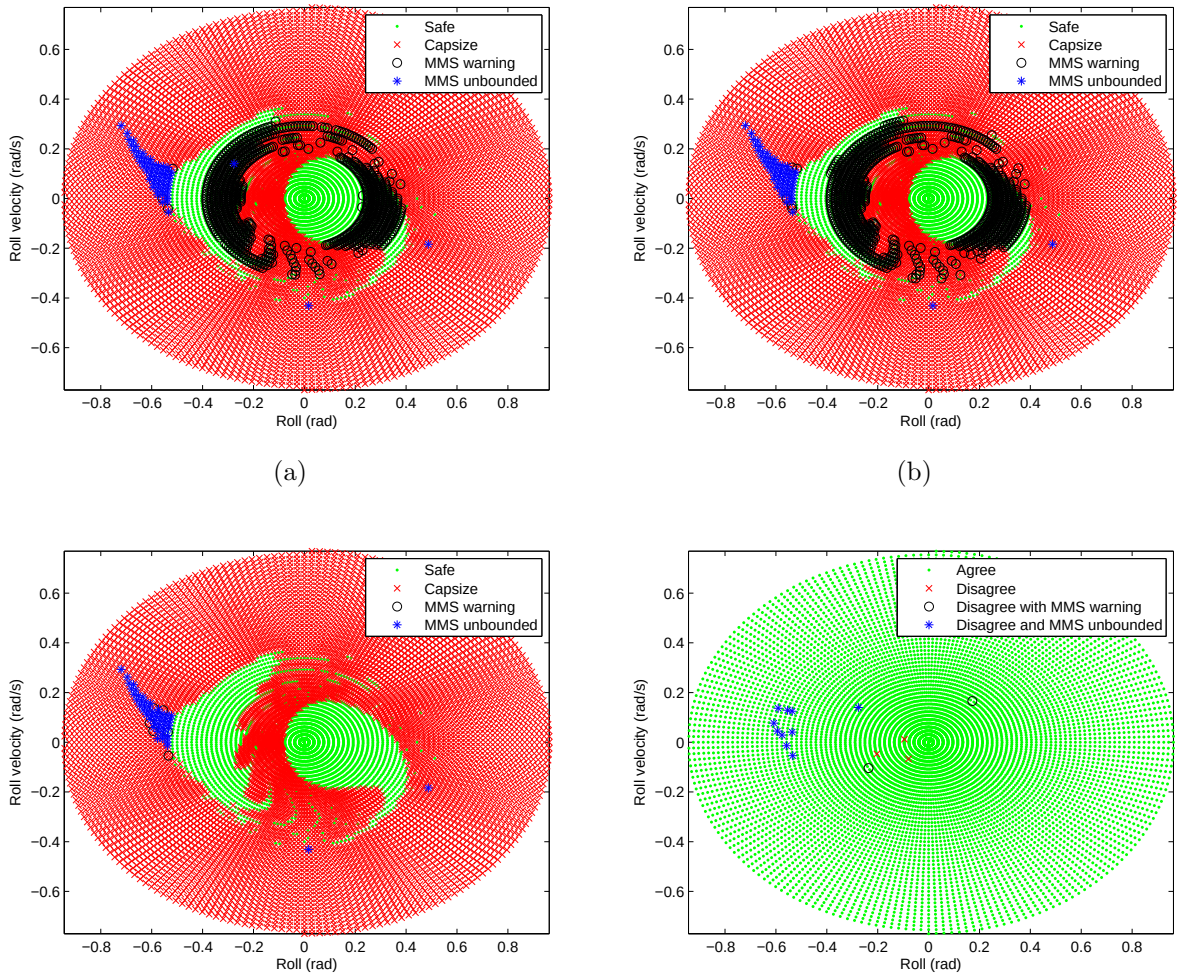

Figure 6.5: Safe basin and direct comparison with manufactured solution using (S/D)LSODA. Figures 6.5(a) and 6.5(b) are simulated using SLSODA and DLSODA, respectively, with relative error tolerance 1.0e-6 and absolute error tolerance 1.0e-8 and checking for capsize every $dt = 0.1$s. Figure 6.5(c) is integrated using DLSODA with relative error tolerance 1.0e-12 and absolute error tolerance 1.0e-16, and checking for capsize every $dt = 0.01$s. Figure 6.5(d) compares Figures 6.5(a) and 6.5(c) for capsize/non-capsize agreement.

$$
\begin{aligned}
Q(t) &= \ddot{X} + \beta\dot{X} + X(1-X)(1+aX) - F\sin(\omega_e t) \\
Q(t) &= -\Theta_{amp}\omega_e^2 \sin(\omega_e t + \phi) + \beta\omega_e\Theta_{amp}\cos(\omega_e t + \phi) \\
&\quad +\Theta_{amp}\sin(\omega_e t + \phi)(1 - \Theta_{amp}\sin(\omega_e t + \phi))(1 + a\Theta_{amp}\sin(\omega_e t + \phi)) \\
&\quad -F\sin(\omega_e t) \qquad (6.16)
\end{aligned}
$$

In this simulation, $a = 0.75$, $\beta = 0.1$, $\omega_e = 0.8$ and F is set to be 0.08. With these values, the mix of capsize and non-capsize occurred.

Figure 6.6 is generated in the same way as Figure 6.5 by integrating Eq. (6.14) and Eq. (6.15) simultaneously. Figures 6.6(a) and 6.6(b) indicates the round-off errors by using single and double precisions at the integration package. This again shows single precision can keep round-off error less than discretization error. Similarly, Figure 6.6(d) compares Figure 6.6(a) and 6.6(c) by setting Figure 6.6(c) as benchmark solution. Of the 10,000 points, 9,880 points agreed, 5 disagreed and showing discrepancies with manufactured solution, 111 disagreed and marked as unstable solutions, and 4 disagreed without any warning. Similarly, the integration time has been estimated. Generating Figure 6.6(a) took approximately 48.5 seconds by indicating capsize/non-capsize and checking for MMS discrepancies and unbounded solutions. The time needed to detect capsize/safe for the flagged points in Figure 6.6(a) using error tolerances specified in Figure 6.6(c) is 239.1 seconds. Integrating only Eq. (6.14), without checking MMS discrepancies, with error tolerances indicated in Figure 6.6(c) took about 819.4 seconds, nearly 3 times longer than the sum of previous calculation.

Different manufactured solutions have been tried in order to show how the form of the manufactured solution would influence the reliability of the MMS approach. Figures 6.7(a) and 6.7(b) are generated for Falzarano's model with the manufactured solution $\Theta = \Theta_{amp}\sin(\omega_n t +$

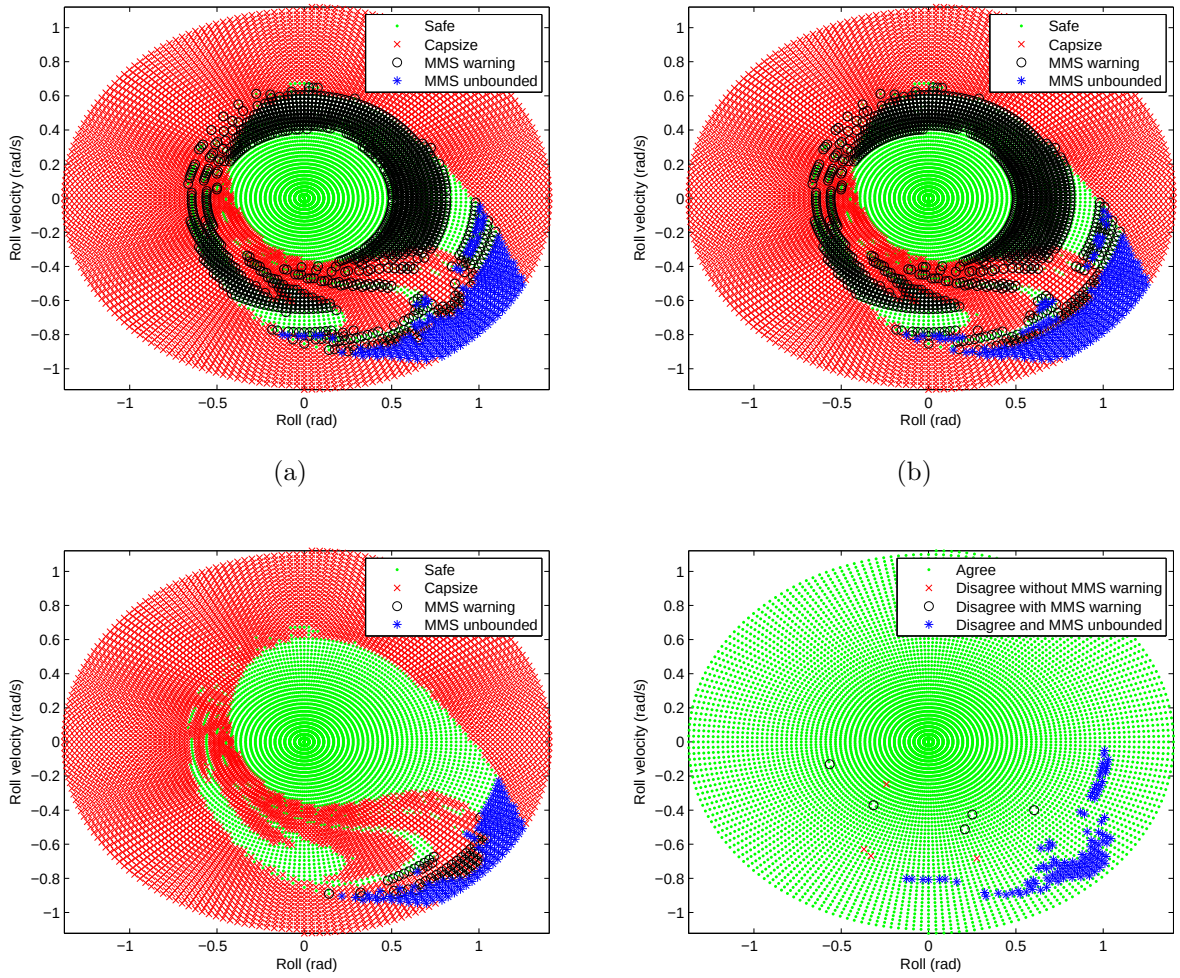

Figure 6.6: Safe basins and direct comparison of manufactured analytic solution to numerical simulation using (S/D)LSODA for the biased model. Figures 6.6(a) and 6.6(b) are simulated using SLSODA and DLSODA respectively, with relative tolerance=1.0e-6 and absolute tolerance=1.0e-8, and checking for capsize every $dt = 0.1$s. Figure 6.6(c) is integrated using DLSODA with relative tolerance=1.0e-12 and absolute tolerance=1.0e-16, and checking for capsize every $dt = 0.01$s. Figure 6.6(d) compares Figures 6.6(a) and 6.6(c) for capsize/non-capsize agreement.

ϕ). Figure 6.7(a) is generated using single precision, relatively loose error tolerances, while Figure 6.7(b) is using double precision, tight error tolerances. By changing the frequency to the natural frequency ω_n, the number of points with MMS discrepancies/unbounded increased much more even when integrated by DLSODA with stringent error tolerances, as shown in Figure 6.7(b). The same happens for the biased model. For the biased model, the new manufactured solution is picked as $X = \Theta_{amp} \sin(0.5t + \phi)$, for which the frequency is significantly different from the encounter frequency. As shown in Figures 6.7(c) and 6.7(d), the number of points with MMS discrepancies/unbounded is much higher than those using the encounter frequency for the manufactured solution. This may be due to the fact that manufactured solution employing the encounter frequency is more physically realistic. Future research will be carried out on whether there is an optimal form of manufactured solutions and how the different choice of manufactured solution will influence the effectiveness and reliability of the method.

6.4 Conclusion

The method of manufactured solutions has been used on dynamical systems with chaotic behaviors. For the classic dynamic systems (Lorenz and Rössler), due to the existence of 'convergent region', the method of manufactured solution can only distinguish numerical instability and chaotic behavior within the region or on the boundaries. For the ship capsize models, potential computational efficiency improvements of up to a factor of 3.5 were demonstrated, which can have a significant impact as the capsize models become more complex and expensive to run.

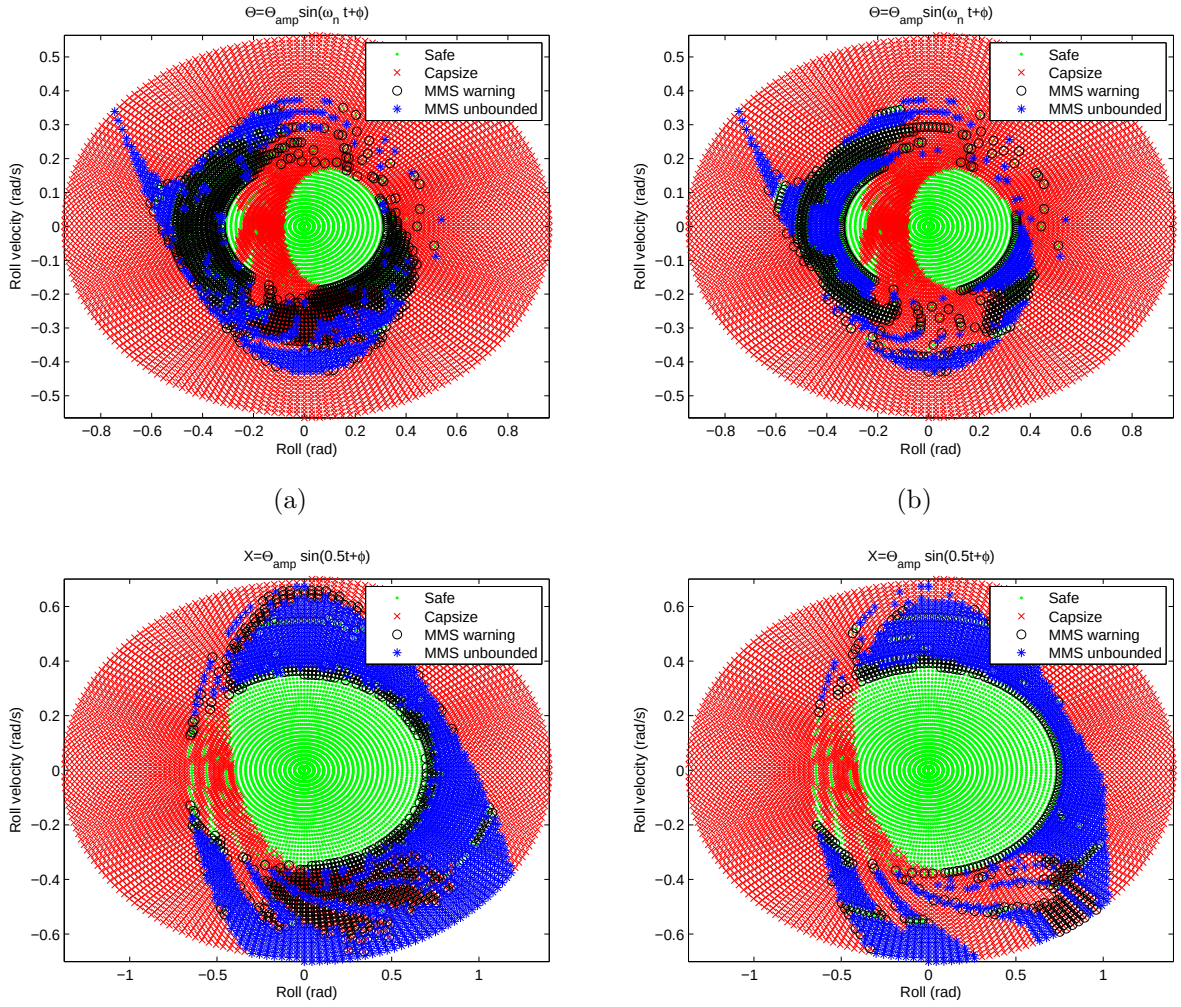

Figure 6.7: Safe basins and direct comparison of manufactured analytic solution to numerical simulation using (S/D)LSODA for Falzarano and biased models. Figures 6.7(a) and 6.7(c) are integrated using SLSODA with relative tolerance=1.0e-6 and absolute tolerance=1.0e-8, and checking for capsize every $dt = 0.1$s. Figures 6.7(b) and 6.7(d) are integrated using DLSODA with relative tolerance=1.0e-12 and absolute tolerance=1.0e-16, and checking for capsize every $dt = 0.01$s.

Chapter 7

Practical Impact of This Research

As mentioned in Chapter 1, one purpose of this research is to use the Melnikov's method to obtain criteria that related to the development of new stability criteria in IMO. The IMO stability criteria address three modes of capsize: the harmonic resonance for dead ship; the maneuvering related problems such as broaching and the stability variation problems such as parametric rolling.

In this dissertation, the extended Melnikov's method is first applied to single-degree-of-freedom roll models in regular beam seas. This is the simplest model of harmonic resonance for a dead-ship. The purpose is to show the validity and feasibility of the extended Melnikov's method. Although this cannot be used as the criteria of harmonic resonance, this work provides the possibility of applying the extended Melnikov's method to the surf-riding problem.

The threshold of global surf-riding in following regular waves is obtained using the extended Melnikov's method. Since surf-riding is a precursor of broaching, the occurrence of global surf-riding can serve as a criteria for broaching. The results from the extended Melnikov's

method is more accurate than the standard Melnikov's method. Although a general analytical formula seems to be unavailable at this time, the computational efficiency surpasses numerical simulation.

The study of the heave-roll-sway coupled model using the Melnikov's method is to show the possibility of applying this method for multi-DOF problem. With this knowledge, in future work, we may be able to address the parametric roll problem.

The work of applying the method of manufactured solutions to systems with chaotic behavior has demonstrated to have computational efficiency improvement, especially for the ship capsizing models. This can be a great beneficial when the capsize model becomes more complicated.

Chapter 8

Conclusions and Future Work

8.1 Summary

In this dissertation, the extended Melnikov's method has been used for several nonlinear ship dynamics models to analyze the complex dynamics. This method overcomes the small damping constraint set by the standard Melnikov's method at the expense of not being able to produce closed-form formula. However, the extended Melnikov's method as applied here still allows substantial computational efficiencies compared to direct numerical simulation.

The application of the extended Melnikov's method to single-DOF ship rolling models in Chapter 3 demonstrated the validity and feasibility of the method. This provided the basis for applying the method to the surf-riding problem in Chapter 4.

The extended Melnikov's method provided more accuracy on the prediction of global surf-riding than the standard Melnikov's method in Chapter 4. An empirical formula is obtained based on the numerical results from the extended Melnikov's method. But a more general formula is needed. And validation is required for the formula to work on other ship models.

In addition, if the linear damping term is larger than some value, it is impossible to find σ_c to yield the homoclinic orbit, which presents a secondary constraint on this approach.

To apply the Melnikov's method for slowly varying systems with large damping, the unperturbed system needs to be a homoclinic orbit (Wiggins [1988]). Therefore, in Chapter 5, as a demonstration of concept, a hypothetical fictitious quadratic damping term is assumed to be large. And the constant σ is chosen as to eliminate any constant terms in the unperturbed sub-system. While not physical, it provides the possibility of applying the Melnikov's method to multi-DOF system with large damping.

The final work in the dissertation is the application of the method of manufactured solution to systems with chaotic behaviors in Chapter 6. MMS is proven to be able to identify numerical discrepancies in classic chaotic models within the convergent region. And for a physically reasonable manufactured solution, MMS was demonstrated to improve computational efficiency in single-DOF ship capsizing models.

8.2 Future work

This research has used the extended Melnikov's method to propose some criteria that related to the development of new performance based intact stability criteria in IMO. One interesting future work would be to compare the stability criteria proposed in this dissertation to the existing quasi-static criteria.

In the application of the biased roll model in Chapter 3, the measure of bias a is assumed to be large such that $1 - a$ is treated as a small number. More research can be carried out when $1 - a$ cannot be assumed to be a small term. When the damping term is assumed to be small, the unperturbed sub-system in this case is a homoclinic orbit. The extended

Melnikov's method can be tried to a system like this.

One constraint of the extended Melnikov's method is the inability to produce a closed-form formula. In Chapter 4, in order to address the constrain, a formula $-4\tanh(p_1 - p_2\pi/2)/\pi$ has been obtained as the 'best fit' approximation based on the numerical data. However, this formula only works when $p_2 < 0.2$. A more general formula is needed for a large range of p_2. In addition, this formula needs to be validated on other ship models.

Chapter 5 is only preliminary research for the multi-DOF problem with large damping. As mentioned before, if the linear damping term is assumed to be large, it is chanllenging to find the requisite homoclinic orbit in the unperturbed sub-system. And for the Melnikov's method in slowly varying system, the homoclinic orbit seems to be essential. More research can be done to see how this constraint can be addressed. Numerical simulations can be carried out and compared with the Melnikov's method. The results from this 3DOF model can be compared with 1DOF model assuming sway and heave are all zero. Moreover, we can look for the possibility of reducing other multi-DOF ship models to a slowly varying system; or the possibility of applying the Melnikov's method to a multi-DOF parametric roll problem.

The method of manufactured solutions has been proven to have computational efficiency improvement when applying to single-DOF ship capsizing models. An interesting future work might be applying MMS to multi-DOF ship motion models to see how this non-traditional application of the MMS will work for multi-DOF chaotic systems.

Bibliography

AIAA. *Guide for the Verification and Validation of Computational Fluid Dynamics Simulations*. American Institute of Aeronautics and Astronautics, Reston, VA, January 1998. G-077-1998.

ASME Performance Test Code Committee 60. *Guide for verification and validation in computational solid mechanics*. American Society of Mechanical Engineers, New York, NY, 2006. ASME V&V 10-2006.

R.C. Batra and X.Q. Liang. Finite dynamic deformations of smart structures. *Computational Mechanics*, 20:427–438, 1997.

V. Belenky, J.O. de Kat, and N. Umeda. Toward performance-based criteria for intact stability. *Marine Technology*, 45:101–123, 2008.

M. Bikdash, B. Balachandran, and A.H. Nayfeh. Melnikov analysis for a ship with a general roll-damping model. *Nonlinear Dynamics*, 6:101–124, 1994.

S.L. Chen and S.W. Shaw. Phase space transport in a class of multi-degree-of-freedom system. In *Proceedings of 1997 ASME Design Engineering Technical Conferences, DETC97'*, Sacramento, CA, USA, 1997.

S.L. Chen, S.W. Shaw, and A.W. Troesch. A systematic approach to modelling nonlinear multi-DOF ship motions in regular seas. *Journal of Ship Research*, 43:25–37, 1999.

J. De Kat and W.L.III Thomas. Extreme rolling, broaching and capsizing - model tests and simulations of a steered ship in waves. In *Twenty-second Symposium on Naval Hydrodynamics*, pages 69–88, 1998.

J. De Kat and W.L.III Thomas. Broaching and capsize model tests for validation of numerical ship motion predictions. In D. Vassalos, M. Hamamoto, A. Papanikolaou, and D. Molyneux, editors, *Contemporary Ideas on Ship Stability*, pages 69–88. Elsevier Science Ltd, 2000.

Department of Defense. *DoD Modeling and Simulation (M&S) Verification, Validation, and Accreditation (VV&A)*, May 2003. Department of Defense Instruction 5000.61.

Department of the Navy. *Verification, Validation, and Accreditation (VV&A) of Models and Simulations*, April 1999. SECNAV Instruction 5200.40.

T. Endo, L.O. Chua, and T. Narita. Chaos from phase-locked loops–part II: high dissipation case. *IEEE Transanctions on Circuits and Systems*, 36:255–263, 1989.

J.M. Falzarano. *Predicting complicated dynamics leading to vessel capsizing.* PhD thesis, University of Michigan, Ann Arbor, 1990.

J.M. Falzarano and F. Zhang. Multiple degree of freedom global transient ship rolling motion: large amplitude forcing. *Stochastic Dynamics and Reliability of Nonlinear Ocean Systems, ASME WAM*, DE-77:99–108, 1994.

J.M. Falzarano, A.W. Shaw, and A.W. Troesh. Application of global methods for analyzing dynamical systems to ship rolling motion and capsizing. *International Journal of Bifurcation and Chaos*, 1:101–115, 1992.

W. Froude. Remarks on Mr. Scott Russel's paper on rolling. *Transactions of Institute of Naval Architects*, 3:232–275, 1863.

S. Grochowalski, J.B. Archilbald, F.J. Connolly, and C.K. Lee. Operational factors in stability safety of ships in heavy seas. In *Proceedings of 5th International Conference on Stability of Ships and Ocean Vehicles STAB94'*, Melbourne, FL, USA, 1994.

J. Guckenheimer and P. Holmes. *Nonlinear oscillations, dynamical systems, and bifurcations of vector fields*. Springer-Verlag, New York, 6th edition, 2002.

A.C. Hindmarsh. Serial FORTRAN solvers for ODE initial value problems. `http://www.llnl.gov/CASC/odepack/`, 2006.

S.R. Hsieh, A.W. Troesch, and S.W. Shaw. A nonlinear probabilistic method for predicting vessel capsizing in random beam seas. *Proceedings of the Royal Society of London*, 446: 195–211, 1994.

A.W. Hübler and E. Lüscher. Resonant stimulation and control of non-linear oscillators. *Naturwissenschaft*, 76:67, 1989.

Y. Ikeda, Y. Himeno, and N. Tanaka. On roll damping force of ship-effect of friction of hull and normal force of bilge keels. *Journal of Kansai Society of Naval Architects*, 161:41–49, 1976. in Japanese.

IMO. Revised guidance to the master for avoiding dangerous situations in adverse weather and sea conditions. MSC.1/Circ.1228, London, 2007.

E.A. Jackson. Control of dynamic flow with attractors. *Physical Review A*, 44(8):4839–4853, October 1991a.

E.A. Jackson. On the control of complex dynamics systems. *Physica D*, 50:341–366, 1991b.

C. Jiang, A.W. Troesh, and S.W. Shaw. Highly nonlinear rolling motion of biased ships in random beamseas. *Journal of Ship Research*, 40:125–135, 1996.

C. Jiang, A.W. Troesh, and S.W. Shaw. Capsize criteria for ship models with memory-dependent hydrodynamics and random excitation. *Philosophical Transactions of Royal Society London A*, 358:1761–1791, 2000.

M. Kan. Surging of large amplitude and surf-riding of ships in following seas. *Naval Architecture and Ocean Engineering*, 28:1–14, 1990. The Society of Naval Architects of Japan, Ship and Ocean Foundation.

M. Kan. Chaotic capsizing. In *Proceedings of the 20th ITTC Seakeeping Committee*, Osaka, September 10-11 1992.

H. Khalil. *Nonlinear Systems Analysis*. Prentice-Hall, New York, 1996.

P. Knupp and K. Salari. *Verification of computer codes in computational science and engineering*. Chapman and Hall, 2002.

E. M. Lewandowski. *The Dynamics of Marine Craft*. World Scientific, 2004.

E. V. Lewis, editor. *Principles of Naval Architecture, v.3. Motions in Wave and Controllability*. Society of Naval Architects and Marine Engineers, Jersey City, NJ, 1988.

V.K. Melnikov. On the stability of the center for time periodic perturbations. *Transactions of the Moscow Mathematical Society*, 12:1–57, 1963.

A.H. Nayfeh and B. Balachandran. *Applied nonlinear dynamics: analytical, computational, and experimental methods*. Wiley, New York, 1995.

H. Nowachi and L. Fereiro. Historical roots of the theory of hydrostatic stability of ships. In *Proceedings of 8th International Conference on Stability of Ships and Ocean Vehicles*, Madrid, September 15-19 2003.

W.L. Oberkampf and C.J. Roy. *Verification and Validation in Scientific Computing*. Cambridge University Press, New York, to appear 2010.

J.R. Paulling and R.M. Rosenberg. On unstable ship motions resulting from nonlinear coupling. *Journal of Ship Research*, 42:36–46, 1959.

K. Radhakrishnan and A.C. Hindmarsh. Description and use of LSODE, the livermore solver for ordinary differential equations. Technical Report UCRL-ID-113855, Lawrence Livermore National Laboratory, 1993.

P.J. Roache. *Verification and validation in computational science and engineering*. Hermosa Publishers, 1998.

P.J. Roache. Code verification by the method of manufactured solutions. *Journal of Fluids Engineering*, 124, March 2002.

C.J. Roy, C.C. Nelson, T.M. Smith, and C.C. Ober. Verification of Euler/Navier-Stokes codes using the method of manufactured solutions. *International Journal for Numerical Methods in Fluids*, 44(6):599–620, February 2004.

F.M.A. Salam. The Melnikov technique for highly dissipative systems. *SIAM Journal on Applied Mathematics*, 47:232–243, 1987.

T.M. Shih. A procedure to debug computer programs. *International Journal of Numerical Methods in Engineering*, 21:1027–1037, 1985.

K.J. Spyrou. Surf-riding and oscillation of a ship in quatering waves. *Journal of Marine Science and Technology*, 1:24–26, 1995.

K.J. Spyrou. Dynamic instability in quatering seas: the behavior of a ship during broaching. *Journal of Ship Research*, 40:46–59, 1996.

K.J. Spyrou. On the parametric rolling of ships in a following sea under simultaneous nonlinear periodic surging. *Philosophical Transanctions of Royal Society London A*, 358: 1813–1834, 2000.

K.J. Spyrou. Asymmetric surging of ships in following seas and its repercussions for safety. *Nonlinear Dynamics*, 43:149–172, 2006.

K.J. Spyrou and J.M.T. Thompson. The nonlinear dynamics of ship motions: a field overview and some recent developments. *Philosophical Transactions of Royal Society London A*, 358: 1735–1760, 2000.

K.J. Spyrou, B. Cotton, and B. Gurd. Analytical expressions of capsize boundary for a ship with roll bias in beam waves. *Journal of Ship Research*, 46:167–174, 2002.

S. Steinberg and P.J. Roache. Symbolic manipulation and computational fluid dynamics. *AIAA Journal*, 22:1390–1394, 1985.

J.M.T. Thompson. Designing against capsize in beam seas: Recent advances and new insights. *Applied Mechanics Reviews*, 50:307–325, 1997.

J.M.T. Thompson, S.R. Bishop, and L.M. Leung. Fractal basins and chaotic bifurcations prior to escape from a potential well. *Physics Letters A*, 121:116–120, 1987.

N. Umeda. Probabilistic study of surf-riding of a ship in irregular following seas. In *Proceedings of 4th International Conference on Stability of Ships and Ocean Vehicles*, Naples, Italy, 1990.

N. Umeda, A. Maki, S. Izawa, H. Sano, Y. Sogawa, E. Maeda, and I. Tsukamoto. New generation intact stability criteria: a step forward. In *Proceedings of 10th International Conference on Stability of Ships and Ocean Vehicles*, St. Petersburg, Russia, 2009.

S. Wiggins. *Global Bifurcations and Chaos: Analytical Methods*. Springer-Verlag, New York, 1988.

S. Wiggins and P. Holmes. Homoclinic orbits in slowly varying oscillators. *SIAM Journal on Mathematical Analysis*, 18(3):612–629, 1987.

W. Wu and L.S. McCue. Melnikov's method for ship motions without the constraint of small linear damping. In *Proceedings of IUTAM Symposium on Fluid-Structure Interaction in Ocean Engineering*, Hamburg, 2007.

W. Wu and L.S. McCue. Application of the extended Melnikov's method for single-degree-of-freedom vessel roll motion. *Ocean Engineering*, 35:1739–1746, 2008.

W. Wu and K.J. Spyrou. Technical note: Prediction of the threshold of global surf-riding by an extended Melnikov's method. In *Proceedings of 10th International Conference on Stability of Ships and Ocean Vehicles*, St. Petersburg, Russia, 2009.

W. Wu, L.S. McCue, and C.J. Roy. The method of manufactured solutions applied to chaotic systems. *Nonlinear Dynamics*, 2009a. under review.

W. Wu, K.J. Spyrou, and L.S. McCue. Improved prediction of the threshold of surf-riding of a ship in steep following seas. *Ocean Engineering*, 2009b. submitted.

H.C. Yee and P.K. Sweby. Global asymptotic behavior of iterative implicit schemes. *International Journal of Bifurcation and Chaos*, 4(6):1579–1611, 1994.

H.C. Yee and P.K. Sweby. Nonlinear dynamics and numerical uncertainties in CFD. Technical Report NASA Technical Memorandum 110398, NASA, April 1996.

H.C. Yee and P.K. Sweby. Dynamics of numerics and spurious behaviors in CFD computations. Technical Report RIACS 97.06, Research Institute for Advanced Computer Science NASA Ames Research Center, June 1997.

H.C. Yee, J.R. Torczynski, S.A. Morton, M.R. Visbal, and P.K. Sweby. On spurious behavior of CFD simulations. In *13th AIAA Computational Fluid Dynamics Conference*, Snowmass, CO, 1997.

Appendix A

Calculation of σ and T for Surf-riding Model

A.1 Treating linear damping as large term

The detailed numerical methods for calculating σ and T is given by Endo et al. [1989]. For the unperturbed system

$$\begin{aligned} x' &= y, \\ y' &= -\sin x - p_1 y - \sigma. \end{aligned} \tag{A.1}$$

Let (x_1, y_1) and (x_2, y_2) be the points on the heteroclinic orbits and have distance $\delta = 10^{-3}$ to the respective saddle points. x_1, y_1 is on the unstable eigenvector $[1, \lambda_1]^T$ and x_2, y_2 is on

the stable eigenvector $[1, \lambda_2]^T$, in which

$$\lambda_1 = \frac{-p_1 + \sqrt{p_1^2 + 4\sqrt{1-\sigma^2}}}{2}; \tag{A.2a}$$

$$\lambda_2 = \frac{-p_1 - \sqrt{p_1^2 + 4\sqrt{1-\sigma^2}}}{2}. \tag{A.2b}$$

The coordinates of these two points can be given as

$$x_1 = \pi + \arcsin\sigma - \delta; \tag{A.3a}$$

$$y_1 = -\lambda_1(\sigma)\delta; \tag{A.3b}$$

$$x_2 = -\pi + \arcsin\sigma + \delta; \tag{A.3c}$$

$$y_2 = \lambda_2(\sigma)\delta. \tag{A.3d}$$

Define functions

$$F_1(T, \sigma) = X_1(T, x_1, y_1, \sigma) - x_2(\sigma); \tag{A.4a}$$

$$F_2(T, \sigma) = Y_1(T, x_1, y_1, \sigma) - y_2(\sigma). \tag{A.4b}$$

where (X_1, Y_1) is the unstable orbits of Eq.(A.1) with initial condition (x_1, y_1) at $t = 0$. At time $t = T$, the orbit will end up at (x_2, y_2). Therefore, this orbit is a heteroclinic orbit. For the critical values of σ and T, functions F_1 and F_2 should all be zero. Therefore, there are two equations and two unknowns. σ and T can be obtained by numerically solving Eq.(A.4)

using Newton's method:

$$\begin{pmatrix} T_{k+1} \\ \sigma_{k+1} \end{pmatrix} = \begin{pmatrix} T_k \\ \sigma_k \end{pmatrix} - \begin{pmatrix} J_1 & J_2 \\ J_3 & J_4 \end{pmatrix}^{-1} \begin{pmatrix} F_1(T_k, \sigma_k) \\ F_2(T_k, \sigma_k) \end{pmatrix}. \tag{A.5}$$

The elements of the Jacobian matrix can be calculated by taking partial derivatives of F_1 and F_2. For example: $J_1 = \partial F_1/\partial T$. Substituting Eq. (A.4) into this, $J_1 = \partial X_1/\partial T - \partial x_1/\partial T$. From Eq. (A.1), $\partial X_1/\partial T = Y_1$ and x_1 is independent of T. Therefore, $J_1 = Y_1$. Similarly, J_3 can be obtained. When calculating J_2 and J_4, since x_1, y_1, x_2, y_2 and σ are all functions of σ, chain rule is used.

$$J_1 = Y_1; \tag{A.6a}$$

$$\begin{aligned} J_2 &= \frac{\partial X_1}{\partial x_1}\frac{\partial x_1}{\partial \sigma} + \frac{\partial X_1}{\partial y_1}\frac{\partial y_1}{\partial \sigma} + \frac{\partial X_1}{\partial \sigma} - \frac{\partial x_2}{\partial \sigma} \\ &= \frac{\partial X_1}{\partial x_1}\frac{1}{\sqrt{1-\sigma^2}} + \frac{\partial X_1}{\partial y_1}\frac{\sigma\delta}{\sqrt{p_1^2(1-\sigma^2)+4(1-\sigma^2)^{3/2}}} + \frac{\partial X_1}{\partial \sigma} + \frac{1}{\sqrt{1-\sigma^2}}; \end{aligned} \tag{A.6b}$$

$$J_3 = \frac{\partial Y_1}{\partial T} = -\sin X_1 - p_1 Y_1 - \sigma; \tag{A.6c}$$

$$\begin{aligned} J_4 &= \frac{\partial Y_1}{\partial x_1}\frac{\partial x_1}{\partial \sigma} + \frac{\partial Y_1}{\partial y_1}\frac{\partial y_1}{\partial \sigma} + \frac{\partial Y_1}{\partial \sigma} - \frac{\partial y_2}{\partial \sigma} \\ &= \frac{\partial Y_1}{\partial x_1}\frac{1}{\sqrt{1-\sigma^2}} + \frac{\partial Y_1}{\partial y_1}\frac{\sigma\delta}{\sqrt{p_1^2(1-\sigma^2)+4(1-\sigma^2)^{3/2}}} + \frac{\partial Y_1}{\partial \sigma} \\ &\quad - \frac{\sigma\delta}{\sqrt{p_1^2(1-\sigma^2)+4(1-\sigma^2)^{3/2}}}. \end{aligned} \tag{A.6d}$$

Let $u_1 = \partial X_1/\partial x_1$, $u_2 = \partial Y_1/\partial x_1$. Taking derivatives to Eq.(A.1) with respect to x_1:

$$\frac{du_1}{dt} = u_2; \tag{A.7a}$$
$$\frac{du_2}{dt} = -u_1 \cos X_1 - p_1 u_2 - \sqrt{1-\sigma^2}. \tag{A.7b}$$

u_1 and u_2 can be numerically solved using Eq.(A.7) combined with Eq.(A.1) with initial conditions $(x_1(\sigma_k), y_1(\sigma_k), 1, 0)$. Similarly, if let $u_1 = \partial X_1/\partial y_1$ and $u_2 = \partial Y_1/\partial y_1$. They can be solved using Eq.(A.8) and Eq.(A.1) with initial condition $(x_1(\sigma_k), y_1(\sigma_k), 0, 1)$.

$$\frac{du_1}{dt} = u_2; \tag{A.8a}$$
$$\frac{du_2}{dt} = -u_1 \cos X_1 - p_1 u_2 - \frac{\sqrt{p_1^2(1-\sigma^2) + 4(1-\sigma^2)^{3/2}}}{\sigma\delta}. \tag{A.8b}$$

The derivatives with respect to σ can also be calculated numerically. Let $u_1 = \partial X_1/\partial\sigma$ and $u_2 = \partial Y_1/\partial\sigma$. Taking derivative of Eq.(A.1) with respect to σ:

$$\frac{du_1}{dt} = u_2 \tag{A.9a}$$
$$\frac{du_2}{dt} = -u_1 \cos X_1 - p_1 u_2 + 1 \tag{A.9b}$$

u_1 and u_2 can be solved using Eq.(A.1) and Eq.(A.9) with initial condition $(x_1(\sigma_k), y_1(\sigma_k), 0, 0)$.

A.2 Treating both linear and quadratic damping terms large

The method for calculating σ and T for this case is basically the same as the linear case except for minor differences. For the Jacobian matrix of the equation, in this case, $J_3 = -\sin X_1 - p_1 Y_1 - p_2 Y_1^2 - \sigma$. Other terms in this matrix are same as previous.

For calculating $u_1 = \partial X_1/\partial x_1$ and $u_2 = \partial Y_1/\partial x_1$, we should use Eqs. (A.10) and (A.1).

$$\frac{du_1}{dt} = u_2; \tag{A.10a}$$

$$\frac{du_2}{dt} = -\cos X_1 u_1 - p_1 u_2 - 2p_2 Y_1 u_2 - \sqrt{1-\sigma^2}. \tag{A.10b}$$

The equations for calculating $u_1 = \partial X_1/\partial y_1$ and $u_2 = \partial Y_1/\partial y_1$ are Eqs. (A.11) and (A.1).

$$\frac{du_1}{dt} = u_2; \tag{A.11a}$$

$$\frac{du_2}{dt} = -\cos X_1 u_1 - p_1 u_2 - 2p_2 Y_1 u_2 - \frac{\sqrt{p_1^2(1-\sigma^2) + 4(1-\sigma^2)^{3/2}}}{\sigma\delta}. \tag{A.11b}$$

And the equation for $u_1 = \partial X_1/\partial \sigma$ and $u_2 = \partial Y_1/\partial \sigma$ are Eqs.(A.12) and (A.1).

$$\frac{du_1}{dt} = u_2 \tag{A.12a}$$

$$\frac{du_2}{dt} = -u_1 \cos X_1 - p_1 u_2 - 2p_2 Y_1 u_2 - 1 \tag{A.12b}$$